

**Organotypische Schnittkulturen aus Glioblastomgewebe
als präklinisches Testsystem**

Dissertation
zur Erlangung des akademischen Grades
Dr. rer. med.

an der Medizinischen Fakultät
der Universität Leipzig

eingereicht von: M. Sc. Susann Hähnel
Geburtsdatum / -ort: 10.11.1990 in Schkeuditz

angefertigt an / in: Medizinische Fakultät der Universität Leipzig /
Universitätsklinikum Leipzig
Institut für Anatomie / Klinik und Poliklinik für Neurochirurgie

Betreuer: Prof. Dr. Ingo Bechmann
Prof. Dr. Frank Gaunitz

Beschluss über die Verleihung des Doktorgrades vom: 24.01.2023

Inhalt

Einleitung	3
Glioblastoma multiforme	3
Standardtherapie und MGMT	4
Immuntherapie	5
Heterogenität im GBM	6
Individualisierte Therapie.....	7
RNA-Sequenzierung	8
Modelle in der Krebsforschung	10
Schnittkulturen aus Patientengewebe.....	11
Zielstellung der Arbeit.....	13
Publikation I.....	14
Publikation II.....	33
Zusammenfassung.....	63
Referenzen.....	66
Darstellung des eigenen Beitrags	72
Erklärung über die eigenständige Abfassung der Arbeit	76
Lebenslauf.....	77
Publikationen.....	78
Vorträge	78
Danksagung	79

Einleitung

Glioblastoma multiforme

Gliome sind mit einer Inzidenz von 6 pro 100.000 Einwohner pro Jahr die häufigsten primären Hirntumore bei Erwachsenen. Etwa die Hälfte dieser Patienten erkrankt an einem Glioblastom (GBM), welches die bösartigste Form des Glioms darstellt und daher nach der WHO-Klassifizierung dem Grad 4 zugeordnet wird [1,2]. Die Inzidenz steigt mit zunehmendem Alter, das mediane Alter bei Diagnosestellung liegt bei 65 Jahren. Männer erkranken etwa 1,5 mal häufiger als Frauen [2]. Ein Viertel aller GBMs entsteht im Frontallappen, ein Fünftel im Temporallappen, 13 % im Parietallappen und 3 % kommen im Okzipitallappen vor [3]. Das sogenannte Schmetterlingsgliom breitet sich symmetrisch beidseitig des Corpus callosum aus und stellt eine häufige Sonderform dar [4]. Die Symptome eines GBMs können je nach Lokalisation des Tumors sehr vielfältig und teilweise unspezifisch sein. Häufig sind es starke Kopfschmerzen, epileptische Anfälle, neurologische Ausfälle oder Persönlichkeitsveränderungen, die zu einer ärztlichen Vorstellung des Patienten führen [5,6]. Über bildgebende Verfahren erfolgt die vorläufige Diagnostik und das Vorliegen eines GBMs wird nach oder bereits während der Operation histopathologisch bestätigt.

Über die Ursachen für die Entstehung eines GBMs ist wenig bekannt. Der einzige erwiesene prädisponierende Faktor ist eine früher erfolgte Bestrahlung des Kopfes, häufig im Kindes- und Jugendalter im Zuge der Behandlung einer Leukämieerkrankung [7]. Histologisch ist das GBM charakterisiert durch ein infiltratives Wachstum, eine hohe mitotische Aktivität, die Ausbildung von Blutgefäßen zur eigenen Versorgung sowie zum Teil großflächige nekrotische Bereiche im Gewebe [8,9]. Insbesondere das infiltrative Wachstum entlang der Fasern der gesunden weißen Substanz erschwert die vollständige Resektion des malignen Gewebes und führt bei der Mehrheit der Patienten (~ 90 %) früher oder später zu Rezidivbildung und Tumorprogression [10]. Trotz der größtmöglichen Resektion und anschließender aggressiver Radiochemotherapie mit dem alkylierenden Zytostatikum Temozolomid (TMZ), liegt das mediane Gesamtüberleben von Patienten mit einem primären GBM noch immer bei circa 15 Monaten nach Diagnosestellung [11,12]. Gänzlich unbehandelte Patienten weisen ein medianes Überleben von lediglich drei Monaten auf [13]. Das ehemals primär genannte GBM ist definiert als *de novo* Entwicklung des Tumors ohne maligne Vorstufen, wohingegen das vormals sekundäre GBM aus niedrigradigen Astrozytomen evolviert und vorrangig bei jüngeren Patienten beobachtet wird – der Median liegt hier bei circa 44 Jahren [5,6,14]. Beide Subtypen unterscheiden sich aber nicht nur hinsichtlich ihrer Entstehungsgeschichte, sondern auch in ihren molekularen Expressionsmustern, dem Ansprechen auf die Standardtherapie und der Prognose [15–17].

In einer 2009 publizierten Studie wurde gezeigt, dass Patienten mit sekundärem GBM unter Radiochemotherapie im Mittel doppelt so lange überleben wie Patienten mit primärem GBM (31 Monate vs. 15 Monate) [18].

In den letzten Jahren hat die molekulare Charakterisierung von Tumoren zunehmend an Bedeutung gewonnen und spielt nun auch beim GBM hinsichtlich Diagnostik, Therapieentscheidungen und Prognose eine entscheidende Rolle. Zu den beiden wichtigsten Markern, die standardmäßig bestimmt werden, gehören der Mutationsstatus der Isocitratdehydrogenasen (IDH) 1 und 2 sowie der Methylierungsstatus des Promotors für das DNA-Reparaturenzym O-6-Methylguanin-DNA-Methyltransferase (MGMT) [19]. Auf MGMT wird im folgenden Kapitel „Standardtherapie und MGMT“ näher eingegangen. IDH1 ist im Cytosol und den Peroxisomen lokalisiert, IDH2 hingegen kommt in den Mitochondrien vor [20]. Beide Enzyme fungieren als Katalysatoren bei der oxidativen Decarboxylierung von Isocitrat [19]. Punktmutationen in IDH1 und 2 kommen ausschließlich in sekundären GBMs vor, sind mit einem längeren Überleben assoziiert und damit prognostisch relevant [21]. Diagnostisch unterscheidet man seit der Abschaffung der Begriffe „primär“ und „sekundär“ neben IDH-wildtypischem GBM (ehemals primäres GBM) das IDH-mutierte Astrozytom Grad 4 (früher IDH-mutiertes oder sekundäres GBM), welches zwar histologisch sehr ähnlich ist, sich aber biologisch und klinisch vom GBM unterscheidet [5,22]. In meiner Arbeit habe ich mich ausschließlich mit dem primären, IDH-wildtypischen GBM befasst.

Standardtherapie und MGMT

Der erste und wichtigste Teil der Therapie des GBMs stellt die operative Entfernung des malignen Gewebes dar [23]. Um die Radikalität der Resektion zu erhöhen, bedient man sich während der Operation unterstützender Verfahren, da die Abgrenzung von malignem zu gesundem Gewebe mit bloßem Auge sehr schwierig ist. So wird in den Richtlinien der Europäischen Gesellschaft für Neuroonkologie (*European Association of Neuro-Oncology, EANO*) der Einsatz von 5-Aminolävulinsäure (5-ALA) empfohlen, welche sich in GBM-Zellen anreichert, dem Tumor fluoreszierende Eigenschaften verleiht und die malignen Zellen für den Operateur sichtbar macht [24–26]. Nach der erfolgten Resektion wird mit der adjuvanten Radiochemotherapie begonnen, der sich 6 Zyklen Erhaltungskemotherapy anschließen [23]. Eine ergänzende Therapie mit elektrischen Wechselfeldern, über deren Einsatz im Einzelfall mit dem Patienten entschieden wird, kann das progressionsfreie Überleben sowie das Gesamtüberleben von Patienten mit neu diagnostiziertem GBM verlängern [27].

Seit der Veröffentlichung einer klinischen Phase III-Studie von Roger Stupp et al. 2005, gilt die Kombinationstherapie aus TMZ und der Bestrahlung der betroffenen Hirnregion als Standardtherapie für primäre Glioblastome. In dieser Studie wurde gezeigt, dass die

experimentelle Gruppe (TMZ + Bestrahlung) im Mittel ein circa drei Monate längeres Gesamtüberleben zeigte als die Kontrollgruppe, welche die alleinige Bestrahlungstherapie erhielt [11,12]. Die Bestrahlung erfolgt fraktioniert (1,8-2 Gy pro Fraktion) über mehrere Wochen bis zu einer Gesamtdosis von 60 Gy [26]. TMZ ist ein Zytostatikum, welches als *Prodrug* verabreicht und im humanen Stoffwechsel bei physiologischem pH-Wert in seine aktive Form umgewandelt wird. TMZ methyliert als alkylierendes Agens die Basen der DNA und verursacht auf diese Weise Schäden in der DNA [28]. Kommen solche Schäden in den Promotorregionen oder anderen kodierenden Bereichen von Genen vor, wird deren Replikation beeinträchtigt und die Expression behindert. Dadurch kommt es vermehrt zur Apoptose in den betroffenen Zellen. MGMT ist ein DNA-Reparaturgen und kodiert für ein Protein, welches DNA-Schäden repariert, die von alkylierenden Agenzien wie TMZ oder Nitrosoharnstoffen, die ebenfalls in der Neuroonkologie als Zytostatika Verwendung finden, hervorgerufen werden [29]. Patienten, die einen methylierten Promotor des MGMT-Gens aufweisen, profitieren dadurch signifikant besser von der Therapie mit TMZ und Bestrahlung, da ihre Tumorzellen die hierbei entstehenden DNA-Schäden nicht mehr ausreichend reparieren können [30].

Bei Patienten über 70 Jahren hat sich ein verkürztes Behandlungsschema etabliert, um die körperliche Belastung zu reduzieren. Die Gesamtdosis beträgt hier im Vergleich zur Standardtherapie meist nur 40 Gy [31]. In Abhängigkeit vom Allgemeinzustand der Patienten kann auch eine alleinige Bestrahlung oder Chemotherapie erfolgen [32]. Für die progrediente bzw. rezidivierende Situation ist keine Standardtherapie in den Leitlinien der Deutschen Gesellschaft für Neurologie (DGN) definiert. Optional ist hier eine Reoperation des Tumors, alleinige Radiotherapie oder Chemotherapie, Letzteres vorzugsweise im Rahmen einer Studienteilnahme [33].

Immuntherapie

Das GBM hat, wie viele andere Tumorentitäten, Strategien entwickelt, um dem körpereigenen Immunsystem zu entgehen und die erfolgreiche Bekämpfung der entarteten Zellen zu verhindern [34]. PD-L1 (*Programmed cell death 1 ligand 1*) ist ein immunsuppressives Protein und wird unter anderem in Mikroglia und in Astrozyten exprimiert [35]. Unter physiologischen Bedingungen bindet PD-L1 an seinen auf T-Zellen exprimierten Rezeptor PD-1, wodurch die entsprechenden Zellen als körpereigen erkannt werden. So verhindert der PD-1/PD-L1-Signalweg als Immuncheckpoint die Entstehung von Autoimmunreaktionen und unnötig starken T-Zell-Antworten und ist damit entscheidend für die Aufrechterhaltung eines immunologischen Gleichgewichts [36]. GBM-Zellen, wie auch andere Tumorzellen, nutzen die Expression von PD-L1 auf ihrer Oberfläche, um einem

Angriff durch das Immunsystem des Patienten zu entgehen. Eine Metaanalyse konnte zeigen, dass eine erhöhte PD-L1-Expression im GBM mit einem schlechteren Gesamtüberleben und damit einer schlechteren Prognose korreliert [37]. Das ist dadurch erklärbar, dass die erhöhte Aktivität des PD-1/PD-L1-Signalweges eine Inhibition der T-Zellen zur Folge hat. Das wiederum führt auch zu einer geringeren Anzahl zytotoxischer T-Zellen, die normalerweise entartete Zellen eliminieren würden [38]. In einem orthotopen Mausmodell konnte bereits 2013 ein lebensverlängernder Effekt der Kombinationstherapie aus Bestrahlung und PD-1-Blockade gezeigt werden [39]. Für die Entdeckung von PD-1 und seiner Bedeutung als therapeutisches Zielmolekül für Checkpoint-Inhibitoren wurde Tasuku Honjo und James P. Allison 2018 der Nobelpreis für Physiologie oder Medizin verliehen. Neben PD-1/PD-L1 ist CTLA-4 ein vielversprechendes Ziel von Checkpoint-Inhibitoren, die zur Behandlung einiger Tumorerkrankungen bereits erfolgreich eingesetzt werden. Nivolumab, ein monoklonaler Antikörper gegen PD-1, findet Anwendung beim metastasierten Melanom [40] und beim fortgeschrittenen oder metastasierten nicht-kleinzelligen Lungenkarzinom (NSCLC) [41]. Ipilimumab ist ein gegen CTLA-4 gerichteter Antikörper, welcher häufig in Kombination mit Nivolumab eingesetzt wird, so unter anderem auch im Melanom, im NSCLC und im fortgeschrittenen Nierenzellkarzinom [42,43]. Trotz eines großen Vorteils für das Gesamtüberleben in den eben genannten Entitäten, zeigt sich das GBM in verschiedenen Studien weitgehend resistent gegen diese Checkpoint-Inhibitoren [44–46].

Heterogenität im GBM

Ein charakteristisches Merkmal des GBMs und gleichzeitig eine der größten Herausforderungen für eine erfolgreiche Therapie ist seine Heterogenität, sowohl histopathologisch innerhalb eines Tumors als auch zwischen den Tumoren verschiedener Patienten [47]. Daraus ergibt sich auch die Herkunft des Namenszusatzes *multiforme*, was sich am besten mit „vielfältig“ übersetzen lässt.

Darwins Theorie von der natürlichen Selektion und klonalen Evolution kann als Erklärung für die Entstehung von Tumorheterogenität herangezogen werden. Demnach häufen Tumorzellen genetische Veränderungen an, die ihnen einen Proliferationsvorteil verschaffen und zu Therapieresistenzen führen. So überleben nur diejenigen Klone, die am besten angepasst sind [48,49]. Solche Mutationen, die dem Tumor einen Wachstumsvorteil verschaffen und Tumorprogression begünstigen, werden als Treibermutationen (*driver mutation*) bezeichnet [50]. Die Stammzelltheorie, eine weitere Theorie, um Tumorheterogenität zu erklären, geht davon aus, dass es eine kleine Population von Tumorzellen gibt, die ein kontinuierliches Proliferationspotential haben und Klone mit

unterschiedlichen genetischen Eigenschaften hervorbringen [51,52]. Durch die Untersuchung von GBM-Proben aus humanen Patienten konnte nachgewiesen werden, dass verschiedene Klone ein unterschiedliches Ansprechen auf die Therapie zeigen. So wurden in unbehandeltem Gewebe bereits Zellen gefunden, die resistent gegen eine Behandlung mit TMZ waren [53].

Mit fortschreitender Entwicklung der Analysemöglichkeiten, konnte die Heterogenität nicht mehr nur unter histologischen Aspekten betrachtet, sondern auch auf molekularer Ebene untersucht werden. So wurden im Jahr 2006 durch Genexpressionsanalysen erstmals molekulare Subtypen des GBMs definiert – der proneurale, mesenchymale und proliferative Subtyp [54]. Vier Jahre später kam der neurale Subtyp dazu [55], der aber mittlerweile als Kontamination mit gesunden Zellen erkannt wurde, sodass GBMs aktuell in den proneuralen, mesenchymalen und klassischen Subtyp klassifiziert werden [56]. Da es jedoch bisher keine zielgerichteten Behandlungsstrategien gibt, die explizit einen bestimmten Subtyp adressieren, ist noch offen, inwieweit die Klassifizierung für die Behandlung von Patienten zukünftig relevant sein wird [57]. Hinzu kommt, dass sich nicht alle GBMs eindeutig einem Typ zuordnen lassen und im Laufe der Tumorprogression und Rezidivbildung ein Wechsel des Subtyps erfolgen kann [56]. Für die Prognosestellung kann die Einordnung aber durchaus von Bedeutung sein. Im Vergleich zum proneuralen GBM haben Patienten mit einem mesenchymalen GBM beispielsweise eine schlechtere Prognose, da dieser Subtyp häufig eine Resistenz gegen die Behandlung mit TMZ und generell eine höhere Invasivität zeigt [58]. Aufgrund dieser Eigenschaften ist ein besseres Verständnis insbesondere für das mesenchymale GBM Gegenstand aktueller Forschung, auch im Hinblick auf spezifische Therapieoptionen.

Individualisierte Therapie

Wie im vorangegangenen Kapitel beschrieben, ist Krebs nicht gleich Krebs. Die Heterogenität stellt eine große Herausforderung für die erfolgreiche Therapie einer Tumorerkrankung dar, da sich Tumore der gleichen Entität zwischen einzelnen Patienten stark unterscheiden können. Das hat zur Folge, dass Patienten unterschiedlich gut von einer gewählten Behandlung profitieren. Um dieses Phänomen zu adressieren, ist eine individualisierte Therapie von Krebspatienten das große Ziel. Eine wichtige Voraussetzung für die Etablierung einer personalisierten Medizin ist die Identifikation von Biomarkern. Mit Hilfe der Genomsequenzierung ist es möglich, potenzielle Biomarker in der DNA eines Patienten zu finden und diese möglichst zielgerichtet mit einer Therapie zu erreichen. Aus diesem Grund spricht man auch von molekular gesteuerter Medizin [59]. Die immer günstigere und schnellere Sequenzierung der DNA führte zur Identifikation zahlreicher

Treibermutationen und damit zu potenziellen Kandidaten für Behandlungsstrategien in verschiedenen Tumorarten. Das Potenzial der zielgerichteten Therapien zeigt sich am Beispiel des nichtkleinzelligen Lungenkarzinoms (NSCLC). Bei bis zu 80 % dieser Tumore lassen sich Treibermutationen identifizieren, die für eine molekular gesteuerte Behandlung zugänglich sind [60,61]. Einige Medikamente, die spezifisch gegen solche Mutationen eingesetzt werden, sind Erlotinib (EGFR Mutation), Crizotinib (ALK Mutation) oder Lorlatinib (ROS1 und ALK Mutation) [62]. Positive Aspekte sind hier nicht nur ein verlängertes Überleben der Patienten, sondern auch eine bessere Symptomkontrolle mit verbesserter Lebensqualität [63–65]. Obwohl auch beim GBM bereits zahlreiche Biomarker identifiziert werden konnten, resultieren daraus bisher keine erfolgreichen Behandlungsstrategien. Bevacizumab, ein monoklonaler Antikörper gegen VEGF, konnte keinen Überlebensvorteil gegenüber der Standardbehandlung liefern [66]. Auch Rindopepimut, welches sich gegen die EGFR Mutation EGFRvIII richtet, brachte in einer Phase III-Studie keinen Vorteil im neu diagnostizierten GBM [67]. Die aktuell laufende Phase I/II-Studie NCT Neuro Master Match (N2M2) verfolgt das Ziel der Untersuchung verschiedener zielgerichteter Therapien in einer Kohorte von Patienten mit neu diagnostiziertem GBM mit unmethyliertem MGMT-Promotor [68]. Damit ist sie eine der ersten Betrachtungen einer selektierten Patientenkollektiv. Erste Ergebnisse der Studie werden 2023 erwartet und könnten wegweisend sein für eine individualisierte Therapie beim GBM.

RNA-Sequenzierung

Die Zellen des menschlichen Körpers tragen alle die gleiche DNA und somit die identischen Gene in sich. Je nach Gewebetyp üben sie aber sehr verschiedene Funktionen aus und unterscheiden sich sowohl in ihrer Morphologie als auch in ihren Eigenschaften. Der Grund dafür ist die unterschiedliche Expression von Genen – das Transkriptom. Die RNA-Sequenzierung ist eine Methode, um das Transkriptom von Zellen sichtbar zu machen [69]. Neben der Identifikation von Spleißvarianten und anderen post-transkriptionalen Veränderungen ist der Vergleich von Expressionswerten unter verschiedenen Bedingungen das wichtigste Einsatzgebiet der RNA-Sequenzierung [69]. Da die RNA-Sequenzierung zu den Methoden des *Next Generation Sequencing* und damit zu einer neuen Generation der Sequenziertechnik gehört, zeichnet sie sich durch eine hohe Durchsatzrate mit hoher Auflösung aus [69]. Eine Vielzahl von Firmen entwickelte diverse Geräte und Techniken, um Sequenzierungen zu realisieren. Da für die vorliegende Arbeit mit einem HiSeq 2500 von Illumina sequenziert wurde, werde ich die Technik auch anhand der dort verwendeten Methodik des *Sequencing by Synthesis* beschreiben.

Bevor mit der Sequenzierung begonnen werden kann, muss die ribosomale RNA aus der Probe entfernt werden, da sie sonst das Ergebnis verfälschen würde. Hierfür verwendet man entsprechende kommerziell verfügbare Kits. Um das Transkriptom sequenzieren zu können, wird zunächst die aus Zellen oder Gewebe extrahierte RNA in cDNA umgeschrieben. Anschließend findet eine DNA-Sequenzierung statt. Da die Leselänge limitiert ist, wird die DNA in circa 300 bp lange Fragmente zerkleinert. Nun erfolgt die Ligation von Adapters an beiden Enden der Fragmente. Die Adapter ermöglichen eine Bindung der DNA-Fragmente auf einer Platte, der so genannten *Flow Cell*. Auf der *Flow Cell* sind außerdem Primer gebunden, deren Sequenz komplementär zu den verwendeten Adapters ist. Die bisher freien Enden der Fragmente binden an die Primer und bilden Brücken, weshalb man diesen Schritt auch als Brücken-PCR bezeichnet. Nach Zugabe einer DNA-Polymerase werden komplementäre Strände synthetisiert und diese durch Erhöhung der Temperatur anschließend wieder denaturiert und voneinander getrennt. Die beiden komplementären Strände nennt man *forward* und *reverse* Strang und bieten den Vorteil, dass auffällige Sequenzen auf dem jeweils anderen Strang kontrolliert werden können. Auf diese Weise können eventuell auftretende Artefakte als solche identifiziert werden. Der Vorgang der Synthese und anschließenden Denaturierung wird in mehreren Zyklen wiederholt, sodass auf der *Flow Cell* Cluster von identischen Nukleotidsträngen entstehen. So können auch Transkripte nachgewiesen werden, die nur in sehr geringer Zahl in der Ausgangsprobe vorliegen. Danach beginnt die eigentliche Sequenzierung. Durch die Zugabe der Polymerase, Primer und markierter Desoxynukleosidtriphosphate (dNTPs) findet eine erneute Synthese der einzelnen Strände statt. Nach jedem Einbau eines dNTPs wird die Synthese gestoppt und über die Anregung mit einem Laser kann detektiert werden, wo in welchem Schritt welches dNTP eingebaut wurde. Auf diese Weise werden die Sequenzen der einzelnen Fragmente bestimmt [70]. Je nach gewählter Sequenziertiefe entstehen sehr große Datenmengen, die eine Herausforderung für die anschließende Analyse darstellen. Zunächst wird die erhaltene Sequenz mit dem Referenzgenom, hier dem humanen Genom, abgeglichen und jedes Fragment wird seiner Stelle im Genom zugeordnet. Im Zuge dieser primären Analyse erfolgen auch Qualitätskontrollen, um die Verlässlichkeit der Ergebnisse zu sichern. Die sekundäre Analyse konzentriert sich auf die Detektion von Unterschieden zwischen dem zu untersuchenden Genom und dem Referenzgenom. Je nach Fragestellung kann im weiteren Verlauf zudem die Expression zwischen verschiedenen Konditionen verglichen werden. Insbesondere der große Anteil nicht-kodierender RNAs enthält eine noch nicht abschätzbare Menge an Informationen und ist Gegenstand intensiver Forschung. In der hier vorliegenden Arbeit habe ich mich auf kodierende Transkripte fokussiert und auf deren unterschiedliche Expression in behandelten und unbehandelten GBM-Gewebekulturen.

Modelle in der Krebsforschung

Die präklinische Krebsforschung bedient sich verschiedener Modelle, um die jeweilige Tumorentität möglichst realistisch untersuchen zu können. Zellkulturmodelle basieren häufig auf immortalisierten Zelllinien oder Primärzellen, die aus humanen Patientenproben gewonnen wurden. Diese Modelle sind leicht und kostengünstig zu halten und bieten den Vorteil, viele Experimente in kurzer Zeit durchführen zu können. Durch die Subkultivierung der Zellen erhält man Ergebnisse mit geringer Schwankung und benötigt weniger Wiederholungen der Versuche. Jedoch findet mit zunehmender Kultivierungsdauer eine Selektion innerhalb der Zellpopulation statt, sodass sich der Charakter der Kulturen verändern und vom Originaltumor entfernen kann [71]. Zudem fehlt bei Zellkulturen gänzlich die Kommunikation und der Austausch mit den umgebenden Zellen im Organismus, wie beispielsweise Immunzellen und es erfolgt keine Versorgung über Blutgefäße. Systemische Effekte von therapeutischen Ansätzen zu untersuchen, ist daher in diesem Modell unmöglich. Diese Nachteile werden unter anderem mit Tiermodellen adressiert, die hinsichtlich des intakten Gewebeverbandes, einer höheren Variabilität von Zelltypen, Organen und einem funktionierenden Blutkreislauf einen großen Vorteil bieten. Allerdings scheitern sie häufig an der erfolgreichen Übertragbarkeit der Ergebnisse in ein klinisches Setting für humane Patienten, da es zum Teil gravierende Speziesunterschiede zwischen Menschen und Tieren gibt. Ein fatales Beispiel für die Übertragung von Ergebnissen aus Tierversuchen auf den Menschen zeigt die *London Tragedy* aus dem Jahr 2006. Hier wurde in einer Phase I-Studie sechs freiwilligen Probanden TGN1412, ein monoklonaler Antikörper gegen CD28, verabreicht, der zuvor erfolgreich an Primaten getestet und zur Behandlung von rheumatoider Arthritis und Leukämie in England und Deutschland zugelassen worden war [72]. Bei allen Probanden kam es nach kurzer Zeit zu einem Zytokinstorm mit Multiorganversagen in Reaktion auf TGN1412, wodurch sie viele Wochen stationär behandelt werden mussten und zum Teil nur knapp überlebten [73]. Als Zytokinstorm bezeichnet man die rasante Ausschüttung proinflammatorischer Zytokine und Chemokine wie IL-6, IL-8, CCL2, CCL5 und CXCL9 [74]. Der Grund für diese unerwünschte Reaktion wurde danach in der Aminosäuresequenz der Transmembranregion von CD28 gefunden, die sich zwischen Menschen und Affen an nur drei Positionen unterscheidet, aber auf diese Weise das Bindungsverhalten des Antikörpers verändert. So führt er statt zu einer geringfügigen Produktion proinflammatorischer Zytokine zu einer extremen Ausschüttung mit den bereits beschriebenen Folgen [75]. Am Institut für Anatomie der Universität Leipzig konnte an organotypischen Schnittkulturen aus Tonsillengewebe später genau diese Reaktion beobachtet werden, wohingegen Einzelzellkulturen aus Immunzellen diese nicht zeigten [I. Bechmann, persönliche Kommunikation]. Hier zeigt sich also ein klarer Vorteil von

Gewebe- gegenüber Zellkulturen und zugleich die Problematik von Tierversuchen und ihrer klinischen Translation.

Um Interspeziesunterschiede zu reduzieren und die klinische Translation voranzutreiben, wurden Modelle mit Xenografts aus Patientengewebe (*patient-derived xenograft*, PDX) entwickelt [76]. Als Xenografts bezeichnet man Transplantate zwischen verschiedenen Spezies. Im konkreten Fall des PDX-Modells der Krebsforschung werden Tumorgewebe oder -zellen aus Patienten entnommen, aufbereitet und in Versuchstiere (meist Maus oder Ratte) eingebracht, wo sie solide Tumore bilden, die im Folgenden experimentell untersucht werden können. Dabei nutzt man den Organismus des Nagers, erhält aber trotzdem die Eigenschaften des ursprünglichen Tumors. Um eine Abstoßung des eingebrachten humanen Gewebes zu verhindern, verwendet man immunsupprimierte Tiere [77,78], wodurch auch in diesen Modellen die Interaktion des Tumors mit dem körpereigenen Immunsystem fehlt. Gerade im Hinblick auf die Erforschung von Immuntherapien stellt dies eine deutliche Einschränkung dar. Ein weiterer Nachteil dieses experimentellen Modells ist zudem, dass die Haltung der Tiere teuer und zeitintensiv ist und die Bildung von Tumoren in ausreichender Größe verhältnismäßig lange dauert und mit erheblichem Tierleid verbunden sein kann.

Einen weiteren Ansatz, um Speziesunterschiede zu umgehen und dem 3R-Prinzip folgend den Einsatz von Versuchstieren zu reduzieren, aber trotzdem die Arbeit mit dem Originalgewebe zu ermöglichen, stellen organotypische Schnittkulturen dar. Dieses Modell soll im folgenden Kapitel vorgestellt werden.

Schnittkulturen aus Patientengewebe

Das 3R-Prinzip wurde 1959 von den beiden Biologen William Russell und Rex Burch erstmals veröffentlicht und gilt bis heute als ethische Richtlinie für die Durchführung von Tierversuchen [79]. Die drei R stehen für *Replacement* – den Ersatz von Tierversuchen durch alternative Modelle, *Reduction* – die Reduzierung der Anzahl verwendeter Versuchstiere und *Refinement* – die Verbesserung der Bedingungen für die Tiere im Versuch. Ein Modell, welches Tierversuche ersetzen soll, also dem *Replacement* zugeordnet wird, stellen die organotypischen Schnittkulturen dar. In der neurowissenschaftlichen Forschung wurden bereits vor über 30 Jahren hippocampale Schnittkulturen etabliert [80]. Hierfür wird das Gehirn neonataler Nager in 350 µm dicke Scheiben geschnitten, die anschließend über mehrere Wochen hinweg auf einer Membran an einer Medium-Luft-Grenze erhalten werden können. Da auch die im Hippocampus parallel verlaufenden Fasertrakte erhalten bleiben, erlaubt das Modell die Untersuchung von Erregungsleitung oder dem Verhalten der Mikroglia [81,82]. Das Prinzip der Schnittkulturen lässt sich sehr gut auch auf humanes Gewebe übertragen. Da Tumorgewebe ohnehin oft operativ entnommen

werden muss, entsteht in dem Fall kein Mehraufwand und auch keine zusätzliche Belastung für den Patienten. Versuche mit Schnittkulturen aus GBM-Gewebe konnten zeigen, dass der Gewebeverband für mindestens zwei Wochen gut erhalten wird, es nur geringe Zellverluste gibt und neben Tumorzellen auch Astrozyten, Immunzellen und die extrazelluläre Matrix erhalten bleiben [83,84]. Neben den Schnittkulturen aus GBM-Gewebe ist es auch möglich, derartige Kulturen aus anderen soliden Tumoren anzulegen. Gezeigt wurde dies unter anderem für Kopf-Hals-Tumoren [85], kolorektale Karzinome [86], Magenkarzinome und Karzinome des gastroösophagealen Übergangs [87]. Während der Kultivierungszeit kann man Behandlungseffekte untersuchen und so auch neuartige Therapieansätze testen oder die Effektivität verschiedener Behandlungen vergleichen. Doch das Schnittkulturmodell bietet nicht nur Vorteile. Im Fall von Hirntumoren ist es beispielsweise nicht möglich, gesundes Gewebe mit Tumorgewebe zu vergleichen. Zudem ist die Menge des erhaltenen Gewebes oft stark limitiert, was wiederum die Anzahl biologischer Replikate und experimenteller Konditionen einschränkt.

Zielstellung der Arbeit

Da Forschung an Hirntumoren bisher meist an Tiermodellen durchgeführt wurde und die Übertragung der damit erzeugten Ergebnisse oft an interspezifischen Unterschieden zwischen Nagern und Menschen scheitert, wurde das Modell der organotypischen Schnittkulturen entwickelt. Dieses Modell ermöglicht, die Situation im Patienten *in vitro* zu simulieren, Behandlungseffekte zu untersuchen und damit Rückschlüsse auf die Effektivität einer Behandlung zu ziehen. Zunächst beschränkte sich die postexperimentelle Analyse der Kulturen auf die manuelle Auswertung histologischer Färbungen. Um das methodische Spektrum der Schnittkulturen zu erweitern und damit die Anwendbarkeit als präklinisches Testsystem weiter zu untersuchen, sollten in der hier vorliegenden Promotionsarbeit Schnittkulturen aus GBM-Gewebe von 25 Patienten angelegt und mit der Standardtherapie (TMZ + Bestrahlung) behandelt werden. Um die Analyse der histologischen Färbungen zu beschleunigen und zu objektivieren, sollte ein automatisierter Ansatz entwickelt werden. Behandlungseffekte auf transkriptioneller Ebene sollten mittels RNA-Sequenzierung adressiert werden. Hierfür musste zunächst geklärt werden, ob es technisch überhaupt möglich ist, aus dem zum Teil stark nekrotischen GBM-Gewebe, RNA in ausreichender Qualität zu gewinnen. Weiterhin sollte die Frage beantwortet werden, wie gut die Reproduzierbarkeit ist und inwieweit die Heterogenität des Gewebes die Vergleichbarkeit der Ergebnisse beeinflusst. Um die erhobenen Daten mit dem klinischen Verlauf der jeweiligen Patienten korrelieren zu können, wurde in regelmäßigen Abständen der Status der Patienten abgefragt. Hierbei sollte unter anderem besonderes Augenmerk darauf liegen, ob die Patienten im klinischen Verlauf tatsächlich mit der Standardtherapie behandelt worden sind, um eine Vergleichbarkeit zu gewährleisten. Bei 18 der insgesamt untersuchten 25 Patienten war dies der Fall und sie sind in die Analyse der Metadaten eingeflossen.

Folgende zentrale Fragen ergeben sich aus der Zielstellung der Arbeit:

- ❖ Ist es möglich, aus den kultivierten Gewebeschnitten RNA zu gewinnen?
- ❖ Kann man in dem kultivierten Gewebe Behandlungseffekte detektieren?
- ❖ Kann die Quantifizierung histologischer Färbungen automatisiert erfolgen?
- ❖ Wird die intra- und intertumorale Heterogenität des GBMs mit der Verwendung von zwei bis drei technischen/biologischen Replikaten ausreichend adressiert?
- ❖ Ist es möglich, die beobachteten Behandlungseffekte mit dem klinischen Verlauf der Patienten zu korrelieren?
- ❖ Bilden die organotypischen Schnittkulturen ein realistisches Abbild der Situation im Patienten?

Publikation I

Deep sequencing and automated histochemistry of human tissue slice cultures improve their usability as preclinical model for cancer research

Susann Haehnel¹, Kristin Reiche², Dennis Loeffler², Andreas Horn¹, Conny Blumert², Sven-Holger Puppel², Nicole Kaiser¹, Felicitas Rapp³, Michael Rade², Friedemann Horn^{2,4}, Juergen Meixensberger⁵, Ingo Bechmann¹, Frank Gaunitz^{5,6} & Karsten Winter^{1,6}

¹Institute of Anatomy, University of Leipzig, Faculty of Medicine, Leipzig, Germany

²Department of Diagnostics, Fraunhofer Institute of Cell Therapy and Immunology, Leipzig, Germany

³GSI Helmholtzzentrum für Schwerionenforschung GmbH, Darmstadt, Germany

⁴Institute of Clinical Immunology, University of Leipzig, Faculty of Medicine, Leipzig, Germany

⁵Department of Neurosurgery, University Hospital Leipzig, Leipzig, Germany

⁶These authors contributed equally as senior authors: Frank Gaunitz and Karsten Winter

OPEN

Deep sequencing and automated histochemistry of human tissue slice cultures improve their usability as preclinical model for cancer research

Susann Haehnel^{1*}, Kristin Reiche², Dennis Loeffler², Andreas Horn¹, Conny Blumert², Sven-Holger Puppel², Nicole Kaiser¹, Felicitas Rapp¹, Michael Rade¹, Friedemann Horn^{2,4}, Juergen Meixensberger⁵, Ingo Bechmann¹, Frank Gaunitz^{5,6} & Karsten Winter^{1,6}

Cancer research requires models closely resembling the tumor in the patient. Human tissue cultures can overcome interspecies limitations of animal models or the loss of tissue architecture in *in vitro* models. However, analysis of tissue slices is often limited to histology. Here, we demonstrate that slices are also suitable for whole transcriptome sequencing and present a method for automated histochemistry of whole slices. Tumor and peritumoral tissue from a patient with glioblastoma was processed to slice cultures, which were treated with standard therapy including temozolomide and X-irradiation. Then, RNA sequencing and automated histochemistry were performed. RNA sequencing was successfully accomplished with a sequencing depth of 243 to 368×10^6 reads per sample. Comparing tumor and peritumoral tissue, we identified 1888 genes significantly downregulated and 2382 genes upregulated in tumor. Treatment significantly downregulated 2017 genes, whereas 1399 genes were upregulated. Pathway analysis revealed changes in the expression profile of treated glioblastoma tissue pointing towards downregulated proliferation. This was confirmed by automated analysis of whole tissue slices stained for Ki67. In conclusion, we demonstrate that RNA sequencing of tissue slices is possible and that histochemical analysis of whole tissue slices can be automated which increases the usability of this preclinical model.

Cancer constitutes an enormous burden on societies worldwide. Despite achievements, rendering some types of cancer curable, the overall occurrence of cancer is increasing because of growth and aging of populations¹. Research on cancer, aiming at the development of new drugs and therapeutic strategies requires models that most closely resemble the *in vivo* situation in a patient in order to have a predictive value for future treatment. Today, most models are based on (immortalized) cell lines grafted into immunosuppressed animals. Their relevance is further hampered by interspecies limitations between humans and rodents. During the last years, organotypic slice cultures derived from human tissues, including tumors, came into focus as an alternative model². These models may become a valuable alternative to animal testing not only reducing the numbers of experimental animals but also overcoming interspecies differences. In our group, we have already established slice cultures from human brains³, *Glioblastoma multiforme* (GBM)^{4,5}, head and neck squamous cell carcinoma⁶, human gastric and esophagogastric junction cancer⁷, and colorectal carcinoma⁸. Using these organotypic slice cultures, we tested, for example, effects of heavy ion therapy⁵, polyethylenimine-based nanoparticles for siRNA delivery⁹, but also novel nanostructured scaffolds for cultivation⁴.

¹Institute of Anatomy, University of Leipzig, Faculty of Medicine, Leipzig, Germany. ²Department of Diagnostics, Fraunhofer Institute of Cell Therapy and Immunology, Leipzig, Germany. ³GSI Helmholtzzentrum für Schwerionenforschung GmbH, Darmstadt, Germany. ⁴Institute of Clinical Immunology, University of Leipzig, Faculty of Medicine, Leipzig, Germany. ⁵Department of Neurosurgery, University Hospital Leipzig, Leipzig, Germany. ⁶These authors contributed equally: Frank Gaunitz and Karsten Winter. *email: su.haehnel@gmail.com

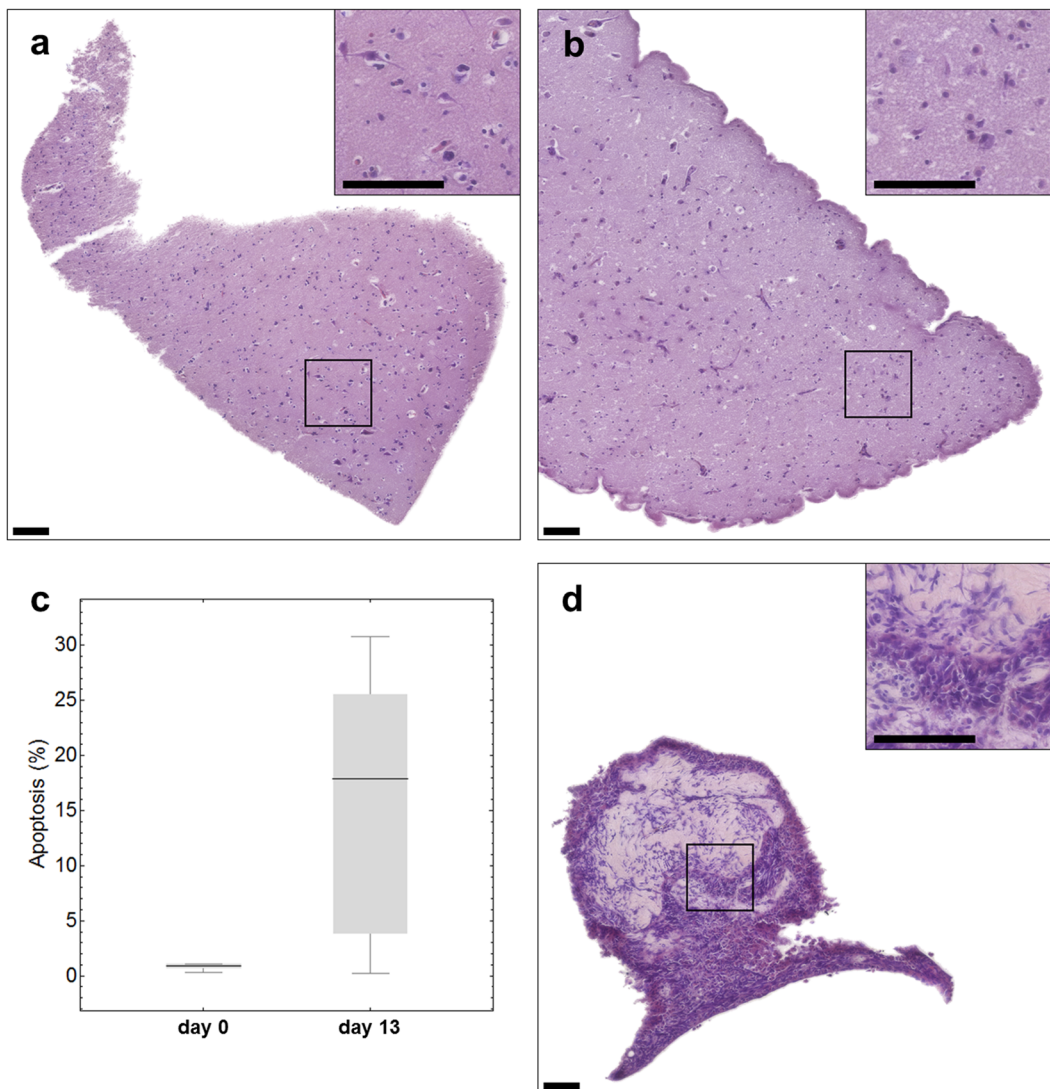


Figure 1. Histology of freshly sliced (a) or cultivated (b) tumor-surrounding brain tissue (peritumoral tissue of zone III) and cultivated GBM tissue (d). Hematoxylin (nuclei) and eosin (cytoplasm) staining was done (a) instantly after the slicing procedure or after 13 days in culture (b,d). Apoptosis rate was determined by TUNEL staining in peritumoral tissue on day 0 (left bar) and day 13 (right bar) (c). Scale bar: 100 μ m.

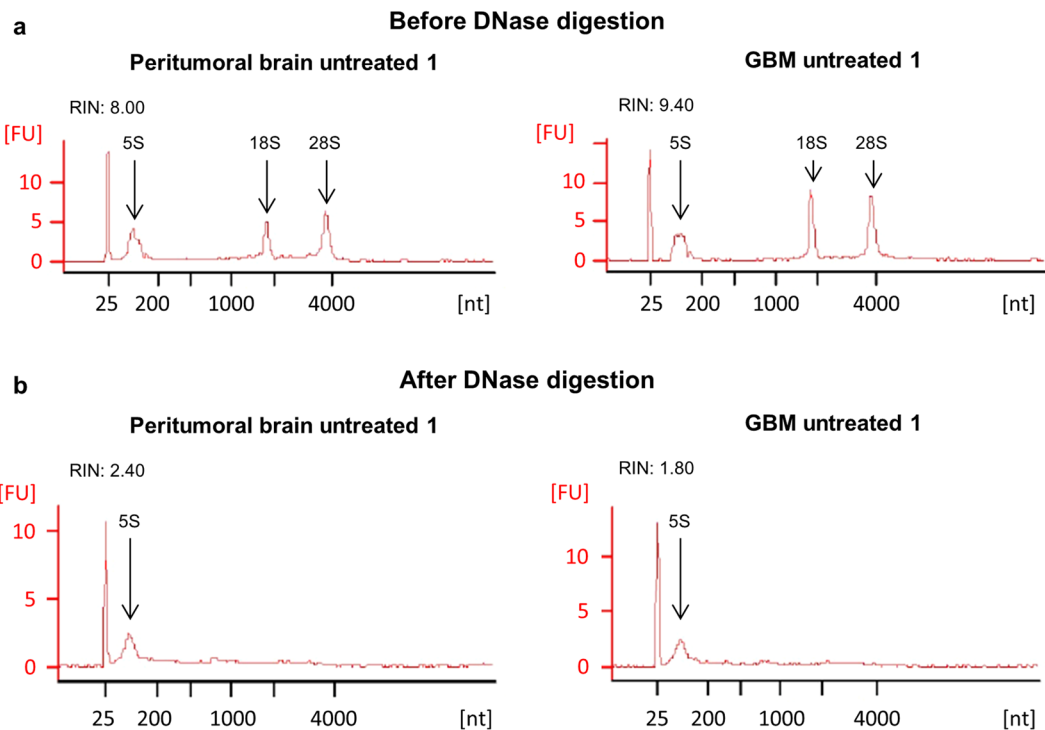
A prerequisite to use such models as clinical test system for the outcome of therapy or the selection of the most effective drug for individual patients is an unbiased, fast and automated cell counting approach allowing to start treatment within a couple of days. Moreover, whole transcriptome analysis with and without treatment would be of help for prediction, but also to better understand mechanisms of tumor progression and therapy resistance.

In order to address these two important issues, we focused on GBM slice cultures which maintain their histopathological hallmarks for at least 14 days *in vitro*⁵. GBM is the most common primary brain malignancy in adults¹⁰ with a median survival of approximately 15 months^{11,12} despite surgical resection, X-irradiation and chemotherapy with temozolomide (TMZ). We report that organotypic slice cultures are suitable for automated histological analyses as well as whole transcriptome sequencing, thereby providing an adequate alternative with regard to individualized cancer research and therapy.

Results

Tissue integrity is maintained in slice cultures during 13 days of cultivation. In order to see whether cultivation had an influence on tissue integrity, hematoxylin and eosin staining of tissue slices was performed immediately after preparation and after cultivation for 13 days. As can be seen in Fig. 1, the cell density of freshly cut peritumoral brain tissue of zone III (Fig. 1a) decreases after 13 days of cultivation (Fig. 1b). In addition, we observed an increase of apoptotic cells from 1% on day 0 to 17% on day 13 (Fig. 1c, $p = 0.034$). Despite an obvious loss of cells, this result also indicates that the tissue is maintained to a high degree. In Fig. 1d tumor tissue after 13 days of cultivation is presented. Unfortunately, the amount of material obtained from the patient was very limited. Therefore, we were not able to present a comparison of the tumor tissue from day 13 to day 0.

Sample	RNA Integrity Numbers	
	before DNase digestion	after DNase digestion
Tumor_untreated_1	9.40	1.80
Tumor_untreated_2	8.60	1.20
Tumor_TMZ+4Gy_1	9.20	2.40
Tumor_TMZ+4Gy_2	9.20	2.40
Peritumoral brain_untreated_1	8.00	2.10
Peritumoral brain_untreated_2	7.80	1.20
Peritumoral brain_TMZ+4Gy_1	8.40	2.40
Peritumoral brain_TMZ+4Gy_2	9.10	2.50

Table 1. RNA integrity number before (left) and after (right) DNase digestion.**Figure 2.** RNA quality of cultivated tissue slices. RNA quality was determined by a Bioanalyzer 2100 using the RNA 6000 Nano-Kit (Agilent Technologies) and revealed good quality before the DNase digestion was performed (a). After the DNase digestion, the RNA quality was strongly reduced (b). The left graphs show untreated peritumoral brain tissue, the right graphs the corresponding GBM tissue.

But, it should be noted that we have previously demonstrated that the individual histopathology of tissue cultures derived from glioblastoma is maintained over at least 16 days⁵.

RNA obtained from tissue slices is suitable for whole transcriptome sequencing. Next, we asked whether the RNA isolated from treated and untreated tissue slices can be further used for whole transcriptome sequencing. Therefore, RNA was isolated from peritumoral brain (zone III) and GBM tissue (zone I) either treated with TMZ and X-irradiation or left untreated. For each condition, the RNA isolated from three individual slices pooled together was collected in order to have enough material for further analyses and to overcome the tumor's heterogeneity. Using a Bioanalyzer 2100, the RNA integrity number (RIN) was determined from each sample before and after DNase digestion. The corresponding data are presented in Table 1. The higher the RIN value, the better is the RNA maintenance¹³. As can be seen in Table 1, all RIN values were ≥ 7 before the DNase digestion which demonstrates a very high RNA quality (Table 1). After DNase digestion, a severe loss of RNA quality was observed as indicated by strongly diminished RIN values (the reason for that is not known, but a contamination of the utilized chemicals with RNase could be excluded in further analyses). This loss of quality was further indicated by a loss of the characteristic peaks of the 18 s and 28 s rRNA in the corresponding chromatograms (Fig. 2). Only the peak of the 5 s rRNA still was clearly distinct (Fig. 2b). Although RNA quality seemed to be insufficient for whole transcriptome sequencing as concluded from the RIN values determined, it should be noted that higher

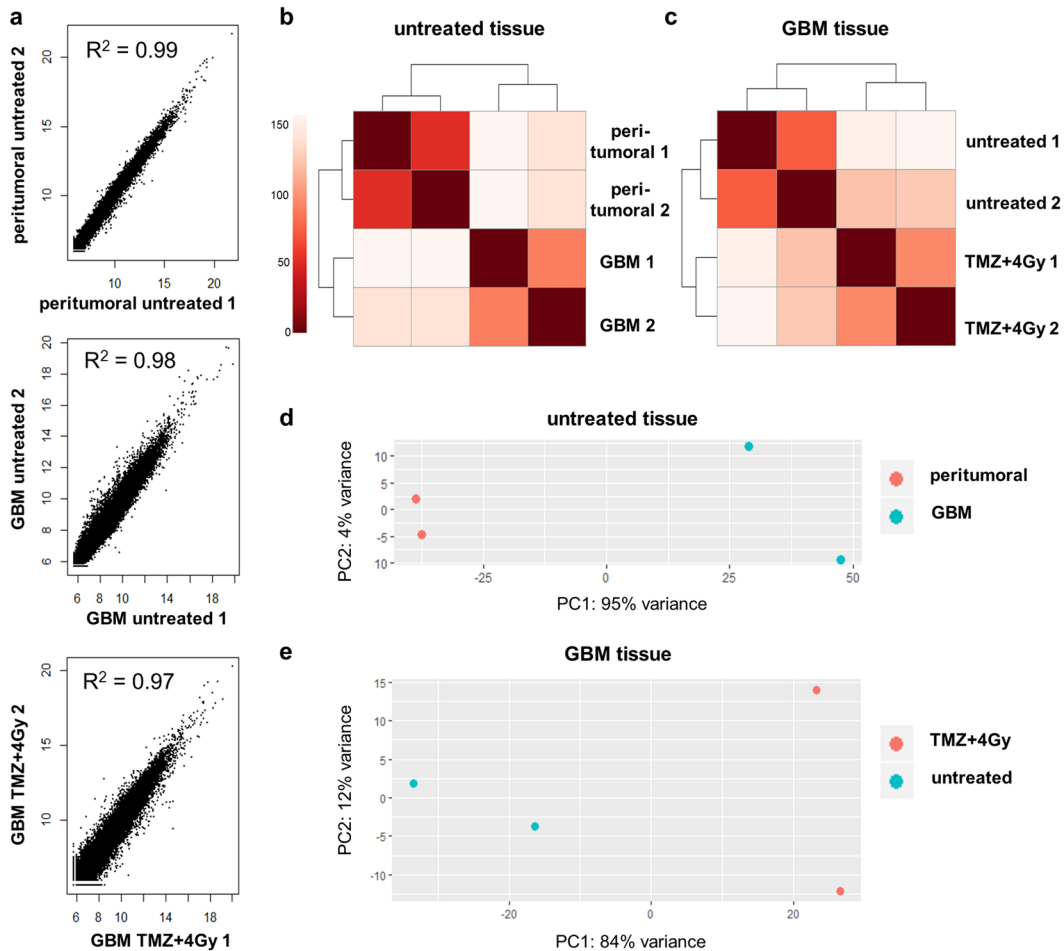


Figure 3. Comparison of gene expression between peritumoral brain and GBM tissue. **(a)** Correlation plots of variance-stabilized counts in sample duplicates (peritumoral untreated = untreated peritumoral brain tissue of zone III, GBM untreated = untreated GBM tissue of zone I, GBM TMZ + 4 Gy = GBM tissue treated with radiotherapy). The correlation coefficient represents low variability between duplicates. **(b)** Distance heatmap of Euclidean distances between untreated peritumoral brain (peritumoral) and GBM tissue (GBM). **(c)** Distance heatmap of Euclidean distances between untreated and treated (TMZ + 4 Gy) GBM tissue. **(d)** Principal Component Analysis. Untreated sample duplicates cluster together with a high variability between peritumoral brain and GBM tissue. **(e)** Principal Component Analysis. GBM sample duplicates show differences between untreated and treated (TMZ + 4 Gy) GBM tissue.

RINs are only necessary for transcriptome sequencing of poly(A) RNA. In our experiments total RNA sequencing was performed which even allows using RNA from FFPE tissue with RINs worse than those presented in our data^{14–16}. In fact, next generation sequencing was performed successfully. Library preparation and sequencing resulted in sequencing depths from 243 to 368 $\times 10^6$ reads per sample. For unknown reasons, this was not the case for one duplicate of treated peritumoral brain tissue (zone III) although respective RIN values were even better than those obtained from other slices (Table 1). Our data clearly demonstrate that whole transcriptome sequencing from slice cultures is possible.

Technical replicates reveal a high consistency of sequencing data. As described in the preceding paragraph, the whole transcriptome sequencing from RNA isolated from tissue slices was successful. The next question to be answered was how consistent the results were among individual experimental replicates. To this end, the data obtained by separate sequencing experiments from two slice pools (three slices were pooled in each approach) for each condition and tissue type were compared. The linear correlation coefficient R^2 of variance-stabilized counts was calculated for each pair (Fig. 3a). For all three sample pairs, the correlation coefficient was close to 1, so that a linear correlation between the duplicates could be assumed. As expected, the variance within the GBM samples was slightly higher than in the peritumoral brain samples (Fig. 3a,d) probably due to high intra-tumor heterogeneity which is well-known for GBM¹⁷. The heatmaps (R package “pheatmap” with default parameters) of the pairwise Euclidean distances of variance-stabilized counts show that the sample duplicates cluster together but clearly separate from the other tissue samples and conditions (Fig. 3b,c). The principal

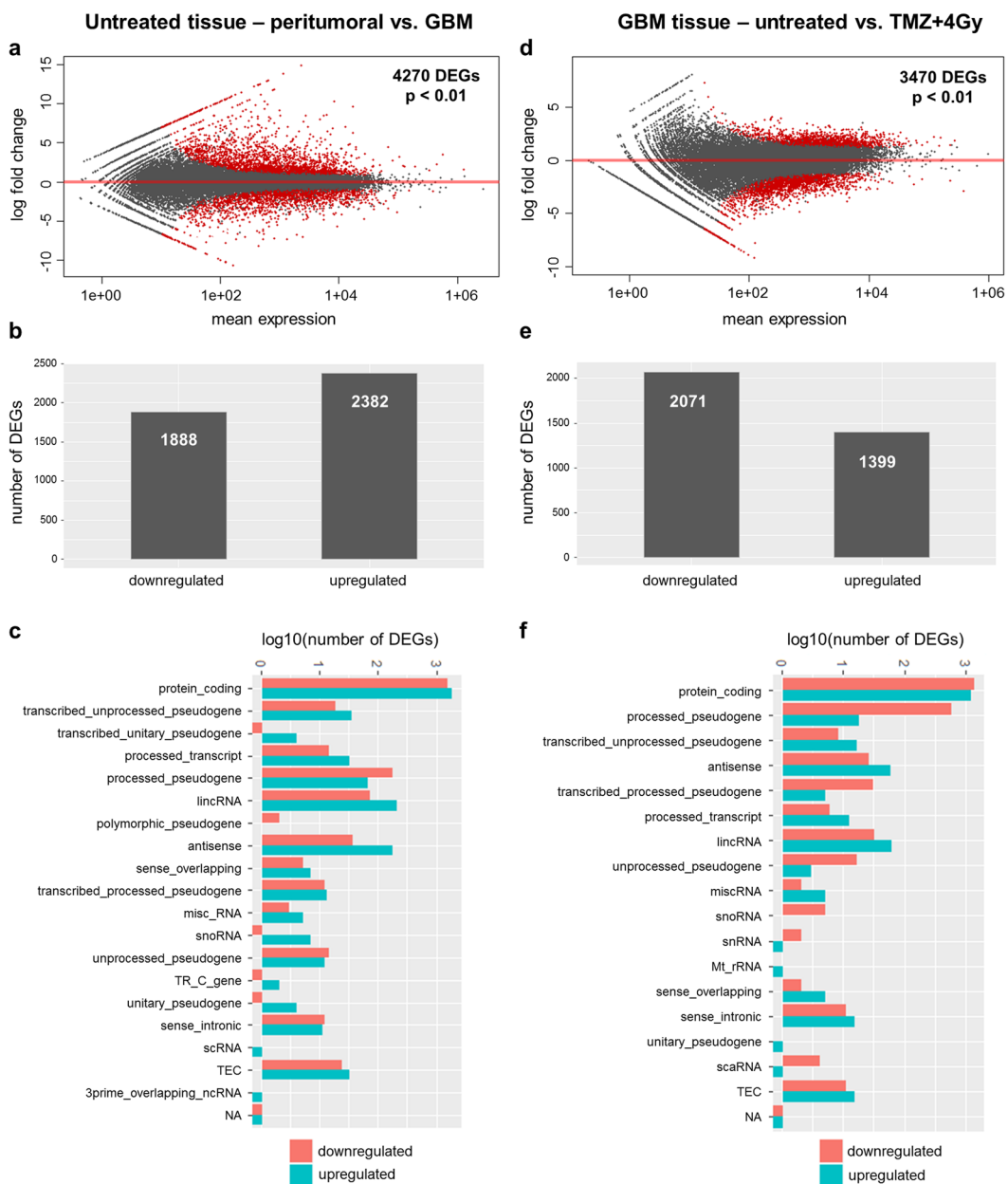


Figure 4. Differentially expressed genes (DEGs) between peritumoral brain and GBM tissue. Analysis of differentially expressed genes (DEGs) between untreated peritumoral brain tissue of zone III and GBM tissue samples of zone I (**a–c**) and between untreated and treated GBM samples (**d–f**). (**a,d**) Significantly regulated transcripts are indicated in red ($p < 0.01$). (**b,e**) Number of down- and upregulated genes in both comparisons. (**c,f**) Biotype of down- (red) and upregulated (blue) transcripts in both comparisons. TEC = to be experimentally confirmed, NA = not available.

component analysis of the variance-stabilized counts confirmed these findings (Fig. 3d,e). The variance between peritumoral brain and GBM tissue was higher (Fig. 3d) than between treated and untreated GBM tissue (Fig. 3e).

Differential gene expression between peritumoral brain (zone III) and GBM tissue (zone I) and between treated and untreated GBM tissue. By the experiments presented in the preceding paragraphs it could be confirmed that the data obtained by whole transcriptome sequencing are reliable, since expression variation was reproducible between duplicates of two different tissue cultures of the same patient. To gain further insight into differential gene expression between peritumoral brain (zone III) and GBM tissue (zone I) and between treated and untreated GBM tissue, a differential gene expression analysis was done.

A calculation with DESeq2 revealed 4270 significantly differentially (FDR < 0.01) regulated transcripts between untreated peritumoral brain (zone III) and GBM tissue (zone I, Fig. 4a). 1888 of these DEGs were found to be significantly downregulated, and 2382 genes were significantly upregulated in the tumor tissue

Diseases and disorders	p-value	molecules of 3280 in total
Cancer	$1.64 \times 10^{-99} - 1.29 \times 10^{-150}$	3101
- Tumorigenesis of tissue	3.29×10^{-145}	3040
- Malignant solid tumor	1.90×10^{-139}	3084
Organismal injury and abnormalities	$1.64 \times 10^{-99} - 1.29 \times 10^{-150}$	3135
Gastrointestinal disease	$8.04 \times 10^{-10} - 1.88 \times 10^{-130}$	2822
Endocrine disorders	$1.47 \times 10^{-99} - 3.03 \times 10^{-112}$	2641
Dermatological diseases and conditions	$6.23 \times 10^{-11} - 3.08 \times 10^{-90}$	1926
Molecular and cellular functions		
Cellular development	$9.97 \times 10^{-10} - 1.91 \times 10^{-44}$	598
Cellular growth and proliferation	$9.97 \times 10^{-10} - 1.91 \times 10^{-44}$	511
- Proliferation of neuronal cells	3.25×10^{-15}	198
Cellular assembly and organization	$4.76 \times 10^{-10} - 1.90 \times 10^{-41}$	747
Cellular function and maintenance	$9.97 \times 10^{-10} - 1.90 \times 10^{-41}$	973
Cell-to-cell signaling and interaction	$1.65 \times 10^{-99} - 1.60 \times 10^{-37}$	677
Physiological system development and function		
Nervous system development and function	$1.65 \times 10^{-99} - 1.91 \times 10^{-44}$	994
Tissue development	$1.65 \times 10^{-99} - 1.91 \times 10^{-44}$	999
Embryonic development	$1.61 \times 10^{-99} - 8.66 \times 10^{-40}$	768
Organismal development	$1.65 \times 10^{-99} - 8.66 \times 10^{-40}$	1198
Tissue morphology	$1.61 \times 10^{-99} - 7.98 \times 10^{-33}$	804

Table 2. Top diseases and functions of significant differentially expressed genes in untreated peritumoral brain vs. GBM tissue.

(zone I) in comparison to the peritumoral brain (zone III, Fig. 4b). The vast majority of all DEGs belonged to the protein-coding fraction of transcripts (Fig. 4c). In addition, known human pseudogenes and non-coding RNAs represented approximately 100 DEGs both in the downregulated and in the upregulated transcripts. A corresponding comparison of untreated versus treated GBM tissue (Fig. 4f) revealed 3470 significantly regulated (FDR < 0.01) transcripts. Here, 2071 DEGs were found to be significantly downregulated and 1399 significantly upregulated in GBM tissue which had been treated in contrast to untreated samples (Fig. 4d,e).

A pathway enrichment analysis by the Ingenuity® Pathway Analysis software tool (Qiagen) revealed that the vast majority of the protein-coding genes which are significant differentially expressed between untreated peritumoral brain and GBM tissue and between untreated and treated GBM tissue are known to be associated with certain diseases and/or biological functions. Tables 2 and 3 show an excerpt of these diseases and functions with the corresponding p-values and the numbers of molecules present in both datasets of differentially expressed protein-coding genes. In peritumoral brain versus GBM tissue, 3040 of the 3280 differentially expressed protein-coding transcripts were found to be associated with the tumorigenesis of tissue (Table 2). 511 transcripts are known to play a role in cellular growth and proliferation (Table 2). In untreated versus treated GBM tissue, 2189 of the 2527 protein-coding transcripts are associated with tumorigenesis of tissue and 778 were found to be associated with cellular function and maintenance (Table 3). Further significantly enriched functions are, among others, cell death, cell and organismal survival, proliferation of tumor cells, progression of cell cycle, and cell-to-cell signaling (Tables 2 and 3).

Knowledge base analysis of expression data predicts reduced proliferation in slices after treatment which could be confirmed by automated histochemical analysis. In the previous sections it was demonstrated that whole transcriptome sequencing can be performed with tissue slices in order to reveal differences in gene expression. Now it was of interest, whether these data can be used to make predictions about possible physiological responses to treatment that can be confirmed by a second method. Therefore, we performed a knowledge base data analysis using the Ingenuity® Pathway Analysis (IPA®) software tool (Qiagen). An IPA®-generated list of genes which are described to be associated with proliferation of cancer and/or neuronal cells was compared to the significantly regulated transcripts that were found between treated and untreated GBM tissue. The analysis revealed 190 genes that were present in both lists. Further analysis indicated reduced proliferation under treatment conditions (Fig. 5b). Among the most prominent genes we identified down-regulation of *MKI67*, *SPP1*, *PDGFRA*, *FGF1*, *CXCR4*, *CD44*, *HGF* and *KIT* under the influence of treatment (Fig. 5a).

In order to confirm a negative effect on proliferation in the tumor slices of this patient under treatment, as predicted by gene expression analysis, we performed immunohistochemistry on paraffin sections derived from slices. For the analysis, a quantitative image analysis was implemented. In the experiment presented in Fig. 6, slices from peritumoral brain (zone III, Fig. 6a) and from GBM tissue (zone I, Fig. 6b) were labeled with an antibody directed against Ki67 (untreated samples are shown as example). Ki67 is a commonly used proliferation marker which is present during G1, S, G2, and mitosis but absent in G0 phase¹⁸. In addition, DAPI was used to counterstain nuclei in order to evaluate whether a Ki67-positive signal is indeed localized to a nucleus to prevent counting of unspecific signals. Figures 6a,b show the original pictures recorded by the slide scanner. In a first step,

Diseases and disorders	p-value	molecules of 2527 in total
Cancer	$6.38 \times 10^{-04} - 1.00 \times 10^{-63}$	2306
- Tumorigenesis of tissue	1.29×10^{-62}	2189
- Malignant solid tumor	4.32×10^{-58}	2263
- Glioma	5.59×10^{-04}	216
Organismal injury and abnormalities	$6.38 \times 10^{-04} - 1.00 \times 10^{-63}$	2327
Gastrointestinal disease	$4.31 \times 10^{-04} - 2.00 \times 10^{-56}$	2148
Hepatic system disease	$4.31 \times 10^{-04} - 2.09 \times 10^{-39}$	1632
Reproductive system disease	$1.93 \times 10^{-04} - 2.98 \times 10^{-36}$	1514
Molecular and cellular functions		
Gene expression	$5.07 \times 10^{-08} - 6.05 \times 10^{-13}$	514
Cellular assembly and maintenance	$6.38 \times 10^{-04} - 1.13 \times 10^{-12}$	525
Cellular function and maintenance	$3.19 \times 10^{-04} - 1.13 \times 10^{-12}$	406
Cell death and survival	$6.22 \times 10^{-04} - 1.36 \times 10^{-10}$	778
Cell cycle	$5.47 \times 10^{-04} - 5.51 \times 10^{-10}$	348
- Cell cycle progression	5.51×10^{-10}	251
- Proliferation of tumor cells	6.38×10^{-04}	99
Physiological system development		
Organismal survival	$9.88 \times 10^{-13} - 1.30 \times 10^{-13}$	554
Nervous system development and function	$5.53 \times 10^{-04} - 9.90 \times 10^{-12}$	380
Tissue morphology	$5.53 \times 10^{-04} - 1.18 \times 10^{-09}$	268
Organ morphology	$4.31 \times 10^{-04} - 1.10 \times 10^{-08}$	255
Organismal development	$4.35 \times 10^{-04} - 1.10 \times 10^{-08}$	551

Table 3. Top diseases and functions of significant differentially expressed genes in treated vs. untreated GBM tissue.

the pixel area of the whole tissue was calculated (gray masks in Fig. 6a'"/b'") as well as the DAPI-positive area (Fig. 6a';b') representing the nuclei. To determine the proliferation capacity of peritumoral brain (Fig. 6a) and GBM tissue (Fig. 6b), double-positive nuclei were analyzed (Fig. 6a'',b''). Consecutive H/E-stained sections of the tissue are shown in Fig. 6a'',b'' to demonstrate the native condition of the analyzed tissue slices. The automatic quantification revealed a statistically significant decrease of proliferating cells in treated peritumoral brain and GBM tissue compared to the untreated controls (Fig. 6c). Furthermore, GBM tissue has a high nuclei density and a small tissue area, whereas peritumoral brain tissue exhibits a larger tissue area combined with a smaller cellular density (Fig. 6d).

The results of the automated analysis were confirmed by manual analysis. Segmented areas of total tissue and DAPI were highly correlated ($R^2 = 0.998$ and $R^2 = 0.876$, respectively; all $p < 0.001$) while values for the proliferating area showed moderate correlation ($R^2 = 0.616$, $p < 0.001$) (Fig. S3).

Discussion

Despite intense research during the last decades, many cancerous diseases are still associated with a poor prognosis and a low median overall survival, e.g. 14 months for advanced non-small cell lung cancer¹⁹, 12 months for advanced gastric cancer²⁰, and 15 months for GBM¹². Therefore, the establishment of preclinical models to test newly developed drugs and treatment strategies is an important step in oncological research. As outlined in the introduction, the frequently used animal models often fail because of interspecies differences that impede clinical translation. Cell culture models, on the other hand, are far away from the *in vivo* situation as tumor tissue can be composed of a bulk of many other cell types aside from tumor cells, e.g. endothelial cells²¹, pericytes²², tumor-associated immune cells²³, and cancer stem-like cells²⁴ which is not reflected by cell culture models. As a more realistic system patient-derived xenograft models have been developed, injecting patient-derived tumor cells into immunodeficient mice²⁵. Thus, the animals generate tumors which are supposed to maintain the original tumor's biology thereby mimicking the human patient. This is, among others, well described for breast cancer²⁶, non-small cell lung cancer²⁷, or melanoma metastasis²⁸. Besides the great burden for the animals, the production of patient-derived tumors within rodents is a time-consuming method which is therefore unlikely to find its way into a clinical setting with regard to personalized cancer therapy. The immunodeficiency of these mice, which is required to inhibit the rejection of injected human tumor cells^{29,30} further impedes the successful translation into the clinics.

As an alternative to animal and cell culture models, human tissue slice cultures are now increasingly employed in cancer research^{2,31–37}. One of the major advantages of tissue slice cultures is the maintenance of the tissue topology and composition of different cell types including immune cells, as represented by microglia which play a crucial role in GBM progression^{38–40}. Therefore, slice cultures may reflect the tumor's heterogeneity far better than conventional cell culture and animal models. Yet, tumor heterogeneity is not only defined by the general presence of different cell types, but also by different characteristics of the tumor cells in different areas of the tissue⁴¹. This impedes the reproducibility of such *ex vivo* experiments and increases the difficulty of successful translation into

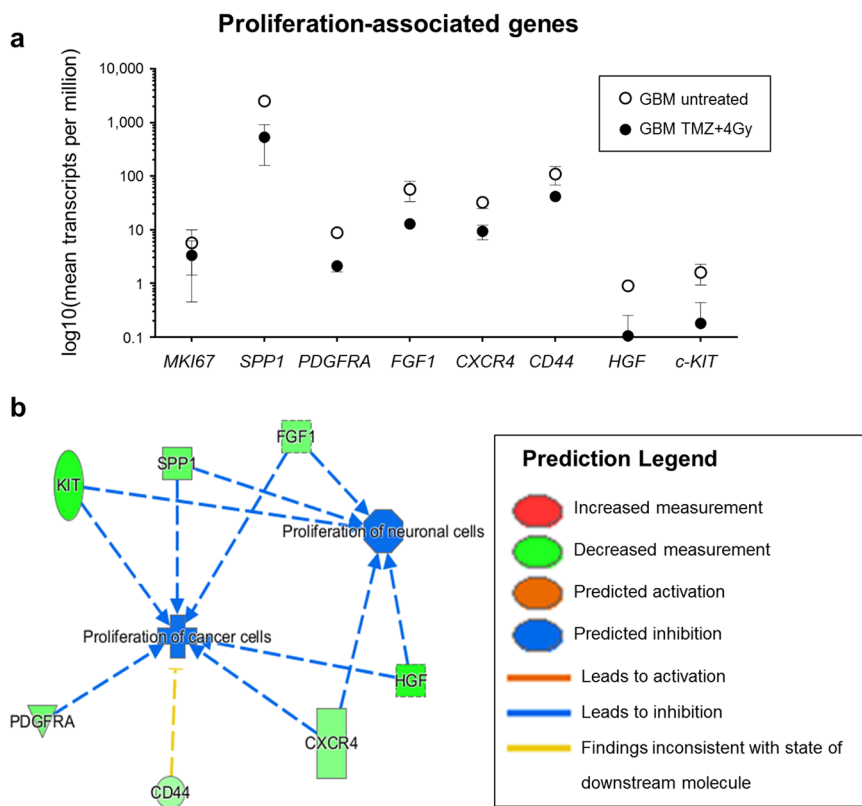


Figure 5. mRNA expression indicates an inhibition of proliferation after treatment. The differentially expressed transcripts in treated versus untreated GBM tissue were compared to a list of proliferation-associated genes obtained from the Ingenuity® Pathway Analysis (IPA®, QIAGEN). 190 genes were found to be present in both lists. Transcripts per million of some of these genes are displayed in (a). Knowledge base analysis with IPA® indicates an inhibition of proliferation of neuronal and cancer cells (b, blue lines). Green symbols represent a decreased measurement of the respective transcript.

a clinical setting for human patients. For that reason, the slices obtained from one patient are pooled together and are randomly distributed in triplicates to the membrane inserts. For RNA analysis, these slices are pooled again to diminish the possibility that the differences observed here are just resulting from a different localization within the original tumor.

For histology, single slices are embedded in paraffin and stained individually. In conventional microscopy, only parts of the whole tissue can be recorded and analyzed. Furthermore, most histological analyses are still performed “manually” which is time-consuming and investigator-dependent. In this study, as exemplified by tissue from one GBM patient, we present that whole slices can be recorded and analyzed automatically (Fig. 6). Therefore, it is possible to retrospectively draw conclusions about the extent of heterogeneity in the original tissue. The automation of the histological analysis is time-saving, objective and reproducible. That in turn increases the suitability for a clinical application of this method with regard to individualized cancer therapy. By designing the experiments in duplicate or even triplicate approaches (depending on the available amount of tissue) the results are getting even more reproducible. In addition, the RNA expression analyses presented here were performed in replicates and exhibited a very good correlation and only slight differences within each sample pair (Fig. 3). Therefore, it can be concluded that the random distribution of three slices may be sufficient to depict the intratumoral heterogeneity. Further investigations on more GBM slice cultures are currently being analyzed to confirm this finding and to verify whether this is consistent among patients.

The histological finding of reduced proliferation in treated GBM tissue is consistent with RNA expression data obtained from the same samples. Here, the same treatment-mediated effect was observed (Fig. 5a). Eight genes, which were found to be downregulated in treated compared to untreated GBM tissue and are known to be associated with proliferation of neuronal and/or cancer cells, were chosen for further analysis. This analysis revealed a downregulation of *SPP1* which has been shown to be overexpressed in grade IV gliomas and which is related to worse overall survival also in patients with lower-grade glioma⁴². Some isoforms of *SPP1* are in fact known to promote glioma cell invasion⁴³. In addition, we identified a down-regulation of *CD44* under treatment (Fig. 5c). This down-regulation may be caused by down-regulation of *SPP1* which was shown to increase the synthesis of the *CD44* variant *CD44v6* in liver cancer cells⁴⁴. *CD44* itself is known as a marker of GBM invasiveness and was shown to promote stem cell-like properties in glioma and to play a role in the mediation of resistance to radiation and chemotherapy with temozolomide^{45,46}. An increased expression of *CXCR4* is associated with the recurrence of glioblastoma after radiochemotherapy and could indicate an activation of the CXCL12-CXCR4

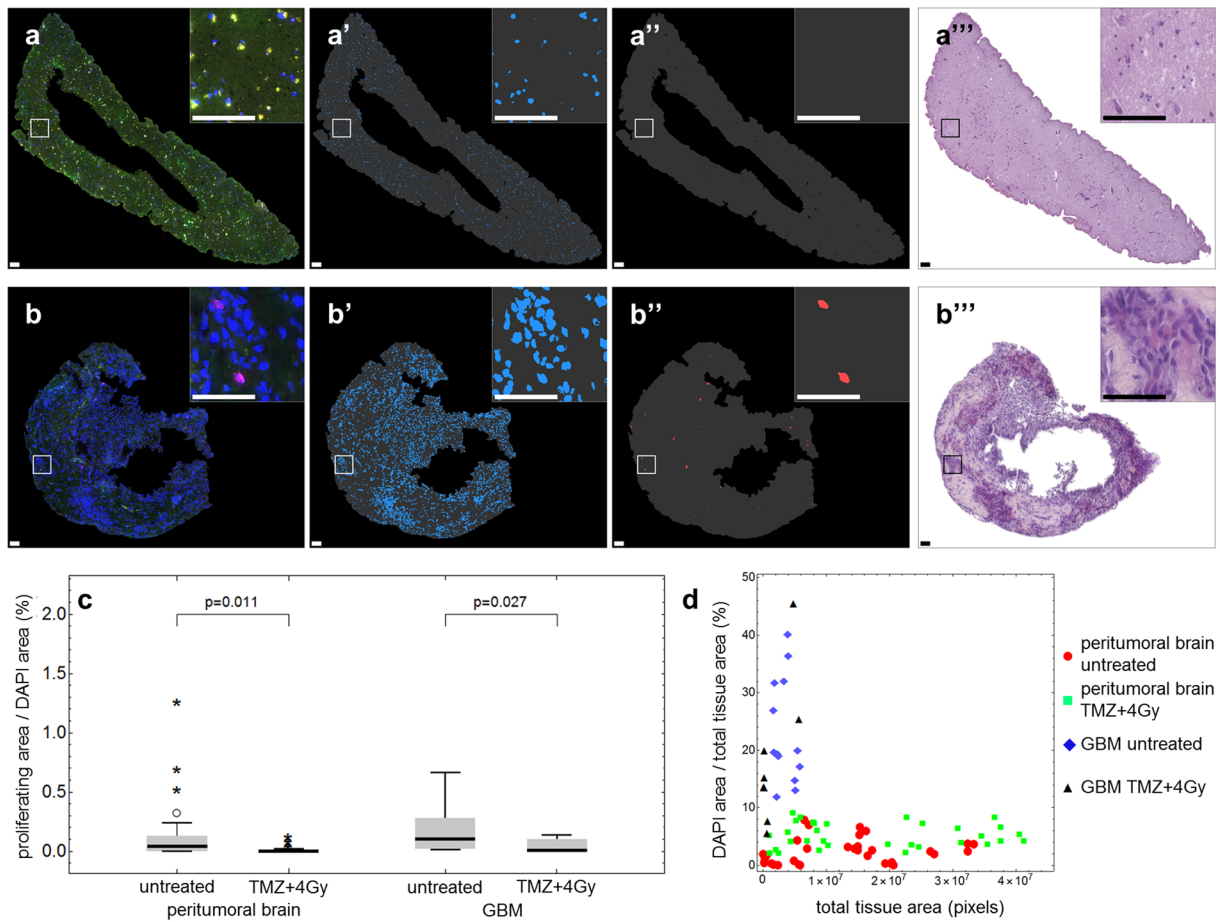


Figure 6. Histological finding of reduced proliferation after treatment supports mRNA expression data. Paraffin-embedded treated and untreated peritumoral brain (**a**) and GBM tissue (**b**) was stained with a Ki67 antibody as proliferation marker (red) and DAPI as nuclei marker (blue) and recorded by a slide scanner. Representative images of untreated samples are presented. (Note: green signals are attributed to autofluorescence of the tissue). For quantification, the total tissue area (**a''**, **b''**, gray), the nuclei area (**a'**, **b'**) and the Ki67-positive nuclei area (**a''', b''', red) were determined. H/E stainings of consecutive tissue sections are shown in **a'''** and **b'''**. (**c**) Ratio of proliferating area (Ki67- and DAPI-positive pixel area) per DAPI area in untreated and treated (TMZ + 4 Gy) peritumoral brain (left) and GBM tissue (right). (**d**) Ratio of DAPI area per total tissue area compared to total tissue area in pixels in untreated and treated (TMZ + 4 Gy) peritumoral brain (red circles, green squares) and GBM tissue (blue diamonds, black triangles). Biological replicates: 1; Technical replicates: 3; Scanned sections: 33 (untreated peritumoral brain), 32 (treated peritumoral brain), 13 (untreated GBM), 8 (treated GBM). Scale bars: 100 µm (**a**), 50 µm (**b**).**

pathway representing an alteration in the angiogenic pattern within the tumor⁴⁷. *FGF1* and other members of the FGF family are involved in cell proliferation, differentiation, and migration⁴⁸. Therefore, down-regulation of these family members is in agreement with the histologically observed decrease of proliferation. At this point, it is also interesting to note that FGF1/FGFR signaling activates Aurora A, a kinase which is involved in the maintenance of the stem cell characteristics of GBM cells⁴⁹. We further found down-regulation of *PDGFRα* and *c-KIT* which is especially interesting as these receptor tyrosine kinases have long been suggested as GBM therapeutic targets^{50,51}. In conclusion, the treatment-induced changes in mRNA expression are in agreement with the histological analysis which demonstrated inhibition of proliferation, as determined by a statistically significant decrease in the Ki67-positive pixel area under treatment (Fig. 6c).

The confirmation of the automatic analysis procedure was done by manual segmentation by three independent observers and both approaches were correlated with each other. A certain divergence of values among the three observers was noticed. While the results for total tissue area were very consistent, there was a notable spread in results for DAPI area which could be attributed to blooming around the stained nuclei. These minimal blooming artifacts appear during image acquisition and have no impact on the automatic analysis. Nevertheless, they proved to be interfering for observers during manual analysis. The large spread for the proliferating area was mainly caused by low signal intensities, poor image contrast and faintly remaining background fluorescence. These factors generally impede manual analysis and observers tend to underestimate threshold values. Overall, there was a very good correlation between manually and automatically obtained results for the total tissue area,

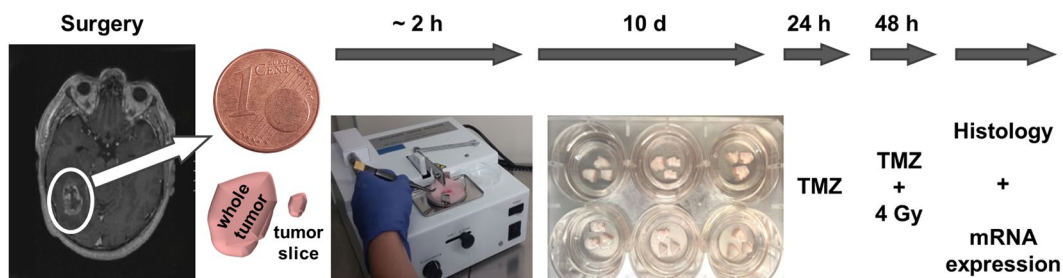


Figure 7. Experimental setup. Freshly resected glioblastoma (zone I) and peritumoral brain tissue (zone III) was transported into the lab in sterile transport medium and stored at 4°C. The production of 350 µm tissue slices was performed with a tissue chopper. The slices were separated from each other by the wide opening of a glass pipette and randomly allocated to membrane inserts and put in the wells of sterile 6-well plates, previously filled with 1 ml of cultivation medium. The slices were cultivated 10 days before treatment with radiochemotherapy was implemented. 24 hours prior to irradiation with 4 Gy the slices were pretreated with 200 µM temozolomide (TMZ). After a total treatment time of 72 hours the slices were either fixed in 4% paraformaldehyde for histological analyses or processed for RNA and protein isolation to perform whole transcriptome sequencing and protein analyses. We acknowledge Dr. Sonja Kallendrusch (Institute of Anatomy, University of Leipzig, Faculty of Medicine, Germany) who kindly provided the photograph of the tissue chopper.

which could be easily segmented by the three observers. The comparison of manual and automatic analysis of the DAPI area also showed very good correlation, although a manual under-segmentation was noted. The corresponding comparison of the proliferation area determination exhibited a moderate correlation and results indicated a manual over-segmentation. Values from individual images showed notable dispersion between automatic and manual analysis.

In conclusion, our data, in compliance with former studies^{4–7} demonstrate that organotypic slice cultures provide a suitable model for mimicking the *in vivo* situation within the patient thereby allowing insights into tumor biology that would not be possible by the use of conventional cell culture or animal models. By this means, it helps to reduce the numbers of animals used in cancer research. Furthermore, it may promote the way to individualized cancer medicine which is the current goal for therapeutic approaches. In the future and with the simultaneous development of new drugs it could be conceivable to prepare slice cultures for each patient, test possible chemotherapeutics and assist the physicians concerning the individual treatment strategy^{2,36,52}.

Material and Methods

Patient and samples. Glioblastoma tissue was obtained by surgery of a 51 year old male patient diagnosed with primary glioblastoma (GBM, WHO grade IV). Surgery and diagnosis were performed at the Department of Neurosurgery and the Department of Neuropathology, University Hospital Leipzig, Germany, according to the EANO guideline for the diagnosis and treatment of anaplastic gliomas and glioblastoma⁵³. To get surgical access to the MRI contrast-enhanced tumor tissue (= zone I), also tumor-surrounding brain tissue had to be removed. In the following, we refer to the tumor-surrounding tissue as peritumoral tissue (= zone III), which is basically normal brain tissue with only very few tumor cells⁵⁴. Both tissue types were subjected to organotypic tissue slice cultures in duplicates. Tissue acquisition and experimental procedure were approved by the institutional research ethics board (Ethical Review Committee of the Medical Faculty of the University of Leipzig, #144-2008; registration numbers: IORG0001320, IRB00001750) in accordance with the Helsinki Declaration (<https://www.wma.net/policies-post/wma-declaration-of-helsinki-ethical-principles-for-medical-research-involving-human-subjects/>). The patient provided written informed consent for experimental usage of his tissue samples and retrospective analysis of the data according to the General Data Protection Regulation of the European Community (<https://gdpr-info.eu/>).

Tissue slice preparation. Tissue slices that can be maintained in culture for at least 14 days were prepared using a previously described protocol⁵. In brief, surgically removed tissue not required for neuropathological diagnostic was transferred to Dulbecco's Modified Eagle Medium (DMEM, Gibco) supplemented with glucose (4.5 g/l, Gibco), fetal calf serum (10%, Biochrom), Glutamax (1%, Gibco) and penicillin/streptomycin (1%, Gibco). Organotypic tissue slices were prepared using a tissue chopper (McIlwain TC752) under sterile conditions (Fig. 7). Before preparation, a razor blade was sterilized by autoclaving. A normal glass pipette as well as a glass pipette with the fine tip broken off and appropriate forceps were autoclaved. The tissue was washed twice with fresh Minimum Essential Medium (MEM, Gibco) and was put on a stack of sterile filter membranes, cut into ~ 350 µm thick slices and transferred into ice-cold MEM. The slices were separated from each other by pipetting up and down with the wide opening of the broken-off glass pipette. Using this pipette they were randomly transferred onto membrane culture inserts (Millipore) in triplicates. The inserts were put into six-well plates equipped with 1 ml medium per well. The culture medium was composed of MEM, 25% Hank's Balanced Salt Solution (with Ca²⁺ and Mg²⁺, ThermoFisher Scientific), 10% heat-inactivated horse serum (Gibco), 1% L-glutamine (Gibco), 1% glucose (Mediatech Inc.) and 1% penicillin/streptomycin (Gibco). The slices were cultivated on a

liquid/air interface in a humidified incubator at 37 °C and 5% CO₂ for 13 days in total. During cultivation, slices were provided with fresh medium every 2 to 3 days.

Treatment of tissue slices. After 10 days in culture, slices were treated with temozolomide (TMZ, 200 μM). Control slices were incubated with the corresponding amount of dimethyl sulfoxide (DMSO, 0.2% v/v) used as vehicle. 24 hours after initial treatment, slices were X-irradiated (4 Gy) or sham-irradiated (control slices), and provided with fresh TMZ- or DMSO-supplemented medium the other day. For X-irradiation, a 200 kV irradiation machine (Gulmay Medical D3000, Gulmay, Surrey, UK) with a copper filter was used. The dose rate was 1.156 Gy/minute and each sample was irradiated 3.46 minutes to reach the target dose of 4 Gy. After a total treatment time of 72 hours, slices were processed for further analyses (Fig. 7).

Histology. Slices were fixed in 4% paraformaldehyde at 4 °C overnight and washed with phosphate-buffered saline (PBS). Slices were dehydrated and embedded in paraffin. Paraffin sections (7 μm) were cut with a sledge microtome and collected on glass slides (3 sections per slide). Hematoxylin and eosin staining was performed to evaluate the tissue maintenance. Photographs were taken with a digital slide scanner (Pannoramic Scan II, 3D HISTECH Ltd., Budapest, Hungary).

For immunological staining, every third slide per condition was dewaxed in xylene and rehydrated in decreasing concentrations of ethanol. Before immunostaining, the slides were pretreated two times for 20 minutes with citrate buffer (pH 6) in a microwave. Slides were washed with PBS and permeabilized/blocked with 0.3% Triton/PBS and 10% normal goat serum for 30 minutes. The primary antibody against Ki67 (MIB1 clone, mouse, 1:100, Dako, code number: M7240) was diluted in 0.3% Triton/PBS with 1% normal goat serum and incubated overnight at 4 °C. The Alexa 568-labeled secondary antibody (goat anti-mouse, 1:800, Gibco, catalog number: A-11004) was diluted in PBS and slides were incubated for 1 hour at room temperature. To stain the nuclei, slides were incubated with DAPI (ThermoFisher Scientific) for 15 minutes at room temperature. Slides were thoroughly washed with PBS and aqua dest. and covered with Fluorescence Mounting Medium (Dako) and coverslips. For apoptosis detection, five to six slides per condition were dewaxed as described above. A TUNEL assay was performed according to the manufacturer's protocol (Click-iT™ Plus TUNEL Assay, Alexa Fluor™ 594, Invitrogen™, order number C10618). To stain the nuclei, slides were incubated with DAPI, washed, and covered with coverslips as described above.

Imaging and image analysis. The immunofluorescently stained microscope slides were fully digitized at 20x magnification using a digital slide scanner (Pannoramic Scan II, 3D HISTECH Ltd., Budapest, Hungary) equipped with a quad band (DAPI/FITC/TRITC/Cy5) filter set. DAPI filter was used for blue DAPI channel, FITC filter was used for green tissue autofluorescence channel, and TRITC filter was used for Ki67 channel. Images of the stained tissue slices were exported from slide scanner data sets (Pannoramic Viewer, Version 1.15.4, 3D HISTECH Ltd., Budapest, Hungary) as PNG images with pixel dimensions of 0.325 μm. Some regions in the exported images had to be masked by hand (Adobe Photoshop CS6, Adobe Systems Inc., San Jose, USA) in order to remove artifacts (i.e. tissue overlaps, air bubbles, unspecific staining, dirt/fluorescent particles, blooming, etc.). Spectral bleedthrough between different color channels was corrected using the “Spectral Unmixing” plugin for ImageJ (Version 1.51n, <http://imagej.nih.gov/ij>). Image analysis was performed with Mathematica (Version 11.1, Wolfram Research, Inc., Champaign, IL, USA). Corrected fluorescence images were imported and split into separate color channels. In order to obtain tissue masks (almost entirely represented by DAPI and autofluorescence signals), all images were smoothed with a 5 pixel wide Gaussian filter and binarized using Otsu's (cluster variance maximization) thresholding method⁵⁵ prior to color channel separation. DAPI signals within blue image channels were also binarized using Otsu's thresholding method while proliferation marker (Ki67) signals within red image channels were binarized using Kapur's (histogram entropy minimization) thresholding method⁵⁶. Since specific proliferation marker staining can only occur within the nuclei, the binarized DAPI and Ki67 images were multiplied in order to omit unspecific staining outside of nuclei. The resulting masks were further cleared of very small segments (up to 20 pixels) to eliminate specks of fluorescent particles within nuclei. Finally, the areas of total tissue, DAPI and Ki67 masks were determined and ratios were computed. Numbers of analyzed images were as follows: 33 for untreated peritumoral brain tissue, 32 for peritumoral brain treated with TMZ + 4 Gy, 13 for untreated GBM tissue, 8 for GBM tissue treated with TMZ + 4 Gy.

To verify the result of the automated image analysis approach we performed an additional interactive analysis by three independent observers using ImageJ. Corrected fluorescence images were imported and split into separate color channels (DAPI, Ki67, autofluorescence). Subsequently, all color channels were segmented by interactive thresholding. Manually generated masks were imported in Mathematica and analyzed corresponding to the automatically segmented masks. Calculated parameters of the three observers' segmentations were averaged and ratios were computed.

Tissue slices with apoptosis staining underwent the same imaging and image preprocessing procedures as the microscope slides stained against Ki67, as mentioned above. Apoptosis was captured using the TRITC filter of the digital slide scanner. Spectral unmixing was performed and apoptosis signals within red image channels were binarized using Kapur's (histogram entropy minimization) thresholding method. Binarized DAPI and apoptosis images were multiplied in order to omit unspecific staining outside of nuclei. Subsequently, segmented images were inspected and masked by hand if necessary (e.g. vessels, artifacts). Finally, the areas of total tissue, DAPI, and apoptosis masks were determined, ratios were computed, and results were averaged for all slices originating from the same tissue slice.

RNA sequencing. Total RNA from cultivated tissue slices was isolated using the miRNeasy mini Kit (Qiagen) following the provided manufacturer's protocol. RNA yield was measured with the Qubit 2.0 instrument (Life Technologies) using the RNA Broad Range Assay. Total RNA amount per sample ranged from 1.5 to 2.9 µg. RNA quality was determined by the Bioanalyzer 2100 using the RNA 6000 Nano-Kit (Agilent Technologies). All samples had RNA integrity numbers of ≥ 7.6 (Table 1, before DNase digestion). RNA was DNase-digested twice using the TURBO DNA free Kit (Ambion®, ThermoFisher Scientific).

For library preparation with the Truseq-Stranded Total RNA Sample Prep Kit (Illumina) up to 200 ng RNA per sample were used. A ribosomal RNA (rRNA) depletion step using the Ribo-Zero Gold rRNA Removal Kit (Illumina) was conducted according to the manufacturer's protocol and – depending on the quality of each sample – a fragmentation was done. Every library was equipped with two barcodes to allow multiplexing of the samples. Concentrations were determined using the Qubit DNA Kit and the DNA quality was detected by the Bioanalyzer 2100 (DNA1000 Kit). According to the average size, which is determined by the Bioanalyzer, and the exact concentration of the samples, the molarity of each library was calculated.

The samples were sequenced at the HiSeq2500 with 2×126 bp paired-end reads. 12 pM of DNA were put on the flowcell using one lane per sample. The number of reads obtained was between 243 and 368×10^6 reads per sample, except for one sample (“peritumoral brain TMZ + 4 Gy 2”) with less than 50,000 reads.

Data analysis and statistics. *Primary and secondary data analysis.* Postprocessing of obtained raw reads per sample included demultiplexing using Illumina bcl2fastq v1.84 and secondary data analysis covering adaptor trimming, read mapping and expression quantification. Data processing of the secondary data analysis was invoked and monitored by the universal analysis pipeline (<http://uap.readthedocs.io/en/master/>), ensuring consistent and reproducible execution of each single analysis step per sample. The according configuration files are available as Supplementary File S1. In detail, adaptor sequences (adaptor 1: AGATCGGAAGAGCACACGTCT, adaptor 2: AGATCGGAAGAGCGTCGTGTA) were removed from raw reads by utilizing AdaptorRemoval v.2.2.0⁵⁷ with additional parameters –trimns –trimqualities –minquality 20, and –minlength 20 in order to trim terminating ambiguous bases or bases with a quality score less than 20 and to discard reads shorter than 20 bases. Trimmed reads were mapped to the human reference genome version GRCh38/hg38 by segemehl v0.2.0⁵⁸ in split read mode (option –splits) and with additional parameters –hitstrategy 1 and –differences 1 to report the best alignment with at maximum one indel or mutation in the initial seed and passing the default minimal alignment accuracy. Expression quantification for the human reference gene annotation Gencode v25⁵⁹ was obtained by using HTSeq v0.6.1⁶⁰ with parameters –stranded = reverse, –type = exon, –idattr = gene_id and –mode = intersection-strict. The number of reads assigned to a gene is, thus, defined by the number of paired reads that completely map to the exons of this gene and that do not map to any other gene. For assessing expression variation among samples raw counts were variance-stabilized by using the R library DeSeq2 version 1.10.1⁶¹. For visualization of expression, data raw gene counts were transformed to transcripts per million (TPMs) in order to correct for different sequencing depths of RNA libraries and gene length.

Quality control of obtained deep sequencing data. In order to assess the overall quality of the RNA sequencing for each tissue specimen a subsample of 1 million raw paired-end reads was randomly chosen by fastq-sample v0.0.14 (http://hannonlab.cshl.edu/fastx_toolkit/) using default parameters (<https://github.com/dcjonas/fastq-tools>). Each sample was evaluated according to the following criteria using FastQC v0.11.5 (<https://www.bioinformatics.babraham.ac.uk/projects/fastqc/>), FastQ Screen v0.11.1a (https://www.bioinformatics.babraham.ac.uk/projects/fastq_screen/), and self-developed scripts (for details see Supplemental Methods): (i) minimal Illumina Phred Quality Score of 30 reflecting minimal base call accuracy of 99.9%, (ii) no adapter sequence remnants detected, (iii) a negligible number of reads mapped to reference genomes other than human, and (iv) more than 90% of reads mapped to the human reference genome GRCh38/hg38 (Fig. S1). A manually assorted list of human rRNA sequences (see S1 Table for NCBI RefSeq identifiers) was used to calculate the fraction of reads mapping to human rRNA transcripts, resulting in fractions ranging from 17% to 66% (Fig. S2).

All samples except one (“peritumoral brain TMZ + 4 Gy 2”) passed all quality criteria (Figs. S1 and S2). For the remaining samples, a high fraction of reads mapping to rRNA transcripts was observed. However, reads corresponding to endogenous rRNA resulted in a maintainable number of reads. The fraction of high reads mapping antisense to rRNA genes resembled rRNA antisense probes from the rRNA depletion step, and thus do not affect assessment of transcriptome variation (Fig. S2).

Differential expression analysis. Differential expression was assessed with negative binomial models by using the R library DESeq2 version 1.10.1⁶¹ and RStudio version 1.1.442⁶². Both Samples of the treated peritumoral brain tissue (“peritumoral brain TMZ + 4 Gy”) were excluded from differential expression analysis because minimal number of required sample size was not reached due to sequencing failure of one sample of this group. The linear term for the negative binomial model to obtain significant changes in gene expression between two selected contrasts of interest (untreated peritumoral brain vs. untreated GBM tissue, untreated GBM vs. treated GBM tissue) is:

$$\log \lambda_{gi} = \beta_0 + \beta_1 \cdot group_k$$

with λ_{gi} denoting the relative abundance of gene g in sample i . The group parameter $group_k$ reflects a vector specifying the contrasts used for expression variation assessment. It assigns samples to the groups “untreated peritumoral brain” and “untreated GBM tissue” or to the groups “treated GBM” and “untreated GBM”, respectively. For both contrasts, expression variation was assessed for all genes with at least one read count in all regarded samples.

Default settings of independent filtering of the DeSeq2 R library were used. All genes with a false discovery rate (FDR) < 0.01⁶³ were classified to be significantly differentially expressed.

Ingenuity® pathway analysis (IPA®). The pathway enrichment analysis was done with the Ingenuity® Pathway Analysis software tool version 44961306 (IPA®, Qiagen). A table containing all the significant differentially expressed transcripts of the protein-coding fraction between treated and untreated GBM samples (2527 transcripts) and between untreated GBM versus peritumoral brain samples (3280 transcripts) was uploaded. A core analysis was run with default parameters based on expression log ratio. To link the histological data to the expression analysis data, a list of genes which are well-known to be associated with the proliferation of cancer and/or neuronal cells, was generated by IPA®. This IPA® list (1678 genes) was compared to the list of significant differentially expressed protein-coding genes between treated and untreated GBM tissue and the number of transcripts present in both lists was calculated. Of the 190 genes which were found in both lists, 7 of the most prominent ones were chosen for further analyses. They were extracted from the list of differentially expressed genes (DEGs) between treated and untreated GBM tissue, another core analysis was run with default parameters and the z-score was calculated. The z-score indicates whether an associated disease, function or pathway is predicted to be inhibited or activated under the given expression values⁶⁴. Figure 5 shows the results of this analysis. Green gene symbols in the figure illustrate the measured downregulation of the gene and blue arrows indicate the inhibition of the corresponding biological function, representing negative z-scores calculated by IPA®.

Statistical analysis of image quantification data. Statistical analysis was performed with IBM SPSS Statistics (version 22; IBM Corp.; Armonk, New York, USA). Data were tested for normal distribution using the Shapiro-Wilk test. Group comparisons were performed using Kruskal-Wallis test with Dunn's post hoc tests to adjust the p-value for multiple comparisons. Correlation analysis of manually and automatically calculated values was performed by computing Spearman's rank correlation coefficient. Significance for all tests was set at $p < 0.05$. Data were expressed as median and interquartile range, boxplots and scatterplots were generated using Mathematica.

Data availability

The deep sequencing datasets generated and analyzed during the current study are available in the GEO repository GSE119102. The histological datasets generated during the study are available from the corresponding author on reasonable request.

Received: 30 May 2019; Accepted: 12 December 2019;

Published online: 27 December 2019

References

1. Torre, L. A. *et al.* Global cancer statistics, 2012. *CA: a cancer journal for clinicians* **65**, 87–108, <https://doi.org/10.3322/caac.21262> (2015).
2. Hafner, K. & Mayer, B. Bringing 3D tumor models to the clinic - predictive value for personalized medicine. *Biotechnology journal*, **12**, <https://doi.org/10.1002/biot.201600295> (2017).
3. Nitsch, R. *et al.* Human brain-cell death induced by tumour-necrosis-factor-related apoptosis-inducing ligand (TRAIL). *Lancet* **356**, 827–828, [https://doi.org/10.1016/S0140-6736\(00\)02659-3](https://doi.org/10.1016/S0140-6736(00)02659-3) (2000).
4. Kallendrusch, S., Merz, F., Bechmann, I., Mayr, S. G. & Zink, M. Long-Term Tissue Culture of Adult Brain and Spleen Slices on Nanostructured Scaffolds. *Advanced healthcare materials*, **6**, <https://doi.org/10.1002/adhm.201601336> (2017).
5. Merz, F. *et al.* Organotypic slice cultures of human glioblastoma reveal different susceptibilities to treatments. *Neuro Oncol* **15**, 670–681, <https://doi.org/10.1093/neuonc/not003> (2013).
6. Gerlach, M. M. *et al.* Slice cultures from head and neck squamous cell carcinoma: a novel test system for drug susceptibility and mechanisms of resistance. *Br J Cancer* **110**, 479–488, <https://doi.org/10.1038/bjc.2013.700> (2014).
7. Koerfer, J. *et al.* Organotypic slice cultures of human gastric and esophagogastric junction cancer. *Cancer Med* **5**, 1444–1453, <https://doi.org/10.1002/cam4.720> (2016).
8. Sönnichsen, R. *et al.* Individual Susceptibility Analysis Using Patient-derived Slice Cultures of Colorectal Carcinoma. *Clinical colorectal cancer*, <https://doi.org/10.1016/j.clcc.2017.11.002> (2017).
9. Ewe, A. *et al.* Optimized polyethylenimine (PEI)-based nanoparticles for siRNA delivery, analyzed *in vitro* and in an *ex vivo* tumor tissue slice culture model. *Drug delivery and translational research* **7**, 206–216, <https://doi.org/10.1007/s13346-016-0306-y> (2017).
10. Louis, D. N. *et al.* The 2016 World Health Organization Classification of Tumors of the Central Nervous System: a summary. *Acta Neuropathol* **131**, 803–820, <https://doi.org/10.1007/s00401-016-1545-1> (2016).
11. Stupp, R. *et al.* Radiotherapy plus Concomitant and Adjuvant Temozolomide for Glioblastoma. *N Engl J Med* **352**, 987–996 (2005).
12. Stupp, R. *et al.* Effects of radiotherapy with concomitant and adjuvant temozolomide versus radiotherapy alone on survival in glioblastoma in a randomised phase III study: 5-year analysis of the EORTC-NCIC trial. *Lancet Oncol* **10**, 459–466 (2009).
13. Schroeder, A. *et al.* The RIN. An RNA integrity number for assigning integrity values to RNA measurements. *BMC molecular biology*, **7**, <https://doi.org/10.1186/1471-2199-7-3> (2006).
14. Eikrem, O. *et al.* Transcriptome Sequencing (RNAseq) Enables Utilization of Formalin-Fixed, Paraffin-Embedded Biopsies with Clear Cell Renal Cell Carcinoma for Exploration of Disease Biology and Biomarker Development. *PloS one*, **11**, <https://doi.org/10.1371/journal.pone.0149743> (2016).
15. Zhao, W. *et al.* Comparison of RNA-Seq by poly (A) capture, ribosomal RNA depletion, and DNA microarray for expression profiling. *BMC genomics* **15**, 419, <https://doi.org/10.1186/1471-2164-15-419> (2014).
16. Yan, J. *et al.* Association between microRNA-125b expression in formalin-fixed paraffin-embedded tumor tissues and prognosis in patients with melanoma. *Oncol Lett* **18**, 1856–1862, <https://doi.org/10.3892/ol.2019.10506> (2019).
17. Bonavia, R., Inda, M.-d.M., Cavenee, W. K. & Furnari, F. B. Heterogeneity maintenance in glioblastoma. A social network. *Cancer research* **71**, 4055–4060, <https://doi.org/10.1158/0008-5472.CAN-11-0153> (2011).
18. Gerdes, J. *et al.* Cell cycle analysis of a cell proliferation-associated human nuclear antigen defined by the monoclonal antibody Ki-67. *J Immunol* **133**, 1710–1715 (1984).
19. Paz-Ares, L. G. *et al.* PARAMOUNT. Final overall survival results of the phase III study of maintenance pemetrexed versus placebo immediately after induction treatment with pemetrexed plus cisplatin for advanced nonsquamous non-small-cell lung cancer.

- Journal of clinical oncology: official journal of the American Society of Clinical Oncology* **31**, 2895–2902, <https://doi.org/10.1200/JCO.2012.47.1102> (2013).
20. Digklia, A. & Wagner, A. D. Advanced gastric cancer. Current treatment landscape and future perspectives. *World journal of gastroenterology* **22**, 2403–2414, <https://doi.org/10.3748/wjg.v22.i8.2403> (2016).
 21. Wesseling, P., van der Laak, J. A. W. M., de Leeuw, H., Ruiter, D. J. & Burger, P. C. Quantitative immunohistological analysis of the microvasculature in untreated human glioblastoma multiforme. *Computer-assisted image analysis of whole-tumor sections. J Neurosurg* **81**, 902–909 (1994).
 22. Cheng, L. *et al.* Glioblastoma stem cells generate vascular pericytes to support vessel function and tumor growth. *Cell* **153**, 139–152, <https://doi.org/10.1016/j.cell.2013.02.021> (2013).
 23. Whiteside, T. L. The tumor microenvironment and its role in promoting tumor growth. *Oncogene* **27**, 5904–5912, <https://doi.org/10.1038/onc.2008.271> (2008).
 24. Singh, S. K. *et al.* Identification of human brain tumour initiating cells. *Nature* **432**, 396–400, <https://doi.org/10.1038/nature03031> (2004).
 25. Jin, K. *et al.* Patient-derived human tumour tissue xenografts in immunodeficient mice. A systematic review. *Clinical & translational oncology: official publication of the Federation of Spanish Oncology Societies and of the National Cancer Institute of Mexico* **12**, 473–480, <https://doi.org/10.1007/s12094-010-0540-6> (2010).
 26. Whittle, J. R., Lewis, M. T., Lindeman, G. J. & Visvader, J. E. Patient-derived xenograft models of breast cancer and their predictive power. *Breast cancer research: BCR*, **17**, <https://doi.org/10.1186/s13058-015-0523-1> (2015).
 27. Zhang, X.-c. *et al.* Establishment of patient-derived non-small cell lung cancer xenograft models with genetic aberrations within EGFR, KRAS and FGFR1. Useful tools for preclinical studies of targeted therapies. *Journal of translational medicine*, **11**, <https://doi.org/10.1186/1479-5876-11-168> (2013).
 28. Kageyama, K. *et al.* Establishment of an orthotopic patient-derived xenograft mouse model using uveal melanoma hepatic metastasis. *Journal of translational medicine* **15**, 145, <https://doi.org/10.1186/s12967-017-1247-z> (2017).
 29. Flanagan, S. P. Nudé, a new hairless gene with pleiotropic effects in the mouse. *Genetical research* **8**, 295–309 (1966).
 30. Bosma, G. C., Custer, R. P. & Bosma, M. J. A severe combined immunodeficiency mutation in the mouse. *Nature* **301**, 527–530 (1983).
 31. Davies, E. J. *et al.* Capturing complex tumour biology *in vitro*. Histological and molecular characterisation of precision cut slices. *Scientific reports* **5**, 17187, <https://doi.org/10.1038/srep17187> (2015).
 32. Göttlich, C. *et al.* A Combined 3D Tissue Engineered *In Vitro*/In Silico Lung Tumor Model for Predicting Drug Effectiveness in Specific Mutational Backgrounds. *Journal of visualized experiments: JoVE*, e53885, <https://doi.org/10.3791/53885> (2016).
 33. Jonas, O. *et al.* An implantable microdevice to perform high-throughput *in vivo* drug sensitivity testing in tumors. *Science translational medicine* **7**, 284ra57, <https://doi.org/10.1126/scitranslmed.3010564> (2015).
 34. Klinghammer, K., Walther, W. & Hoffmann, J. Choosing wisely – Preclinical test models in the era of precision medicine. *Cancer treatment reviews* **55**, 36–45, <https://doi.org/10.1016/j.ctrv.2017.02.009> (2017).
 35. Klinghofer, R. A. *et al.* A technology platform to assess multiple cancer agents simultaneously within a patient's tumor (2015).
 36. Naipal, K. A. T. *et al.* Tumor slice culture system to assess drug response of primary breast cancer. *BMC cancer*, **16**, <https://doi.org/10.1186/s12885-016-2119-2> (2016).
 37. Uhl, F. E. *et al.* Preclinical validation and imaging of Wnt-induced repair in human 3D lung tissue cultures. *The European respiratory journal* **46**, 1150–1166, <https://doi.org/10.1183/09031936.00183214> (2015).
 38. Markovic, D. S., Glass, R., Synowitz, M., van Rooijen, N. & Kettenmann, H. Microglia Stimulate the Invasiveness of Glioma Cells by Increasing the Activity of Metalloprotease-2. *J Neuropathol Exp Neurol* **64**, 754–762, <https://doi.org/10.1097/01.jnen.0000178445.33972.a9> (2005).
 39. Markovic, D. S. *et al.* Gliomas induce and exploit microglial MT1-MMP expression for tumor expansion. *Proceedings of the National Academy of Sciences of the United States of America* **106**, 12530–12535, <https://doi.org/10.1073/pnas.0804273106> (2009).
 40. Sliwa, M. *et al.* The invasion-promoting effect of microglia on glioblastoma cells is inhibited by cyclosporin A. *Brain* **130**, 476–489, <https://doi.org/10.1093/brain/awl263> (2007).
 41. Aum, D. J. *et al.* Molecular and cellular heterogeneity: the hallmark of glioblastoma (2014).
 42. Chen, J. *et al.* Identification of Secreted Phosphoprotein 1 (SPP1) as a Prognostic Factor in Lower-Grade Gliomas. *World Neurosurg* **130**, e775–e785, <https://doi.org/10.1016/j.wneu.2019.06.219> (2019).
 43. Yan, W. *et al.* Expression pattern of osteopontin splice variants and its functions on cell apoptosis and invasion in glioma cells. *Neuro Oncol* **12**, 765–775, <https://doi.org/10.1093/neuonc/noq006> (2010).
 44. Gao, C. *et al.* Osteopontin-dependent CD44v6 expression and cell adhesion in HepG2 cells. *Carcinogenesis* **24**, 1871–1878, <https://doi.org/10.1093/carcin/bgg139> (2003).
 45. Pietras, A. *et al.* Osteopontin-CD44 signaling in the glioma perivascular niche enhances cancer stem cell phenotypes and promotes aggressive tumor growth. *Cell stem cell* **14**, 357–369, <https://doi.org/10.1016/j.stem.2014.01.005> (2014).
 46. Brown, D. V. *et al.* Coexpression analysis of CD133 and CD44 identifies proneural and mesenchymal subtypes of glioblastoma multiforme. *Oncotarget* **6**, 6267–6280, <https://doi.org/10.18632/oncotarget.3365> (2015).
 47. Tabouret, E. *et al.* Recurrence of glioblastoma after radio-chemotherapy is associated with an angiogenic switch to the CXCL12-CXCR4 pathway. *Oncotarget* **6**, 11664–11675, <https://doi.org/10.18632/oncotarget.3256> (2015).
 48. Beenken, A. & Mohammadi, M. The FGF family: biology, pathophysiology and therapy. *Nature reviews. Drug discovery* **8**, 235–253, <https://doi.org/10.1038/nrd2792> (2009).
 49. Hsu, Y.-C. *et al.* Activation of Aurora A kinase through the FGF1/FGFR signaling axis sustains the stem cell characteristics of glioblastoma cells. *Exp Cell Res* **344**, 153–166, <https://doi.org/10.1016/j.yexcr.2016.04.012> (2016).
 50. Cantanhede, I. G. & Oliveira, J. R. Mde PDGF Family Expression in Glioblastoma Multiforme: Data Compilation from Ivy Glioblastoma Atlas Project Database. *Sci Rep* **7**, 15271, <https://doi.org/10.1038/s41598-017-15045-w> (2017).
 51. Pearson, J. R. D. & Regad, T. Targeting cellular pathways in glioblastoma multiforme. *Signal transduction and targeted therapy* **2**, 17040, <https://doi.org/10.1038/sigtrans.2017.40> (2017).
 52. Montero, J. *et al.* Drug-induced death signaling strategy rapidly predicts cancer response to chemotherapy. *Cell* **160**, 977–989, <https://doi.org/10.1016/j.cell.2015.01.042> (2015).
 53. Weller, M. *et al.* EANO guideline for the diagnosis and treatment of anaplastic gliomas and glioblastoma. *The Lancet Oncology* **15**, e395–e403, [https://doi.org/10.1016/S1470-2045\(14\)70011-7](https://doi.org/10.1016/S1470-2045(14)70011-7) (2014).
 54. Eyüpoglu, I. Y. *et al.* Supra-complete surgery via dual intraoperative visualization approach (DiVA) prolongs patient survival in glioblastoma. *Oncotarget* **7**, 25755–25768, <https://doi.org/10.18632/oncotarget.8367> (2016).
 55. Otsu, N. A Threshold Selection Method from Gray-Level Histograms. *IEEE Trans. Syst., Man, Cybern.* **9**, 62–66, <https://doi.org/10.1109/TSMC.1979.4310076> (1979).
 56. Kapur, J. N., Sahoo, P. K. & Wong, A. K. A new method for gray-level picture thresholding using the entropy of the histogram. *Computer Vision, Graphics, and Image Processing* **29**, 273–285, [https://doi.org/10.1016/0734-189X\(85\)90125-2](https://doi.org/10.1016/0734-189X(85)90125-2) (1985).
 57. Schubert, M., Lindgreen, S. & Orlando, L. AdapterRemoval v2: rapid adapter trimming, identification, and read merging. *BMC research notes*, **9**, <https://doi.org/10.1186/s13104-016-1900-2> (2016).
 58. Hoffmann, S. *et al.* A multi-split mapping algorithm for circular RNA, splicing, trans-splicing and fusion detection. *Genome biology* **15**, R34, <https://doi.org/10.1186/gb-2014-15-2-r34> (2014).

59. Harrow, J. *et al.* GENCODE: the reference human genome annotation for The ENCODE Project. *Genome research* **22**, 1760–1774, <https://doi.org/10.1101/gr.135350.111> (2012).
60. Anders, S., Pyl, P. T. & Huber, W. HTSeq—a Python framework to work with high-throughput sequencing data. *Bioinformatics (Oxford, England)* **31**, 166–169, <https://doi.org/10.1093/bioinformatics/btu638> (2015).
61. Love, M. I., Huber, W. & Anders, S. Moderated estimation of fold change and dispersion for RNA-seq data with DESeq2. *Genome biology*, **15**, <https://doi.org/10.1186/s13059-014-0550-8> (2014).
62. RStudio Team. *RStudio: Integrated Development Environment for R* (Boston, MA, 2015).
63. Benjamini, Y. & Hochberg, Y. Controlling the False Discovery Rate: A Practical and Powerful Approach to Multiple Testing. *J R Stat Soc Series B* **57**, 289–300 (1995).
64. Krämer, A., Green, J., Pollard, J. & Tugendreich, S. Causal analysis approaches in Ingenuity Pathway Analysis. *Bioinformatics (Oxford, England)* **30**, 523–530, <https://doi.org/10.1093/bioinformatics/btt703> (2014).

Acknowledgements

This study was supported by the Federal Ministry of Education and Research (BMBF, Alternatives to animal testing, Project number: 031A579). We gratefully acknowledge the technical help of Rainer Baran-Schmidt. We further thank Judith Leyh and Dr. Peter Wieghofer for critical reading of the manuscript. We thank Dr. Sonja Kallendrusch who kindly provided the photograph of the tissue chopper. We acknowledge support from the German Research Foundation (DFG) and Leipzig University within the program of Open Access Publishing.

Author contributions

I.B., F.G., F.R., F.H. and J.M. managed the funding and conceptualization of the project and provided resources. S.H., A.H., N.K. and D.L. conducted the experiments and collected data. S.H., K.W., K.R., M.R., S.-H.P. and C.B. analyzed study data. S.H., K.W., K.R. and D.L. wrote the initial manuscript. All authors reviewed the manuscript.

Competing interests

The authors declare no competing interests.

Additional information

Supplementary information is available for this paper at <https://doi.org/10.1038/s41598-019-56509-5>.

Correspondence and requests for materials should be addressed to S.H.

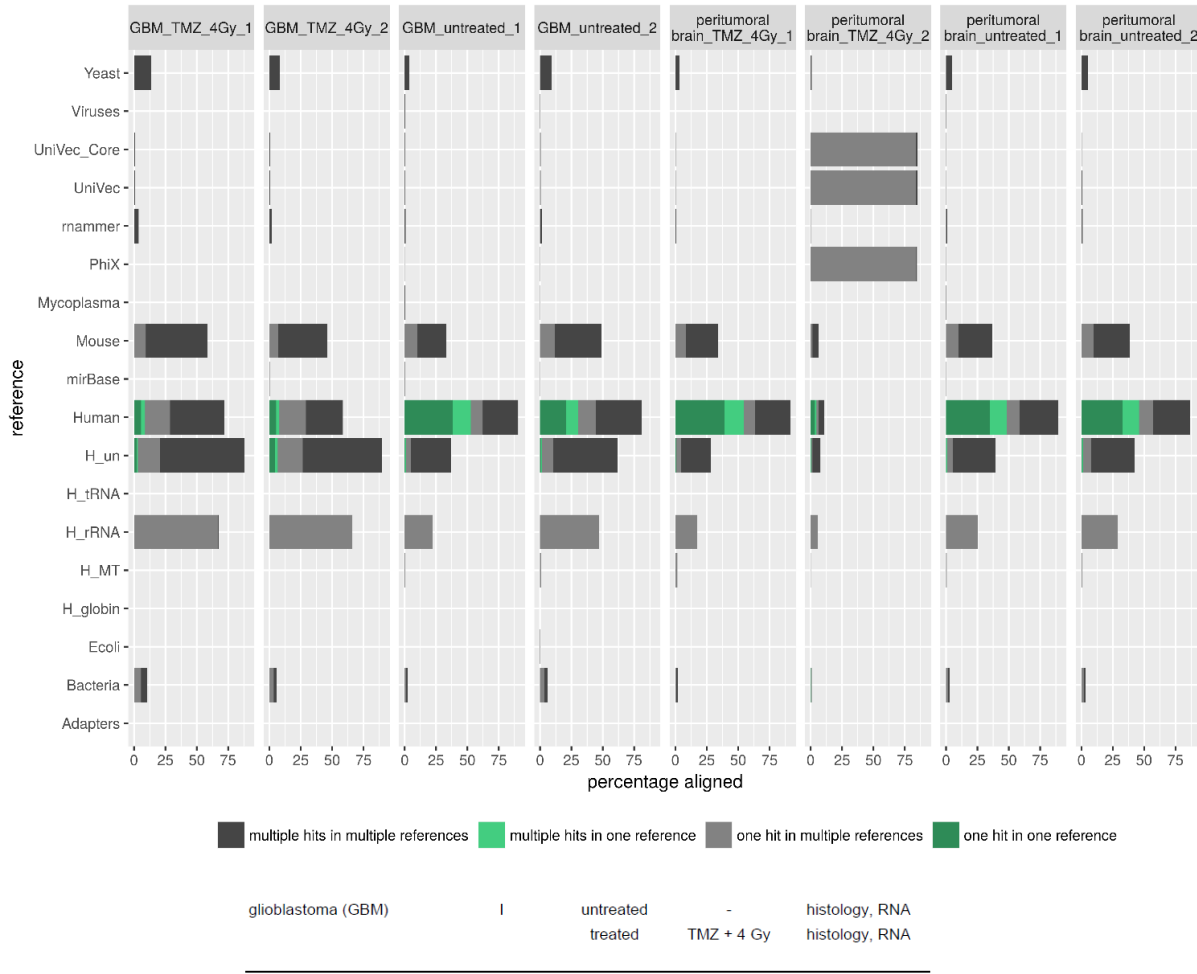
Reprints and permissions information is available at www.nature.com/reprints.

Publisher's note Springer Nature remains neutral with regard to jurisdictional claims in published maps and institutional affiliations.



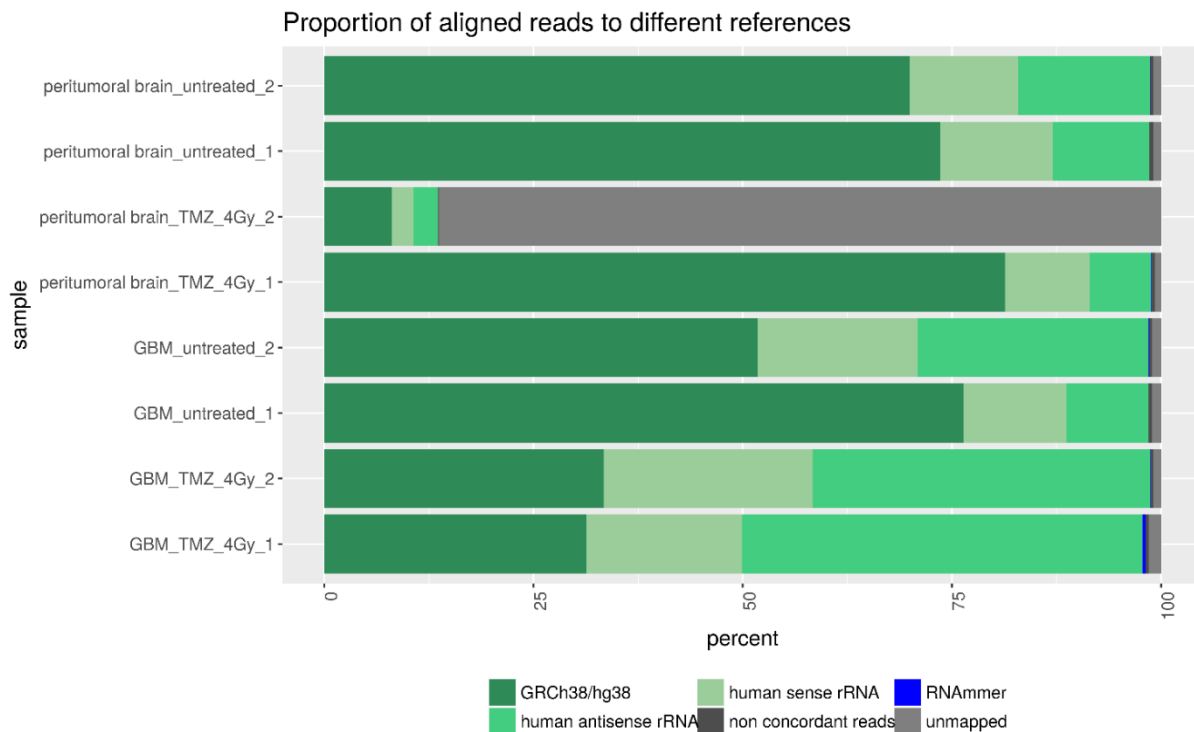
Open Access This article is licensed under a Creative Commons Attribution 4.0 International License, which permits use, sharing, adaptation, distribution and reproduction in any medium or format, as long as you give appropriate credit to the original author(s) and the source, provide a link to the Creative Commons license, and indicate if changes were made. The images or other third party material in this article are included in the article's Creative Commons license, unless indicated otherwise in a credit line to the material. If material is not included in the article's Creative Commons license and your intended use is not permitted by statutory regulation or exceeds the permitted use, you will need to obtain permission directly from the copyright holder. To view a copy of this license, visit <http://creativecommons.org/licenses/by/4.0/>.

© The Author(s) 2019



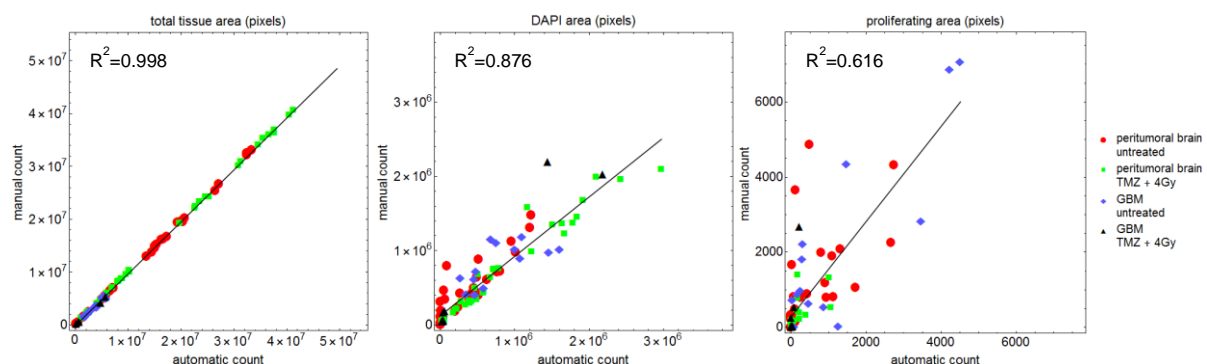
Suppl. Fig. S1: Quality Control of samples with respect to sequencing library composition.

FastQ Screen v0.11.1a was used to assess sequencing library composition in order to detect possible contamination like bacteria and overrepresented fractions of RNA species like human rRNA. Values are given in percentage of reads aligning to selected sequence references. Reads are classified into four distinct types indicating reads uniquely mapping in one sequence reference (one hit in one reference), reads with multiple mappings in one sequence reference (multiple hits in one reference), reads uniquely mapping in distinct sequence references (one hit in multiple references), and reads with multiple mappings in distinct sequence databases (multiple hits in multiple references). The queried sequences are the following: Yeast (genome assembly SacCer3), Viruses (ftp://ftp.ncbi.nlm.nih.gov/genomes/refseq/viral/, March 2014), UniVec and UniVec Core (vector sequences from ftp://ftp.ncbi.nlm.nih.gov/pub/UniVec/build 8.0, May 2015), rnammer (predicted rRNA sequences from http://www.cbs.dtu.dk/services/RNAmer/, v1.2), phiX (gi|9626q372|ref|NC_001422.1| Enterobacteri phage phiX174 sensu lato, complete genome), Mycoplasma (ftp://ftp.ncbi.nih.gov/genomes/refseq/bacteria/Mycoplasma_*, Oct 2014), Mouse (genome assembly mm10), mirBase (miRNA sequences from mirBase v21), Human (human assembly GRCh37/hg19, reference chromosomes only), H_un (unplaced contigs and patches of GRCh37/hg19), H_tRNA (human transfer RNA sequences, http://gttrnadb.ucsc.edu/genomes/eukaryota/Hsapi19/hg19-tRNAs.fa), H_rRNA (human ribosomal RNA sequences, see Supplemental Table S1), H_MT (human mitochondrial reference sequence in GRCh37/hg19), H_globin (human hemoglobin mRNA sequences retrieved from NCBI RefSeq database, see Supplemental Table S2), Ecoli (Escherichia coli K12 DH10B), Bacteria (ftp://ftp.ncbi.nih.gov/genomes/refseq/bacteria/, Oct 2014), and adapters (adapter sequences from https://github.com/csf-ngs/fastqc/blob/master/Contaminants/contaminant_list.txt). Please note that the sample peritumoral brain_TMZ_4GY_2 is a dropout sample, since sequencing depth was about 50K reads and hence accumulates reads from the Illumina spike-in phiX.



Suppl. Fig. 2: Quality Control of samples with respect to fraction of reads mapping to the human genome.

The fraction of reads mapping to the human genome was assessed iteratively by mapping reads against the RNAmer database v1.2 (bowtie2 v2.2.7), human rRNA (bowtie2 v2.2.7), and the human genome assembly GRCh38/hg38 (segemehl v.0.2.0). Non-concordant reads represent reads which do not map linear to the human genome, but for example circular. Human rRNA reads are divided into sense, which resembles endogenous rRNA, and antisense rRNA which resembles rRNA antisense probes from the rRNA depletion step.



Suppl. Fig. 3: Correlation plots of manual versus automatic histological analysis.

The correlation coefficient R^2 of manual versus automatic counts were calculated for total tissue area (left plot), DAPI area (middle plot), and proliferating area (Ki67 positive, right plot). Red circles and green squares represent untreated and treated (TMZ+4Gy) peritumoral brain, whereas blue diamonds and black triangles represent untreated and treated (TMZ+4Gy) GBM tissue.

Tab. S1: rRNA sequences (NCBI RefSeq).

18S_gi	124517659	ref	NR_003286.1	Homo sapiens 18S ribosomal RNA (LOC100008588)
28S_gi	124517661	ref	NR_003287.1	Homo sapiens 28S ribosomal RNA (LOC100008589)
5S_gi	36084	emb	V00589.1	Human 5S ribosomal RNA
5.8S_gi	142372596	ref	NR_003285.2	Homo sapiens RNA, 5.8S ribosomal 1 (RN5-8S1), ribosomal RNA
12S_gi	251831106:648-1601			Homo sapiens mitochondrion, complete genome
16S_gi	251831106:1671-3229			Homo sapiens mitochondrion, complete genome

Tab. S2: NCBI RefSeq accession IDs for globins.

>gi	672228742 ref	NM_000558.4	Homo sapiens hemoglobin, alpha 1 (HBA1), mRNA
>gi	172072689 ref	NM_000517.4	Homo sapiens hemoglobin, alpha 2 (HBA2), mRNA
>gi	94538363 ref	NM_001003938.3	Homo sapiens hemoglobin, mu (HBM), mRNA
>gi	28302132 ref	NM_000184.2	Homo sapiens hemoglobin, gamma G (HBG2), mRNA
>gi	28302130 ref	NM_000559.2	Homo sapiens hemoglobin, gamm A (HBG2), mRNA
>gi	28302128 ref	NM_000518.4	Homo sapiens hemoglobin, beta (HBB), mRNA
>gi	6633805 ref	NM_005332.2	Homo sapiens hemoglobin, zeta (HBZ), mRNA
>gi	62865863 ref	NM_000519.3	Homo sapiens hemoglobin, delta (HBD), mRNA
>gi	28302129 ref	NM_005330.3	Homo sapiens hemoglobin, epsilon 1 (HBE1), mRNA
>gi	44955887 ref	NM_203378.1	Homo sapiens myoglobin (MB), transcript variant 3, mRNA
>gi	44955884 ref	NM_203377.1	Homo sapiens myoglobin (MB), transcript variant 2, mRNA
>gi	44955876 ref	NM_005368.2	Homo sapiens myoglobin (MB), transcript variant 1, mRNA

Tab. S3: Summary of the samples.

Sample	Zone	Treatment	Data	
peritumoral brain	III	untreated	-	histology, RNA
		treated	TMZ + 4 Gy	histology
glioblastoma (GBM)	I	untreated	-	histology, RNA
		treated	TMZ + 4 Gy	histology, RNA

Publikation II

RNA sequencing of glioblastoma tissue slice cultures reveals the effects of treatment at the transcriptional level

Susann Haehnel¹, Michael Rade², Nicole Kaiser¹, Kristin Reiche², Andreas Horn¹, Dennis Loeffler², Conny Blumert², Felicitas Rapp³, Friedemann Horn^{2,4}, Juergen Meixensberger⁵, Christof Renner⁶, Wolf Mueller⁷, Frank Gaunitz⁵, Ingo Bechmann¹ and Karsten Winter¹

¹Institute of Anatomy, Faculty of Medicine, University of Leipzig, Germany

²Department of Diagnostics, Fraunhofer Institute of Cell Therapy and Immunology, Leipzig, Germany

³GSI Helmholtzzentrum für Schwerionenforschung GmbH, Darmstadt, Germany

⁴Institute of Clinical Immunology, Faculty of Medicine, University of Leipzig, Germany

⁵Department of Neurosurgery, University Hospital Leipzig, Germany

⁶Department of Neurosurgery, City Hospital, Dessau, Germany

⁷Department of Neuropathology, University Hospital Leipzig, Germany

RNA sequencing of glioblastoma tissue slice cultures reveals the effects of treatment at the transcriptional level

Susann Haehnel¹ , Michael Rade², Nicole Kaiser¹, Kristin Reiche², Andreas Horn¹, Dennis Loeffler², Conny Blumert², Felicitas Rapp³, Friedemann Horn^{2,4}, Juergen Meixensberger⁵, Christof Renner⁶, Wolf Mueller⁷, Frank Gaunitz⁵, Ingo Bechmann¹ and Karsten Winter¹

¹ Institute of Anatomy, Faculty of Medicine, University of Leipzig, Germany

² Department of Diagnostics, Fraunhofer Institute of Cell Therapy and Immunology, Leipzig, Germany

³ GSI Helmholtzzentrum für Schwerionenforschung GmbH, Darmstadt, Germany

⁴ Institute of Clinical Immunology, Faculty of Medicine, University of Leipzig, Germany

⁵ Department of Neurosurgery, University Hospital Leipzig, Germany

⁶ Department of Neurosurgery, City Hospital, Dessau, Germany

⁷ Department of Neuropathology, University Hospital Leipzig, Germany

Keywords

glioblastoma multiforme;
radiochemotherapy; RNA sequencing; tissue
slice cultures

Correspondence

S. Haehnel, University of Leipzig, Institute
of Anatomy, Liebigstrasse 13, 04103
Leipzig, Germany
Tel: +49 341 9722007
E-mail: su.haehnel@gmail.com

(Received 26 September 2021, revised 22
November 2021, accepted 16 December
2021)

doi:10.1002/2211-5463.13353

Edited by Ivana Novak

One of the major challenges in cancer research is finding models that closely resemble tumors within patients. Human tissue slice cultures are a promising approach to provide a model of the patient's tumor biology *ex vivo*. Recently, it was shown that these slices can be successfully analyzed by whole transcriptome sequencing as well as automated histochemistry, increasing their usability as preclinical model. Glioblastoma multiforme (GBM) is a highly malignant brain tumor with poor prognosis and little is known about its genetic background and heterogeneity regarding therapy success. In this study, tissue from the tumors of 25 patients with primary GBM was processed into slice cultures and treated with standard therapy (irradiation and temozolomide). Total RNA sequencing and automated histochemistry were performed to enable analysis of treatment effects at a transcriptional and histological level. Slice cultures from long-term survivors (overall survival [OS] > 24 months) exhibited more apoptosis than cultures from patients with shorter OS. Proliferation within these slices was slightly increased in contrast to other groups, but not significantly. Among all samples, 58 protein-coding genes were upregulated and 32 downregulated in treated vs. untreated slice cultures. In general, an upregulation of DNA damage-related and cell cycle checkpoint genes as well as enrichment of genotoxicity pathways and p53-dependent signaling was found after treatment. Overall, the current study reproduces knowledge from former studies regarding the feasibility of transcriptomic analyses and automated histology in tissue slice cultures. We further demonstrate that the experimental data merge with the clinical follow-up of the patients, which improves the applicability of our model system.

Glioblastoma multiforme (GBM) is the most frequent malignant brain tumor in adults [1]. As astrocytoma of grade IV, it is characterized by infiltrative growth, high

mitotic activity, microvascular proliferation, and necrosis [2,3]. Despite aggressive standard combination therapy of surgical resection, irradiation, and chemotherapy

Abbreviations

DEG, differentially expressed gene; GBM, glioblastoma multiforme; Gy, gray; HR, hazard ratio; Ifc, log2-fold-change; MGMT, O-6-Methylguanine-DNA-Methyltransferase; NK, natural killer cells; OS, overall survival; PFS, progression-free survival; TMZ, temozolomide.

with temozolomide (TMZ), the median overall survival (OS) of patients with primary GBM still is only about 15 months [4,5]. Primary GBM is defined as *de novo* development of the tumor without any evidence of a less malignant precursor tumor, whereas secondary GBMs evolve from the progression of lower grade astrocytomas [6]. Both classes differ significantly regarding their molecular evolution and genetic pathways [7], RNA expression patterns [8,9], and the patients' prognosis and therapy response [10]. In the present study, we focused on the analysis of primary GBM.

One of the major challenges in GBM therapy is its high intra- and intertumoral heterogeneity and the related difficulty of predicting a patients' response to therapy [11,12]. Many trials are aiming at the identification of predictive biomarkers, but the clinical relevance is often limited and the development of targeted drugs is still challenging [12–15], not least due to the impermeability of the blood–brain barrier [16,17]. Even the methylation status of the O-6-Methylguanine-DNA-Methyltransferase (MGMT) promotor, which is well-established and has been shown to be related to the therapy response and prognosis, leads to heterogeneous responses in patients [18]. In 2010, four molecularly defined subgroups of GBM were established—classical, mesenchymal, proneural, and neural subtype—including characteristic gene expression patterns [19]. Despite this increase in knowledge about genetic and transcriptomic features of GBM since the implementation of TMZ-based radiochemotherapy, the standard of care is not considerably influenced [20]. Further, even within each subtype, there still is a high intratumoral heterogeneity on the expression level [21] which underlines the strong need to develop an individualized approach for each single GBM patient.

Generally, cancer research requires model systems as realistic and as close to the original patient as possible. In recent studies, slice cultures from tumor tissue, for example, head and neck squamous cell carcinoma [22], colorectal carcinoma [23], gastric and esophagogastric junction cancer [24], and GBM [25,26], have been shown to be a promising alternative to conventional cell culture or animal models. Slice cultures overcome interspecies differences, which often limit the translation of animal models into a clinical setting. Further, they offer a higher complexity and are closer to the *in vivo* situation than cell culture models. For GBM, the usability of such models could be enhanced by total RNA sequencing and the quantification of treatment effects within this method has been improved by the automation of histological staining analysis [26]. In the study presented here, the model system was further investigated regarding the reproducibility of the

achieved results among a larger cohort of GBM patients, thereby also addressing the intra- and intertumoral heterogeneity. Samples from 25 patients with primary GBM were processed into slice cultures, subjected to standard radiochemotherapy, and the total RNA was sequenced in treated versus untreated slices. Concomitantly, histological analyses were performed to correlate the results from distinct methods and to evaluate the preservation of the tissue throughout the cultivation and treatment period.

Material and methods

Patients and samples

Glioblastoma tissue samples were obtained by surgery of 16 male and 9 female patients diagnosed with primary glioblastoma (GBM, WHO grade IV). The patient data including PFS and OS are summarized in Table S1. Surgery and diagnosis were performed at the Department of Neurosurgery and the Department of Neuropathology, University Hospital Leipzig, Germany, and at the Department of Neurosurgery, City Hospital, Dessau, Germany, according to the EANO guideline for the diagnosis and treatment of anaplastic gliomas and glioblastoma [27]. All tissue samples were subjected to organotypic tissue slice cultures and replicate number ranged from 1 to 3 depending on the amount of tissue available for the cultivation. Tissue acquisition and experimental procedure were approved by the institutional research ethics board (Ethical Review Committee of the Medical Faculty of the University of Leipzig, #144/08-ek; registration numbers: IORG0001320, IRB00001750) and the ethic board of the Ärztekammer Sachsen-Anhalt, Halle (Saale) in accordance with the Helsinki Declaration (<https://www.wma.net/policies-post/wma-declaration-of-helsinki-ethical-principles-for-medical-research-involving-human-subjects/>). The patients provided written informed consent for experimental usage of their tissue samples and retrospective analysis of the data according to the General Data Protection Regulation of the European Community (<https://gdpr-info.eu/>).

Tissue slice preparation

Tissue slices were prepared according to a previously described protocol [25,26]. The slices were cultivated on a liquid/air interface in a humidified incubator at 37 °C and 5% CO₂ for 6–15 days in total and provided with fresh medium every 2–3 days.

Treatment of tissue slices

After 3–12 days in culture, slices were treated with temozolomide (TMZ, 200 µM) and X-irradiation (4 Gy) according to a previously described protocol [26]. In brief, 24 h after

the initial treatment with TMZ, x-irradiation was performed with a 200 kV irradiation machine (Gulmay Medical D3000, Gulmay, Surrey, UK) with a copper filter. The dose rate was 1.156 Gy·min⁻¹ and each sample was irradiated 3.46 min to reach the target dose of 4 Gy. Control samples were sham-irradiated.

Histology

Histological staining of Ki67 and TUNEL assays were done according to a previously described protocol [26].

Imaging and image analysis

Imaging of immunofluorescently stained microscope slides and image analysis of respective images was performed using previously described methods [26]. In brief, microscope slides were fully digitized at 20× magnification using a digital slide scanner (Pannoramic Scan II, 3D HISTECH Ltd., Budapest, Hungary) equipped with a quad band (DAPI/FITC/TRITC/Cy5) filter set and PNG images were exported from slide scanner data sets (PANNORAMIC VIEWER, version 1.15.4, 3D HISTECH Ltd., Budapest, Hungary) with pixel dimensions of 0.325 µm. Manual correction of artifacts (i.e., tissue overlaps, air bubbles, unspecific staining, dirt/fluorescent particles, and blooming) was carried out (Adobe Photoshop CS6, Adobe Systems Inc., San Jose, CA, USA) and spectral bleedthrough between different color channels was corrected using the ‘Spectral Unmixing’ plugin for IMAGEJ (version 1.51n, <http://imagej.nih.gov/ij/>). Image analysis was performed with MATHEMATICA (version 11.1, Wolfram Research, Inc., Champaign, IL, USA). Corrected fluorescence images were imported, split into separate color channels, and tissue masks as well as DAPI (blue channel) and proliferation marker (Ki67; green channel) masks were obtained using appropriate thresholding methods [28,29]. The resulting masks were further cleared of very small segments to eliminate specks of fluorescent particles within nuclei. Finally, the areas of total tissue, DAPI and Ki67 masks were determined and ratios were computed. Tissue slices with apoptosis staining underwent the same procedures. Apoptosis was captured using the TRITC filter (red channel) of the digital slide scanner. Image export, manual artifact correction, spectral unmixing, image analysis, and parameter calculation were performed as described above. Numbers of analyzed images are summarized in Table S2.

Statistical analysis of image quantification data

Statistical analysis was performed using IBM SPSS STATISTICS (version 22; IBM Corp.; Armonk, New York, USA). Descriptive statistics were calculated and boxplots were generated using MATHEMATICA. Data were tested for normal distribution using the Shapiro–Wilk test and expressed as median and interquartile range. Group comparisons were performed using Kruskal–Wallis test. Significance for all

tests was set at $P < 0.05$. To adjust the P -values for multiple comparisons, Dunn’s *post hoc* tests were performed.

RNA-sequencing

Total RNA from cultivated GBM tissue slices was isolated using the miRNeasy mini Kit (Qiagen, Hilden, Germany) following the provided manufacturer’s protocol. RNA yield was measured with the Qubit 2.0 instrument (Life Technologies, Darmstadt, Germany) using the RNA Broad Range Assay. The extracted RNA was collected and stored at –80 °C until further processing. To remove genomic DNA, it was subjected to double DNase digestion (TURBO DNA free Kit, Ambion, Thermo Fisher Scientific, Dreieich, Germany) before library preparation. RNA was quantified using a Qubit RNA-Kit and the DeNovix instrument (Biozym, Hessisch Oldendorf, Germany). RNA quality was analyzed on a Bioanalyzer 2100 instrument (Agilent Technologies, Waldbronn, Germany). For subsequent RNA-sequencing analyses, 200 ng of total RNA per sample was used. Library preparation was conducted using Truseq-Stranded total RNA Sample Prep kit (Illumina, Inc, San Diego, CA, USA) according to the manufacturers’ protocol. Molarity of each library was calculated and equal amounts were pooled and used for sequencing (12 pm). Sequencing was performed with 2 × 126-bp paired-end reads using HiSeq SBS Kit v4 chemistry on a HiSeq 2500 instrument (Illumina). 23–26 pooled libraries (in total 98) were sequenced on 4 flow cells.

Pre-processing of RNA sequencing data

To facilitate the multistep analysis of the RNA sequencing datasets, we applied the workflow-manager uap [30].

Primary and secondary data analysis

Demultiplexing of Illumina raw files was performed with the ILLUMINA BCL2FASTQ software, v.2.17.1 [31]. The paired-end FASTQ reads were trimmed and filtered using ADAPTERREMOVAL v.2.3.1 [32] with additional parameters to trim ambiguous bases (N) at 5'/3' termini (--trimns), remove low-quality bases (--trimqualities, --minquality 20) and keep reads with a minimum read length of 20bp (--minlength 20). Transcript abundance estimation of each sample was conducted using KALLISTO v.0.46.0 [33] by specifying a reverse stranded library. Human transcriptome FASTA file was downloaded from GENCODE (release 31 GRCh38.p12) and used to create a Kallisto index. Gene level quantifications were generated from the KALLISTO estimated counts per transcript using TXIMPORT v.1.18.0 [34].

Quality control

Sample QC was reported using FASTQC v.0.11.5 [35] to assess base call accuracy, PRESEQ v.2.0.3 [36] to evaluate the

library complexity. For each sample, a subsample of 1 million trimmed paired-end reads was randomly chosen by FASTQ-SAMPLE v.0.8 [37] using default parameters. Subsamples were aligned to human reference genome GRCh38/hg38 using HISAT2 v2.10 [38]. Duplication metrics were collected using PICARD TOOLS v2.3.0 (<http://broadinstitute.github.io/picard/>) function MarkDuplicates using BAM files generated by HISAT2. Picard's CollectRnaSeqMetrics was used to collect mapping percentages on intergenic, intronic, coding and UTR regions as well as gene body coverage. RSeQC v.3.0.0 [39], was used to determine, read GC content, junction saturation, read pair inner distance, and strandness of reads. Aggregated data visualization for the secondary analysis and quality control were generated using the MultiQC [40] framework. FASTQ SCREEN v.0.14 [41] in conjunction with bowtie2 [42] was conducted to assess RNA library composition (Table S3). For 13 samples, a noteworthy fraction from 30% to 75% of the subsampled reads mapped against human rRNA transcripts (Fig. S1c,d). The number of aligned reads using the Kallisto pseudoaligner ranged from 2.8 to 63.2 million (Fig. S1e). For principal component analysis (PCA), the gene counts were normalized using a variance-stabilizing transformation as implemented in DESeq2 v1.30.1 [43]. This was run with the option 'blind = TRUE' in order to compare samples in an unbiased manner. PCA of samples was based on the 5000 most variable genes. The variation in the first component is partly explained by samples in which an increased percentage of reads mapped against the human rRNA reference (Fig. S1f). A pairwise correlation analysis was performed between the replicates (if available) of each sample group (treated and untreated GBM tissue slices). A weaker correlation was observed in sample groups whose replicates were enriched in human rRNA (Fig. S2).

Sample filtering

Samples in which the subsampled reads mapped with at least 30% against the human rRNA reference or with a library size (sum of all raw counts) less than 10 million were removed from further analyses (82 out of 98 samples remained). Furthermore, only matched pairs of treated and untreated samples were analyzed. A total of 80 samples from each of 23 treated and untreated GBM tissue slices were analyzed. For each GBM tissue slice, 1–3 replicates were available.

Differential gene expression analysis

Differential expression between treated and untreated samples was assessed with negative binomial models by using the R/Bioconductor library DESeq2 v1.30.1 [43]. An unspecific expression filter was applied to the gene count matrix. This means that at least 5 counts had to be present in at least 25% of all samples. For each gene that passed

the expression filter, a generalized linear model was fitted using the formula: ~block + contrast, where block encoded the patient (to account for patient-specific differences in gene expression) and contrast was a factor containing information on both untreated and treated for each sample. Empirical estimation of the null distribution was performed with the FDRTOOL R PACKAGE v.1.2.16 [44] using the Wald statistic from DESeq2 as input. The estimated *P*-values were adjusted for multiple testing with the Benjamini-Hochberg correction [45]. A gene was considered significantly differentially expressed if the FDR-adjusted *P*-value was < 0.05. Regularized log2-fold-changes (lfc) were calculated using the lfcShrink() function from the DESeq2 package to account for the variance of lfcs estimates for genes with low read counts.

For hierarchical clustering (Fig. S3) of the significantly differentially expressed genes (DEGs), variance-stabilized gene counts were adjusted for the factor patient using the removeBatchEffect() function in the R/BIOCONDUCTOR LIMMA v.3.46.0 package [46].

Immune microenvironment analyses

Deconvolution of gene expression data was performed by TIMER [47] implemented in immunedeconv R package [48]. We filtered out those samples where the treatment strategy of the patients was not comparable to that of the GBM tissue slices. A total of 56 samples from each of 16 treated and untreated GBM tissue slices with 1–3 replicates were analyzed. Transcripts per million (TPM)-normalized gene expression data in non-log space were used as input for estimation of immune cell infiltrates. For all further analyses, the median of the relative abundance of immune cell types (relative infiltration scores) estimated by TIMER was calculated from GBM slice samples with more than one replicate. A Wilcoxon rank sum test for paired samples was performed to calculate the statistical significance of the estimated relative infiltration scores of immune cell types between treated and untreated GBM tissue slices. The association between standardized relative infiltration scores and the OS for untreated samples was assessed using the univariate Cox proportional hazards regression analysis. The *P*-values and 95% Cis for Cox proportional hazard model were computed by the R function coxph() in survival v.3.2.7 R package [28].

Pathway analysis

Gene enrichment analysis for significantly DEGs was performed using the R package clusterProfiler [29] on the WikiPathways database [49]. Significance of enrichment was assessed by a hypergeometric test and adjusted *P*-values for multiple testing were calculated based on the Benjamini-Hochberg method (adjusted *P*-value < 0.05). Furthermore, at least 5 significantly DEGs must be significantly enriched in the pathways.

Results

Tissue slices from long-term survivors show increased apoptosis but no difference in proliferation rate after treatment

To monitor treatment-mediated effects in cultivated GBM tissue slices from human patients, immunofluorescence staining for proliferation and apoptosis was done in treated and untreated paraffin-embedded slices

(Fig. 1). Apoptosis was detected by TUNEL staining (Fig. 1A–D). Untreated slices are shown as examples (Fig. 1A,B,E,F). Fig. 1C,D Shows the quantification of apoptosis in samples sorted by the patient's OS and progression-free survival (PFS) in months. The following groups were defined: OS ≤ 10 months, OS > 10 months, OS > 15 months, OS > 24 months (=defined as long-term survivors); PFS ≤ 7 months, PFS > 7 months, PFS > 12 months. Significantly increased apoptosis was

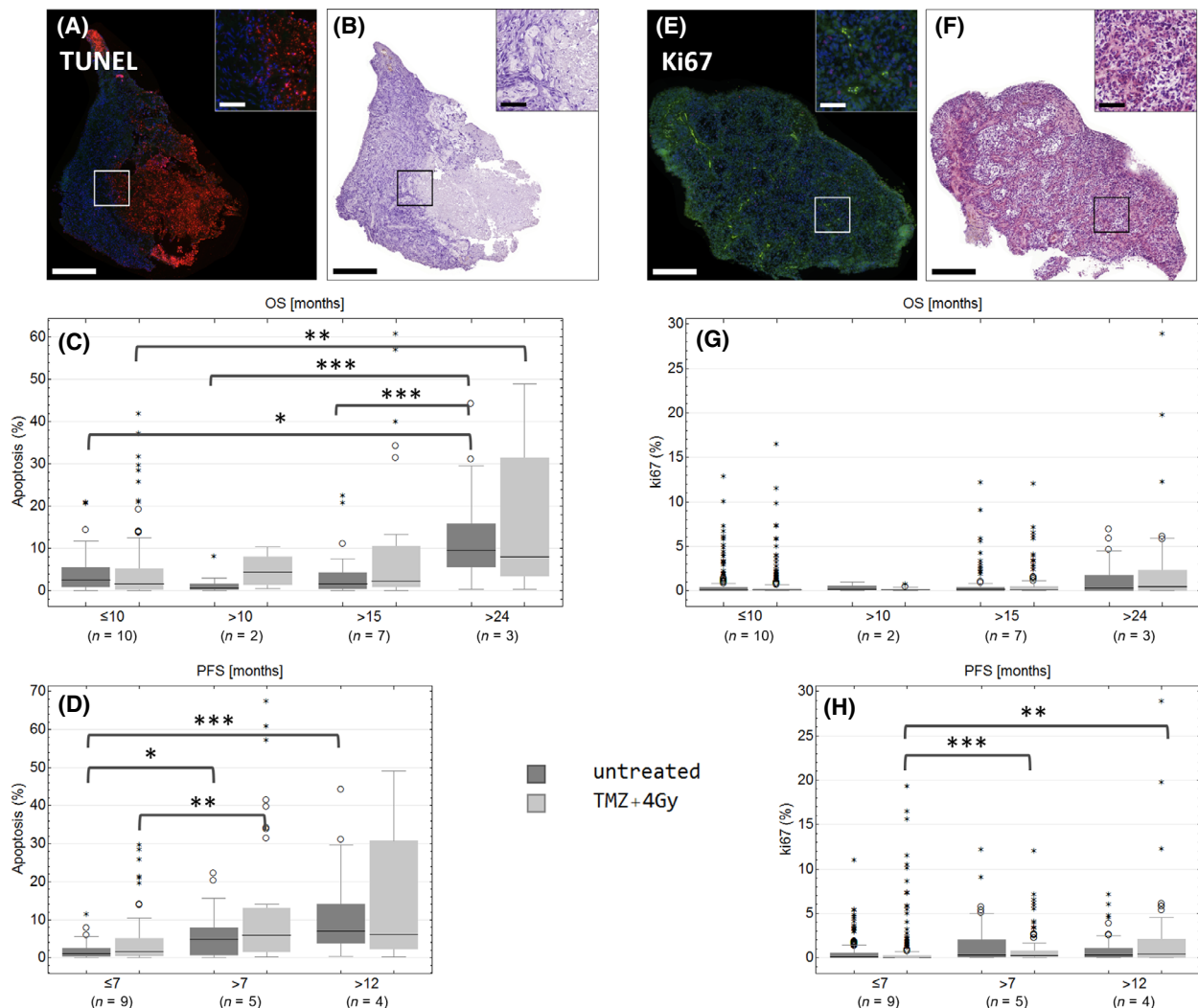


Fig. 1. TUNEL (A–D) and Ki67 (E–H) staining in treated (light gray, 'TMZ+4 Gy') or untreated slices (dark gray, 'untreated') were stained with TUNEL assay (red, A–D) or with an antibody against Ki67 (green, E–H). Fluorescence (A, E) and bright-field images (B, F) were recorded by a digital slidescanner. Representative images of untreated sectional samples are presented (A–B, E–F). For quantification, the total tissue area, DAPI-positive nuclei area, and the Ki67-positive or TUNEL-positive area were determined. Samples were assayed in groups concerning OS (months) and PFS (months). Numbers of biological replicates are as follows: OS ≤ 10: n = 10, OS > 10: n = 2, OS > 15: n = 7, OS > 24: n = 3, PFS ≤ 7: n = 9, PFS > 7: n = 5, PFS > 12: n = 4. Outliers are marked with small circles (O) and extreme values are marked with small asterisks (*). Scale bars: 500, 100 µm in the caption. P-values were adjusted by Kruskal–Wallis test with Dunn's post hoc test for multiple comparisons. Large asterisks centered above the brackets indicate significant differences: ***P ≤ 0.001, **P ≤ 0.01, *P ≤ 0.05.

found in long-term survivors in comparison to patients with OS \leq 10 months, both in untreated (median 9.52% vs. 2.55%, $P = 0.014$) and treated slices (8.00% vs. 1.58%, $P = 0.008$; Fig. 1C). Further, significantly higher apoptosis (9.52%) was detected in untreated samples of long-term survivors compared to patients with OS of 10–15 months (0.62%, $P = 0.001$) and 15–24 months (1.63%, $P = 0.001$). No significant difference in apoptosis was found between treatment and control, but there was a tendency of treatment-mediated apoptosis in slices from patients with OS longer than 10 months (Fig. 1C). Samples from patients with PFS > 7 months showed significantly higher median apoptosis in treated samples (5.96%) compared to patients with lower PFS (1.68%, $P = 0.003$; Fig. 1D). Samples from patients with PFS > 12 months showed even higher apoptotic rates in treated slices (6.16%), but without statistical significance due to the high variation within this group ($P = 0.058$; Fig. 1D). The apoptotic rate was significantly lower in untreated samples of patients with PFS \leq 7 months (1.12%) compared to patients with PFS > 7 months (4.81%, $P = 0.019$) and patients with PFS > 12 months (6.99%, $P = 4 \times 10^{-6}$; Fig. 1D).

Proliferation within GBM slices was detected by antibody staining of Ki67 (Fig. 1E–H). Quantification of Ki67 in groups with different OS did not reveal any significant difference between these groups or between untreated and treated samples, but there was a slight tendency that samples from long-term survivors had more Ki67-positive area than the others (Fig. 1G). In general, the proliferation rate was low, treated samples from patients with PFS \leq 7 months exhibited even lower proliferation rate (0.05%) compared to samples with PFS over 7 months (0.27%, $P = 1.3 \times 10^{-5}$) and samples with PFS > 12 months (0.39%, $P = 0.007$; Fig. 1H).

Immune constitution in treated and untreated GBM tissue slices

For the following analysis, only the samples from patients ($n = 15$) that have been clinically treated by radiochemotherapy with TMZ were used to ensure the highest reliability of the results. Using the RNA sequencing data and analyzing it by the TIMER deconvolution method, the estimated relative abundance of tumor-infiltrating immune cells in treated and untreated GBM tissue slices was quantified (Fig. 2A). TIMER has been developed to systematically evaluate the clinical impact of certain immune cells in cancer samples [47]. Each dot represents one tissue slice or, in case of technical/biological replicates, the median relative abundance. Treated and untreated samples of one

patient are linked by lines (Fig. 2A). The relative abundance of B cells was significantly reduced in treated samples ($P = 0.039$), whereas CD8⁺ T cells, CD4⁺ T cells, neutrophils, macrophages, and dendritic cells did not exhibit any significant differences between treated and untreated slices (Fig. 2A). The relative abundance of tumor-infiltrating immune cells was further correlated with clinical data of the patients, such as MGMT methylation state, PFS, or OS (Spearman's correlation, Fig. 2B). Samples from long-term survivors exhibited an increased relative abundance of CD8⁺ T cells and myeloid dendritic cells, whereas the relative abundance of CD4⁺ T cells was reduced in comparison to samples from patients with lower OS (Fig. 2C). The complete results of the immune micro-environment analyses are given in Fig. S4. The hazard ratios (HR) of CD8⁺ T cells ($P = 0.017$) and macrophages ($P = 0.081$) were 0.47 and 0.57, respectively. The HR of myeloid dendritic cells ($P = 0.082$) was 0.38 (Fig. 2D). The HR of CD4⁺ T cells was 1.51 ($P = 0.073$), and those of neutrophils ($P = 0.456$) and B cells ($P = 0.527$) were 1.20 and 0.84, respectively (Fig. 2D).

Differential gene expression between treated and untreated GBM

The analysis of DEGs between treated and untreated GBM tissue slices revealed that the majority of DEGs (total: 125, up: 85, down: 40) belonged to the fraction of protein-coding genes (up: 58, down: 32, Fig. 3A). 31 DEGs (up: 23, down: 8) could be identified as long noncoding RNA and four as pseudogenes (Fig. 3A). The top 20 up- and downregulated DEGs are shown in Fig. 3B in descending order of the respective lfc (Fig. 3B). A list of all DEGs is given in Table S4. Fig. 3C shows an excerpt of the significant DEGs in treated (yes, right) and untreated (no, left) GBM tissue slices for each individual patient (each dot represents one single patient). CDKN1A was the DEG with the highest lfc and was upregulated in nearly all treated samples compared to the untreated controls (median lfc = 0.89; Fig. 3C, Table S4). The same was true for DDB2 (lfc = 0.601) and AEN (lfc = 0.668), and GZMA was found to be downregulated (lfc = -0.336) in the majority of GBM samples (Fig. 3C, Table S4).

Treatment effects on biological processes and signaling pathways

The significant DEGs between treated and untreated GBM tissue slices were further subjected to pathway

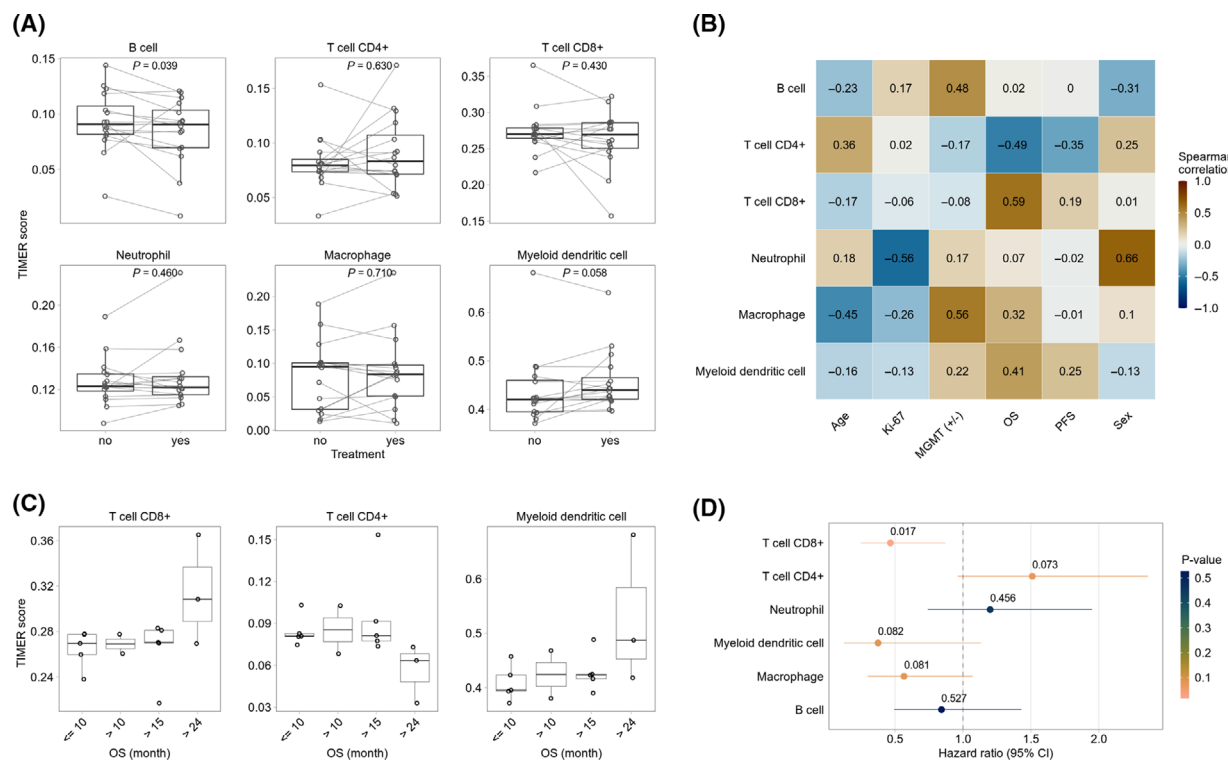


Fig. 2. Immune microenvironment analyses. (A) Estimated relative abundance of tumor-infiltrating immune cells using the TIMER deconvolution method in treated and untreated GBM tissue samples. Lines between dots indicate paired samples from the same patient. For patients with more than one replicate, the median relative abundance was calculated. The *P*-values indicate the statistical significance from the Wilcoxon test for paired samples. (B) The heatmap presents Spearman's correlation of clinical parameters and the relative abundance of tumor-infiltrating immune cells in untreated samples. (C) Examples from correlation analysis (B) between relative abundance of immune cell types and OS. (D) Association of relative abundance of tumor-infiltrating immune cells with overall patient survival. A univariate Cox regression was performed for untreated samples. The forest plot represents the HR and corresponding 95% confidence intervals (95%CI). The colors and numbers above the HRs depict the statistical significance (Wald test).

enrichment analyses (Fig. 4). The analysis of enriched signaling pathways by WikiPathways [50] demonstrated the highest enrichment of the TP53 network, the genotoxicity pathway, and the miRNA regulation of p53 pathway in prostate cancer (rich factors above 0.2, Fig. 4A). The highest number of DEGs (15) was found to be represented in the genotoxicity pathway, and 8–12 DEGs are part of DNA damage response and cancer pathways (melanoma, colorectal cancer, Fig. 4A). Figure 4B shows the top 3 most enriched pathways as a color-coded network of the corresponding DEGs (red: upregulated, *lfc* > 0; blue: downregulated, *lfc* < 0). The network further shows the interaction of different pathways, for example, by MDM2 (mouse double minute 2 homolog) which is involved in genotoxicity pathway, TP53 network as well as miRNA regulation of p53 pathway in prostate cancer. DDB2, GADD45A, and CDKN1A play roles in genotoxicity pathway and TP53 network, and BBC3 and BAX are important players in the TP53 network

as well as the miRNA regulation of p53 pathway in prostate cancer (Fig. 4B). The complete results of the WikiPathways analysis are given in Table S5.

Discussion

Slices from patients with OS > 10 months showed increased apoptosis after treatment with radio-chemotherapy (Fig. 1C), indicating a better response to the treatment and explaining longer OS. Patients with an OS ≤ 10 months exhibited lower or no apoptotic response to treatment. Slices from patients with a PFS > 12 months showed the highest apoptosis rate after treatment, indicating the highest susceptibility to cell death (Fig. 1D). Further, we did not find any significant difference in apoptosis between treated and untreated tissue slices, assuming that the detection of cell death might not be suitable for the monitoring of treatment effects. This could be due to limitations of the TUNEL assay in tumor tissue, for example, the

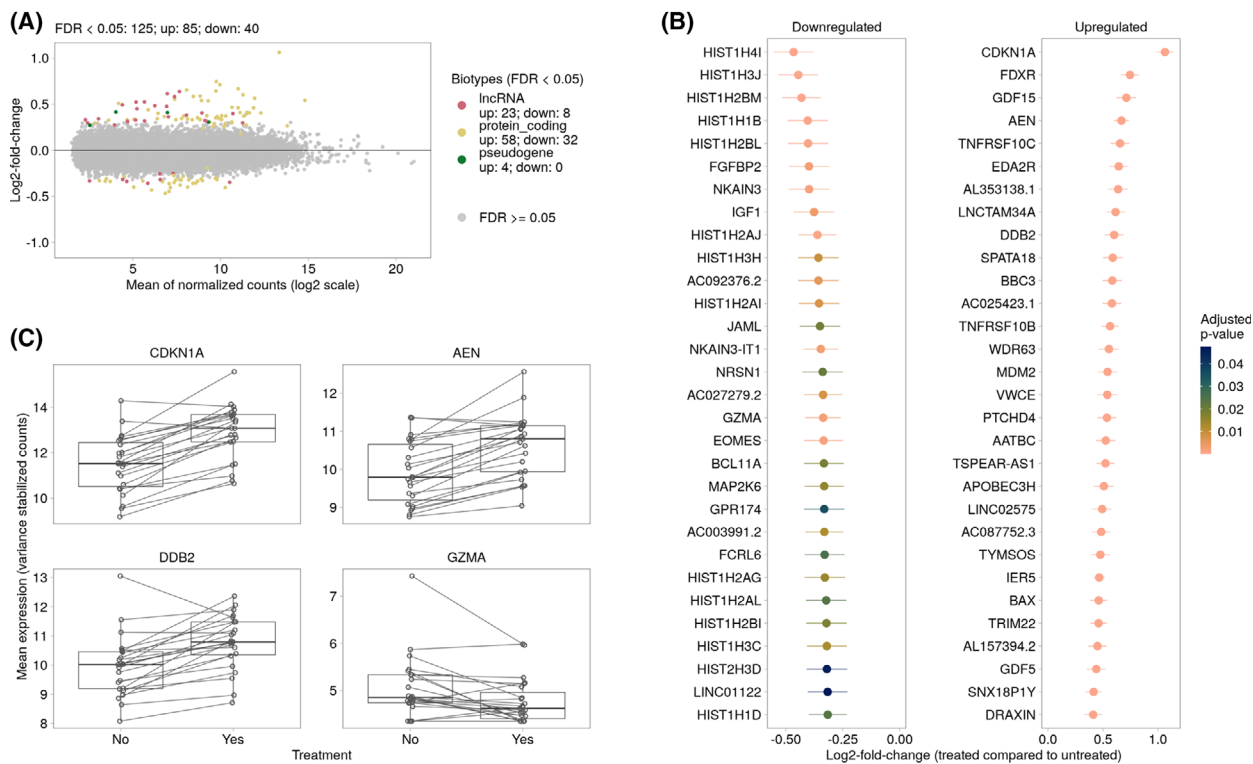


Fig. 3. Differential gene expression analysis between treated and untreated GBM tissue samples. (A) The MA-plot represents the relationship between normalized mean expression values and Ifcs for all analyzed genes. Each dot represents a gene. Significantly DEGs (FDR < 0.05) are colored according to their gene biotype. The legend shows the number of significantly upregulated (up) and downregulated (down) genes for each gene biotype. (B) Top 20 down- and up-regulated significantly regulated genes (treated compared to untreated samples). Genes are ranked by their shrunken Ifcs and colored according to their adjusted P-values. The vertical lines represent their estimates of standard error. (C) Examples of DEGs between treated and untreated GBM samples. Each dot represents one patient, the line links treated and untreated samples. For patients with more than one replicate, the average variance stabilized expression values were calculated.

occurrence of false-positive signals in highly proliferative cells or the emergence of necrosis which also produces DNA single strands leading to TUNEL-positive signals even in untreated samples [51]. The proliferation rates were significantly higher in slices from patients with a PFS > 7 and > 12 months than in the low PFS group. Proliferating tissue is more susceptible to radiation [52] and it could be shown for other tumor entities, for example, prostate cancer or oral squamous cell carcinoma, that a higher proliferation index is associated with an increased radiosensitivity of the tumor [53,54]. This could be an explanation for the higher Ki67-positive area in slices from patients with longer PFS, indicating a beneficial effect of the radiation. In addition, the slices from patients with an OS > 24 months exhibited higher proliferation rates. Although the difference was not statistically significant and the proliferation rates were extremely low across all samples, this observation should be handled with caution. An analysis of a larger patient cohort would

be required to strengthen this finding and to validate whether Ki67 expression in tumor slices could serve as a predictive marker for radiosensitivity in GBM.

For the implementation of the TIMER deconvolution method, only samples from patients clinically treated with radiation therapy and TMZ have been used to increase the reliability of the correlation with patient survival data. The analysis of tumor-infiltrating immune cells revealed a slight reduction of B cells after treatment. The populations of CD4⁺ and CD8⁺ T cells, neutrophils, macrophages, and dendritic cells were not affected by treatment indicating no effect of the relative abundances of these cell types on the OS of patients (Fig. 2A). B cells have been shown to play a crucial role in the development of an inflammatory environment which promotes carcinogenesis [55]. Therefore, a reduction of B cells after treatment could provide a hint of reduced tumor-promoting inflammation within these samples. It was further shown that the relative abundance of CD8⁺ T cells was increased

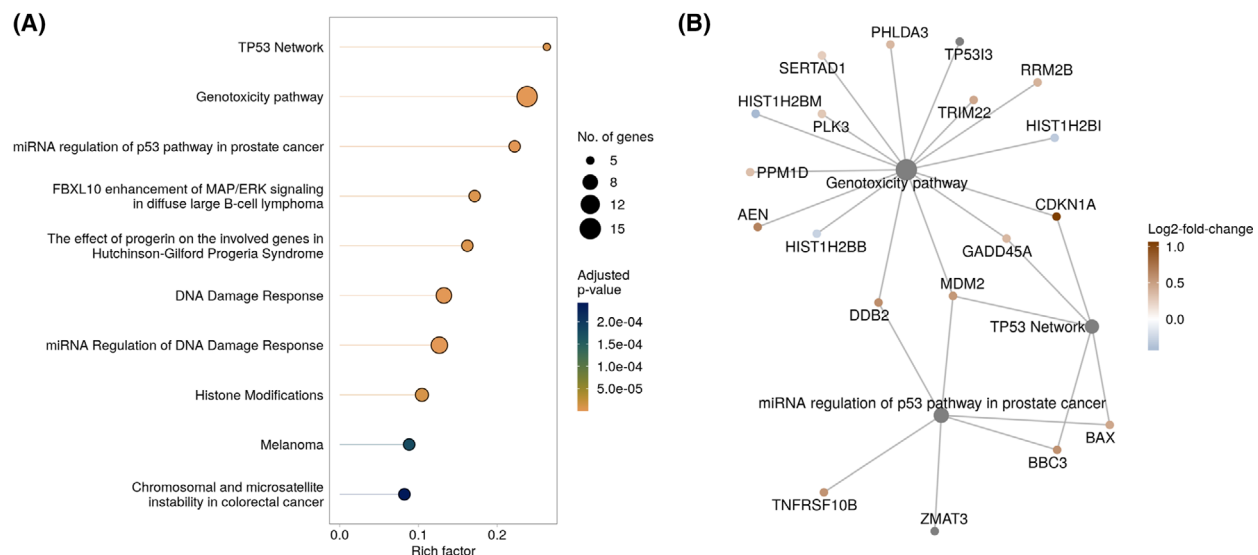


Fig. 4. Pathway enrichment analysis of DEGs between treated and untreated GBM samples. (A) The top 10 significantly enriched pathways ($FDR < 0.05$) form the WikiPathways database identified by over-representation analysis. The x-axis indicates the rich factor which is the number of DEGs in the pathway divided by the number of background genes in the pathway. The size of the bubble indicates the number of involved DEGs in the pathway. The colors indicate adjusted P -values of the significantly enriched pathways. (B) The linkages of genes and pathways as a network are shown. Significantly downregulated genes are shown in blue, upregulated genes in red. Shown are the identified DEGs of the three most enriched pathways.

in samples from patients with OS > 24 months (Fig. 2C). Cytotoxic T lymphocytes have been demonstrated to form immunological synapses with tumorigenic cells in GBM thereby suggesting a role in antitumor immune responses and tumor clearance [56]. This could also explain the higher apoptosis in slices from long-term survivors, in both treated and untreated tissue (Fig. 1C). Further, it was shown for various cancers that a local infiltration of CD8⁺ T cells into the tumor area was correlated with a favorable prognosis [57,58]. Dendritic cells are well-established antigen-presenting cells and are crucial for the activation of T lymphocytes [59]. In the context of cancer, dendritic cells prime cytotoxic T cells via antigen presentation on MHC-I molecules and thereby enable them to specifically target tumor cells [60,61]. A higher proportion of dendritic cells within samples from patients with OS > 24 months is in line with the higher proportion of CD8⁺ T cells (Fig. 2C).

The DEG with the highest median lfc in treated GBM slices was CDKN1A (p21). p21 is known to regulate the cell cycle and inhibit tumor growth. In accordance with that, expression of p21 leads to induction of apoptosis in GBM cells [62]. In GBM-derived cell lines, it was found that a lack of p53 resulted in the failure of apoptosis induction, suggesting a key mechanism to radioresistance which is often observed in GBM [62]. p53 mutations are very common among

GBM and approximately 85% of all GBMs exhibit a deregulation in p53 signaling [11]. In the study presented here, an enrichment of genes associated with miRNA regulation of p53 pathway in prostate cancer and the TP53 network in general was observed (Fig. 4) which gives a hint that p53 signaling has been affected by radiochemotherapy. We further found a significant upregulation of TP53I3 (tumor protein p53 inducible protein 3; lfc = 0.352, Table S4), the gene encoding for tumor protein p53 inducible protein 3 (PIG3). PIG3 expression is suppressed in GBM tissue compared to normal tissue and a higher expression is associated with a better prognosis as well as longer OS in GBM patients [63]. An increased expression in GBM slices after treatment indicates a response to the therapy.

GZMA, the gene encoding granzyme A, is mainly expressed upon activation of cytotoxic T cells and leads to apoptosis through activation of caspases [64]. CD8⁺ T cells and natural killer (NK) cells have the ability to kill cancer cells by overexpressing GZMA and perforin 1 [65]. Further, it was found for various cancer types that the presence of effector T cells within tumors is strongly associated with a better prognosis of the patient [66–68]. In GBM, a study revealed a better outcome for patients with lower expression levels of GZMA [69]. In our dataset of GBM patient tissues, the expression of GZMA was decreased upon treating the tissue slices with radiochemotherapy, indicating a

beneficial effect of the therapy (Fig. 3C). However, an alteration in the NK or CD8⁺ T cell population after treatment could not be detected (Fig. 2). This could be due to the restricted time point of the analysis when mRNA expression changes are already detectable, but an adjustment of cell populations would take some more time after the initiation of treatment.

AEN (apoptosis-enhancing nuclease) is induced by p53 and is regulated by its phosphorylation status upon DNA damage [70], for example, caused by irradiation. AEN, as a proapoptotic p53-dependent target gene, was further shown to be induced by irradiation in U251 MG GBM cells [71]. The upregulation of AEN in radiochemotherapy-treated GBM slices therefore is in line with the upregulation of CDKN1A as well as the treatment-mediated enrichment of the p53 network.

DDB2 (DNA damage binding protein 2) is one of the key DNA repair proteins which is assumed to have tumor-suppressing features and contribute to better treatment responses in tumors [72]. In GBM, an association of higher DDB2 expression with a better prognosis could be demonstrated. Concomitantly, patients with worse prognosis exhibited lower DDB2 expression [73]. In the GBM tissue slices, an increase of DDB2 expression was detected after treatment, being in line with the studies mentioned before.

One of the major problems of working with GBM tissue freshly resected from patients is the highly varying tissue quality, the limited amount of tissue and thus the lack or low number of biological replicates per experiment. Furthermore, high intra- as well as inter-tumoral heterogeneity can be observed. Another drawback is the missing opportunity to compare brain tumor tissue with healthy tissue from the same patient. Despite these limiting factors, we could show that the culture model combined with RNA sequencing is a suitable model to monitor treatment-mediated effects in GBM tissue slices on a transcriptional level. Interestingly, it was more difficult to reproduce these effects on a histological level by immunofluorescent staining. This could be due to the restricted time frame of the experimental setting where transcriptional changes can be seen early after onset of treatment, while changes at the protein or cellular level would take longer to manifest.

In conclusion, the study presented here, reproduces former studies, showing that GBM tissue slice cultures are suitable for RNA sequencing and automated histology, at a larger scale. The model system is now further improved by the correlation of the collected experimental data with the clinical course of each individual patient. At this point, it should be mentioned

that, in order to merge experimental with clinical data regarding OS and PFS, the cultures had been treated and analyzed several months (years) before clinical data were available. The rational for this approach was to identify molecular and physiological characteristics of the primary tumor and its response to therapy that could be used as valuable markers to predict outcome. To investigate potential therapeutic targets, predictive biomarkers, reasons for resistance to therapy, or genetic predispositions to develop GBM, a larger patient cohort should be analyzed as the general expression patterns in these samples seem to be unique for every single patient.

Acknowledgements

This study was supported by the Federal Ministry of Education and Research (Alternatives to animal testing, Project number: 031A579). We gratefully acknowledge the technical help of Rainer Baran-Schmidt. We thank the University Cancer Center Leipzig (UCCL) for the patients' follow-up and clinical course information. We acknowledge support from the German Research Foundation (DFG) and Leipzig University within the program of Open Access Publishing.

Conflict of interest

The authors declare no conflict of interest.

Data accessibility

The deep sequencing datasets generated and analyzed during the current study are available in the GEO repository [GSE179649](#). The histological datasets generated during the study are available from the corresponding author on reasonable request.

Author contributions

IB, FG, FR, FH, and JM managed the funding and conceptualization of the project and provided resources. SH, AH, NK, and DL conducted the experiments and collected data. SH, MR, KW, KR, and CB analyzed study data. CR and JM performed surgery. WM performed neuropathological diagnosis. SH, MR, and KW wrote the initial manuscript. All authors reviewed the manuscript.

References

- Louis DN, Perry A, Reifenberger G, von Deimling A, Figarella-Branger D, Cavenee WK, et al. The 2016

- World Health Organization Classification of Tumors of the Central Nervous System: a summary. *Acta Neuropathol.* 2016;131(6):803–20. <https://doi.org/10.1007/s00401-016-1545-1>
- 2 Louis DN, Ohgaki H, Wiestler OD, Cavenee WK, Burger PC, Jouvet A, et al. The 2007 WHO classification of tumours of the central nervous system. *Acta Neuropathol.* 2007;114(2):97–109. <https://doi.org/10.1007/s00401-007-0243-4>
 - 3 Wesseling P, Capper D. WHO 2016 classification of gliomas. *Neuropathol Appl Neurobiol.* 2018;44(2):139–50. <https://doi.org/10.1111/nan.12432>
 - 4 Stupp R, Mason WP, van den Bent MJ, Weller M, Fisher B, Taphoorn MJB, et al. Radiotherapy plus concomitant and adjuvant temozolomide for glioblastoma. *N Engl J Med.* 2005;352(10):987–96. <https://doi.org/10.1056/nejmoa043330>
 - 5 Stupp R, Hegi ME, Mason WP, van den Bent MJ, Taphoorn MJB, Janzer RC, et al. Effects of radiotherapy with concomitant and adjuvant temozolomide versus radiotherapy alone on survival in glioblastoma in a randomised phase III study: 5-year analysis of the EORTC-NCIC trial. *Lancet Oncol.* 2009;10(5):459–66. [https://doi.org/10.1016/S1470-2045\(09\)70025-7](https://doi.org/10.1016/S1470-2045(09)70025-7)
 - 6 Ohgaki H, Kleihues P. Genetic pathways to primary and secondary glioblastoma. *Am J Pathol.* 2007;170(5):1445–53. <https://doi.org/10.2353/ajpath.2007.070011>
 - 7 Ohgaki H, Dessen P, Jourde B, Horstmann S, Nishikawa T, Di Patre P-L, et al. Genetic pathways to glioblastoma: a population-based study. *Cancer Res.* 2004;64(19):6892–99. <https://doi.org/10.1158/0008-5472.CAN-04-1337>
 - 8 Tso C-L, Freije WA, Day A, Chen Z, Merriman B, Perlina A, et al. Distinct transcription profiles of primary and secondary glioblastoma subgroups. *Cancer Res.* 2006;66(1):159–67. <https://doi.org/10.1158/0008-5472.CAN-05-0077>
 - 9 Godard S, Getz G, Delorenzi M, Farmer P, Kobayashi H, Desbaillets I, et al. Classification of human astrocytic gliomas on the basis of gene expression: a correlated group of genes with angiogenic activity emerges as a strong predictor of subtypes. *Cancer Res.* 2003;63:6613–25.
 - 10 Ohgaki H, Kleihues P. The definition of primary and secondary glioblastoma. *Clin Cancer Res.* 2013;19(4):764–72. <https://doi.org/10.1158/1078-0432.CCR-12-3002>
 - 11 Brennan CW, Verhaak RGW, McKenna A, Campos B, Noushmehr H, Salama SR, et al. The somatic genomic landscape of glioblastoma. *Cell.* 2013;155(2):462–77. <https://doi.org/10.1016/j.cell.2013.09.034>
 - 12 Patel M, Vogelbaum MA, Barnett GH, Jalali R, Ahluwalia MS. Molecular targeted therapy in recurrent glioblastoma: current challenges and future directions. *Expert Opin Investig Drugs.* 2012;21(9):1247–66. <https://doi.org/10.1517/13543784.2012.703177>
 - 13 Karsy M, Neil JA, Guan J, Mahan MA, Mark MA, Colman H, et al. A practical review of prognostic correlations of molecular biomarkers in glioblastoma. *Neurosurg Focus.* 2015;38(3):E4. <https://doi.org/10.3171/2015.1.FOCUS14755>
 - 14 Lynes JP, Nwankwo AK, Sur HP, Sanchez VE, Sarpong KA, Ariyo OI, et al. Biomarkers for immunotherapy for treatment of glioblastoma. *J Immunother Cancer.* 2020;8(1):e000348. <https://doi.org/10.1136/jitc-2019-000348>
 - 15 Szopa W, Burley TA, Kramer-Marek G, Kasprzyk W. Diagnostic and therapeutic biomarkers in glioblastoma: current status and future perspectives. *Biomed Res Int.* 2017;2017:1–13. <https://doi.org/10.1155/2017/8013575>
 - 16 Arvanitis CD, Ferraro GB, Jain RK. The blood-brain barrier and blood-tumour barrier in brain tumours and metastases. *Nat Rev Cancer.* 2020;20(1):26–41. <https://doi.org/10.1038/s41568-019-0205-x>
 - 17 Jiang W, von Roemeling CA, Chen Y, Qie Y, Liu X, Chen J, et al. Designing nanomedicine for immuno-oncology. *Nat Biomed Eng.* 2017;1(2):1–11. <https://doi.org/10.1038/s41551-017-0029>
 - 18 Parker NR, Khong P, Parkinson JF, Howell VM, Wheeler HR. Molecular heterogeneity in glioblastoma: potential clinical implications. *Front Oncol.* 2015;5:55. <https://doi.org/10.3389/fonc.2015.00055>
 - 19 Verhaak RGW, Hoadley KA, Purdom E, Wang V, Qi Y, Wilkerson MD, et al. Integrated genomic analysis identifies clinically relevant subtypes of glioblastoma characterized by abnormalities in PDGFRA, IDH1, EGFR, and NF1. *Cancer Cell.* 2010;17(1):98–110. <https://doi.org/10.1016/j.ccr.2009.12.020>
 - 20 Lin C-HA, Rhodes CT, Lin C, Phillips JJ, Berger MS. Comparative analyses identify molecular signature of MRI-classified SVZ-associated glioblastoma. *Cell Cycle.* 2017;16(8):765–75. <https://doi.org/10.1080/15384101.2017.1295186>
 - 21 Patel AP, Tirosh I, Trombetta JJ, Shalek AK, Gillespie SM, Wakimoto H, et al. Single-cell RNA-seq highlights intratumoral heterogeneity in primary glioblastoma. *Science.* 2014;344(6190):1396–401. <https://doi.org/10.1126/science.1254257>
 - 22 Gerlach MM, Merz F, Wichmann G, Kubick C, Wittekind C, Lordick F, et al. Slice cultures from head and neck squamous cell carcinoma: a novel test system for drug susceptibility and mechanisms of resistance. *Br J Cancer.* 2014;110(2):479–88. <https://doi.org/10.1038/bjc.2013.700>
 - 23 Sönnichsen R, Hennig L, Blaschke V, Winter K, Körfer J, Hähnle S, et al. Individual susceptibility analysis using patient-derived slice cultures of colorectal carcinoma. *Clin Colorectal Cancer.* 2018;17(2):e189–99. <https://doi.org/10.1016/j.clcc.2017.11.002>

- 24 Koerfer J, Kallendrusch S, Merz F, Wittekind C, Kubick C, Kassahun WT, et al. Organotypic slice cultures of human gastric and esophagogastric junction cancer. *Cancer Med.* 2016;5(7):1444–53. <https://doi.org/10.1002/cam4.720>
- 25 Merz F, Gaunitz F, Dehghani F, Renner C, Meixensberger J, Gutenberg A, et al. Organotypic slice cultures of human glioblastoma reveal different susceptibilities to treatments. *Neuro Oncol.* 2013;15(6):670–81. <https://doi.org/10.1093/neuonc/not003>
- 26 Haehnel S, Reiche K, Loeffler D, Horn A, Blumert C, Puppel S-H, et al. Deep sequencing and automated histochemistry of human tissue slice cultures improve their usability as preclinical model for cancer research. *Sci Rep.* 2019;9:1–15. <https://doi.org/10.1038/s41598-019-56509-5>
- 27 Weller M, van den Bent M, Hopkins K, Tonn JC, Stupp R, Falini A, et al. EANO guideline for the diagnosis and treatment of anaplastic gliomas and glioblastoma. *Lancet Oncol.* 2014;15(9):e395–403. [https://doi.org/10.1016/S1470-2045\(14\)70011-7](https://doi.org/10.1016/S1470-2045(14)70011-7)
- 28 Otsu N. A threshold selection method from gray-level histograms. *IEEE Trans Syst Man Cybern.* 1979;9(1):62–6. <https://doi.org/10.1109/tsmc.1979.4310076>
- 29 Kapur JN, Sahoo PK, Wong AKC. A new method for gray-level picture thresholding using the entropy of the histogram. *Comput Gr Image Process.* 1985;29(3):273–85. [https://doi.org/10.1016/0734-189x\(85\)90125-2](https://doi.org/10.1016/0734-189x(85)90125-2)
- 30 Kämpf C, Specht M, Scholz A, Puppel S-H, Doose G, Reiche K, et al. uap: reproducible and robust HTS data analysis. *BMC Bioinform.* 2019;20: <https://doi.org/10.1186/s12859-019-3219-1>
- 31 bcl2fastq. Available at https://emea.support.illumina.com/sequencing/sequencing_software/bcl2fastq-conversion-software.html
- 32 Schubert M, Lindgreen S, Orlando L. AdapterRemoval v2: rapid adapter trimming, identification, and read merging. *BMC Res Notes.* 2016;9:1–7. <https://doi.org/10.1186/s13104-016-1900-2>
- 33 Bray NL, Pimentel H, Melsted P, Pachter L. Near-optimal probabilistic RNA-seq quantification. *Nat Biotechnol.* 2016;34(5):525–7. <https://doi.org/10.1038/nbt.3519>
- 34 Soneson C, Love MI, Robinson MD. Differential analyses for RNA-seq: transcript-level estimates improve gene-level inferences. *F1000Research.* 2015;4:1521. <https://doi.org/10.12688/f1000research.7563.2>
- 35 Andrews S. FastQC. Available at <https://www.bioinformatics.babraham.ac.uk/projects/>. 2010.
- 36 Daley T, Smith AD. Predicting the molecular complexity of sequencing libraries. *Nat Methods.* 2013;10(4):325–7. <https://doi.org/10.1038/nmeth.2375>
- 37 fastq-tools. Available at <https://homes.cs.washington.edu/~dcjones/fastq-tools/>
- 38 Kim D, Paggi JM, Park C, Bennett C, Salzberg SL. Graph-based genome alignment and genotyping with HISAT2 and HISAT-genotype. *Nat Biotechnol.* 2019;37(8):907–15. <https://doi.org/10.1038/s41587-019-0201-4>
- 39 Wang L, Wang S, Li W. RSeQC: quality control of RNA-seq experiments. *Bioinformatics.* 2012;28(16):2184–5. <https://doi.org/10.1093/bioinformatics/bts356>
- 40 Ewels P, Magnusson M, Lundin S, Käller M. MultiQC: summarize analysis results for multiple tools and samples in a single report. *Bioinformatics.* 2016;32(19):3047–3048. <https://doi.org/10.1093/bioinformatics/btw354>
- 41 Wingett SW, Andrews S. FastQ Screen: a tool for multi-genome mapping and quality control. *F1000Research.* 2018;7:1338. <https://doi.org/10.12688/f1000research.15931.2>
- 42 Langmead B, Salzberg SL. Fast gapped-read alignment with Bowtie 2. *Nat Methods.* 2012;9(4):357–359. <https://doi.org/10.1038/nmeth.1923>
- 43 Love MI, Huber W, Anders S. Moderated estimation of fold change and dispersion for RNA-seq data with DESeq2. *Genome Biol.* 2014;15(12):1–21. <https://doi.org/10.1186/s13059-014-0550-8>
- 44 Strimmer K. fdrtool: a versatile R package for estimating local and tail area-based false discovery rates. *Bioinformatics.* 2008;24(12):1461–2. <https://doi.org/10.1093/bioinformatics/btn209>
- 45 Benjamini Y, Hochberg Y. Controlling the false discovery rate: a practical and powerful approach to multiple testing. *J Roy Stat Soc: Ser B (Methodol).* 1995;57(1):289–300. <https://doi.org/10.1111/j.2517-6161.1995.tb02031.x>
- 46 Ritchie ME, Phipson B, Di WU, Hu Y, Law CW, Shi W, et al. limma powers differential expression analyses for RNA-sequencing and microarray studies. *Nucleic Acids Res.* 2015;43(7):e47. <https://doi.org/10.1093/nar/gkv007>
- 47 Li B, Severson E, Pignon J-C, Zhao H, Li T, Novak J, et al. Comprehensive analyses of tumor immunity: implications for cancer immunotherapy. *Genome Biol.* 2016;17:1–16. <https://doi.org/10.1186/s13059-016-1028-7>
- 48 Sturm G, Finotello F, Petitprez F, Zhang JD, Baumbach J, Fridman WH, et al. Comprehensive evaluation of transcriptome-based cell-type quantification methods for immuno-oncology. *Bioinformatics.* 2019;35(14):i436–45. <https://doi.org/10.1093/bioinformatics/btz363>
- 49 Slenter DN, Kutmon M, Hanspers K, Riutta A, Windsor J, Nunes N, et al. WikiPathways: a multifaceted pathway database bridging metabolomics to other omics research. *Nucleic Acids Res.* 2018;46(D1):D661–7. <https://doi.org/10.1093/nar/gkx1064>
- 50 Pico AR, Kelder T, van Iersel MP, Hanspers K, Conklin BR, Evelo C. WikiPathways: pathway editing

- for the people. *PLoS Biol.* 2008;6(7):e184. <https://doi.org/10.1371/journal.pbio.0060184>
- 51 Ghosh AP, Roth KA. Detection of Apoptosis and Autophagy. <https://doi.org/10.1016/B978-0-12-386456-7.07406-2>
- 52 Mendonca MS, Rodriguez A, Alpen EL. Quiescence in 9L cells and correlation with radiosensitivity and PLD repair. *Radiat Res.* 1989;117(3):433. <https://doi.org/10.2307/3577349>
- 53 Freudlsperger C, Freier K, Hoffmann J, Engel M. Ki-67 expression predicts radiosensitivity in oral squamous cell carcinoma. *Int J Oral Maxillofac Surg.* 2012;41(8):965–9. <https://doi.org/10.1016/j.ijom.2012.04.014>
- 54 Ishibashi N, Maebayashi T, Aizawa T, Sakaguchi M, Nishimaki H, Masuda S. Correlation between the Ki-67 proliferation index and response to radiation therapy in small cell lung cancer. *Radiat Oncol.* 2017;12(1):16. <https://doi.org/10.1186/s13014-016-0744-1>
- 55 de Visser KE, Korets LV, Coussens LM. De novo carcinogenesis promoted by chronic inflammation is B lymphocyte dependent. *Cancer Cell.* 2005;7(5):411–23. <https://doi.org/10.1016/j.ccr.2005.04.014>
- 56 Barcia C, Gómez A, Gallego-Sánchez JM, Perez-Vallés A, Castro MG, Lowenstein PR, et al. Infiltrating CTLs in human glioblastoma establish immunological synapses with tumorigenic cells. *Am J Pathol.* 2009;175(2):786–798. <https://doi.org/10.2353/ajpath.2009.081034>
- 57 Fridman WH, Pagès F, Sautès-Fridman C, Galon J. The immune contexture in human tumours: impact on clinical outcome. *Nat Rev Cancer.* 2012;12(4):298–306. <https://doi.org/10.1038/nrc3245>
- 58 Reiser J, Banerjee A. Effector, memory, and dysfunctional CD8(+) T cell fates in the antitumor immune response. *J Immunol Res.* 2016;2016:8941260. <https://doi.org/10.1155/2016/8941260>
- 59 Fu C, Jiang A. Dendritic cells and CD8 T cell immunity in tumor microenvironment. *Front Immunol.* 2018;9:3059. <https://doi.org/10.3389/fimmu.2018.03059>.
- 60 Chen DS, Mellman I. Oncology meets immunology: the cancer-immunity cycle. *Immunity.* 2013;39(1):1–10. <https://doi.org/10.1016/j.jimmuni.2013.07.012>
- 61 Saxena M, Bhardwaj N. Re-emergence of dendritic cell vaccines for cancer treatment. *Trends Cancer.* 2018;4(2):119–37. <https://doi.org/10.1016/j.trecan.2017.12.007>
- 62 Shu HK, Kim MM, Chen P, Furman F, Julin CM, Israel MA. The intrinsic radioresistance of glioblastoma-derived cell lines is associated with a failure of p53 to induce p21(BAX) expression. *Proc Natl Acad Sci USA.* 1998;95(24):14453–58. <https://doi.org/10.1073/pnas.95.24.14453>
- 63 Quan J, Li Y, Jin M, Chen D, Yin X, Jin M. Suppression of p53-inducible gene 3 is significant for glioblastoma progression and predicts poor patient prognosis. *Tumour Biol.* 2017;39(3):101042831769457. <https://doi.org/10.1177/1010428317694572>
- 64 Johnson BJ, Costelloe EO, Fitzpatrick DR, Haanen JBAG, Schumacher TNM, Brown LE, et al. Single-cell perforin and granzyme expression reveals the anatomical localization of effector CD8+ T cells in influenza virus-infected mice. *Proc Natl Acad Sci USA.* 2003;100(5):2657–2662. <https://doi.org/10.1073/pnas.0538056100>
- 65 Roufas C, Chasiotis D, Makris A, Efthathiades C, Dimopoulos C, Zaravinos A. The expression and prognostic impact of immune cytolytic activity-related markers in human malignancies: a comprehensive meta-analysis. *Front Oncol.* 2018;8:27. <https://doi.org/10.3389/fonc.2018.00027>
- 66 Pagès F, Berger A, Camus M, Sanchez-Cabo F, Costes A, Molidor R, et al. Effector memory T cells, early metastasis, and survival in colorectal cancer. *N Engl J Med.* 2005;353(25):2654–66. <https://doi.org/10.1056/NEJMoa051424>
- 67 Sato E, Olson SH, Ahn J, Bundy B, Nishikawa H, Qian F, et al. Intraepithelial CD8+ tumor-infiltrating lymphocytes and a high CD8+/regulatory T cell ratio are associated with favorable prognosis in ovarian cancer. *Proc Natl Acad Sci USA.* 2005;102(51):18538–43. <https://doi.org/10.1073/pnas.0509182102>
- 68 Kawai O, Ishii G, Kubota K, Murata Y, Naito Y, Mizuno T, et al. Predominant infiltration of macrophages and CD8(+) T Cells in cancer nests is a significant predictor of survival in stage IV non-small cell lung cancer. *Cancer.* 2008;113:1387–95. <https://doi.org/10.1002/cncr.23712>
- 69 Nduom EK, Wei J, Yaghi NK, Huang N, Kong L-Y, Gabrusiewicz K, et al. PD-L1 expression and prognostic impact in glioblastoma. *Neuro Oncol.* 2016;18(2):195–205. <https://doi.org/10.1093/neuonc/nov172>
- 70 Kawase T, Ichikawa H, Ohta T, Nozaki N, Tashiro F, Ohki R, et al. p53 target gene AEN is a nuclear exonuclease required for p53-dependent apoptosis. *Oncogene.* 2008;27(27):3797–810. <https://doi.org/10.1038/onc.2008.32>
- 71 Ma H, Rao L, Wang HL, Mao ZW, Lei RH, Yang ZY, et al. Transcriptome analysis of glioma cells for the dynamic response to γ -irradiation and dual regulation of apoptosis genes: a new insight into radiotherapy for glioblastomas. *Cell Death Dis.* 2013;4(10):e895. <https://doi.org/10.1038/cddis.2013.41>
- 72 Zhao R, Cui T, Han C, Zhang X, He J, Srivastava AK, et al. DDB2 modulates TGF- β signal transduction in human ovarian cancer cells by downregulating NEDD4L. *Nucleic Acids Res.* 2015;43(16):7838–49. <https://doi.org/10.1093/nar/gkv667>
- 73 Batista LFZ, Roos WP, Christmann M, Menck CFM, Kaina B. Differential sensitivity of malignant glioma cells to methylating and chloroethylating anticancer drugs: p53 determines the switch by regulating xpc, ddb2, and DNA double-strand breaks. *Cancer Res.* 2007;67(24):11886–95. <https://doi.org/10.1158/0008-5472.CAN-07-2964>

Supporting information

Additional supporting information may be found online in the Supporting Information section at the end of the article.

Fig. S1. Quality Control of samples with respect to sequencing library composition, read alignment and sample variance. Following adapter trimming, each FASTQ file was assessed for average per base (a) and per sequence (b) quality as measured by Phred score. Samples with sequencing depth < 50000 were removed and are not shown in (c–f). (c) To assess the sequencing library composition, each sample was subsampled to randomly 1 million trimmed paired-end reads. FastQ Screen in conjunction with bowtie2 was conducted to detect possible contamination like for example bacteria and overrepresented fractions of RNA species like human rRNA. The y-axis depicts the percentage of first reads for each sample that aligned against the references from Table S3. Reads are classified into four distinct types indicating reads uniquely mapping in one sequence reference (one hit in one reference), reads with multiple mappings in one sequence reference (multiple hits in one reference), reads uniquely mapping in distinct sequence references (one hit in multiple references) and reads with multiple mappings in distinct sequence databases (multiple hits in multiple references). (d) Subsampled reads were mapped iteratively against the RNaMmer database v1.2, human rRNA and the human genome assembly GRCh38/hg38. Human rRNA reads are divided into sense, which resembles endogenous rRNA and anti-sense RNA which indicate rRNA antisense probes from the rRNA depletion step. Samples mapped with at least 30% against the human rRNA reference depicted with asterisks. (e) Quality assessment of read alignment. Number of fragments aligned or not aligned to the human hg38 reference transcriptome using the Kallisto pseudoaligner. Samples mapped with at least 30% against the human rRNA reference depicted with asterisks. (f) Principal component

analysis (PCA) of variance-stabilized counts based on the 5000 most variable genes. The upper plot depicts first and second principal components, the bottom plot the second and third principal component. The upper PCA is colored by library size (sum of all raw count for each sample) and shaped by treatment. The bottom PCA is colored by binned percentages of reads mapped against the human rRNA reference.

Fig. S2. Correlation analysis between replicates of each sample. For each sample group (treat and untreated GBM tissue slices), normalized expression levels were correlated between replicates (if available). The color of each hexagonal bin in the scatter plot represents the number of genes overlapping at that position. The Coefficient of Determination (R^2) and estimated regression model are shown. Axis labels are colored by binned percentages of reads mapped against the human rRNA reference. The last integer in the axis labels indicate the replicate. Treated samples are labeled by 'T'.

Fig. S3. Hierarchical clustering of treated and untreated GBM tissue samples based on significantly DEGs. Euclidean distance clustering and complete linkage was applied to visualize similarity between samples. Each column represents a sample, and each row represents a gene. Variance stabilized expression values for each gene were z-score standardized.

Fig. S4. Relationship between relative abundance of immune cell types estimated using the TIMER deconvolution method and clinical parameters. Relationship between relative abundance of immune cell types estimated using the TIMER deconvolution method and clinical parameters.

Table S1. Summarized data of the patient cohort.

Table S2. Numbers of analyzed images per condition and experiment.

Table S3. References used for FastQ Screen.

Table S4. Complete list of significantly DEGs ($FDR < 0.05$) between treated and untreated samples.

Table S5. Complete over-representation analysis (ORA) by WikiPathways.

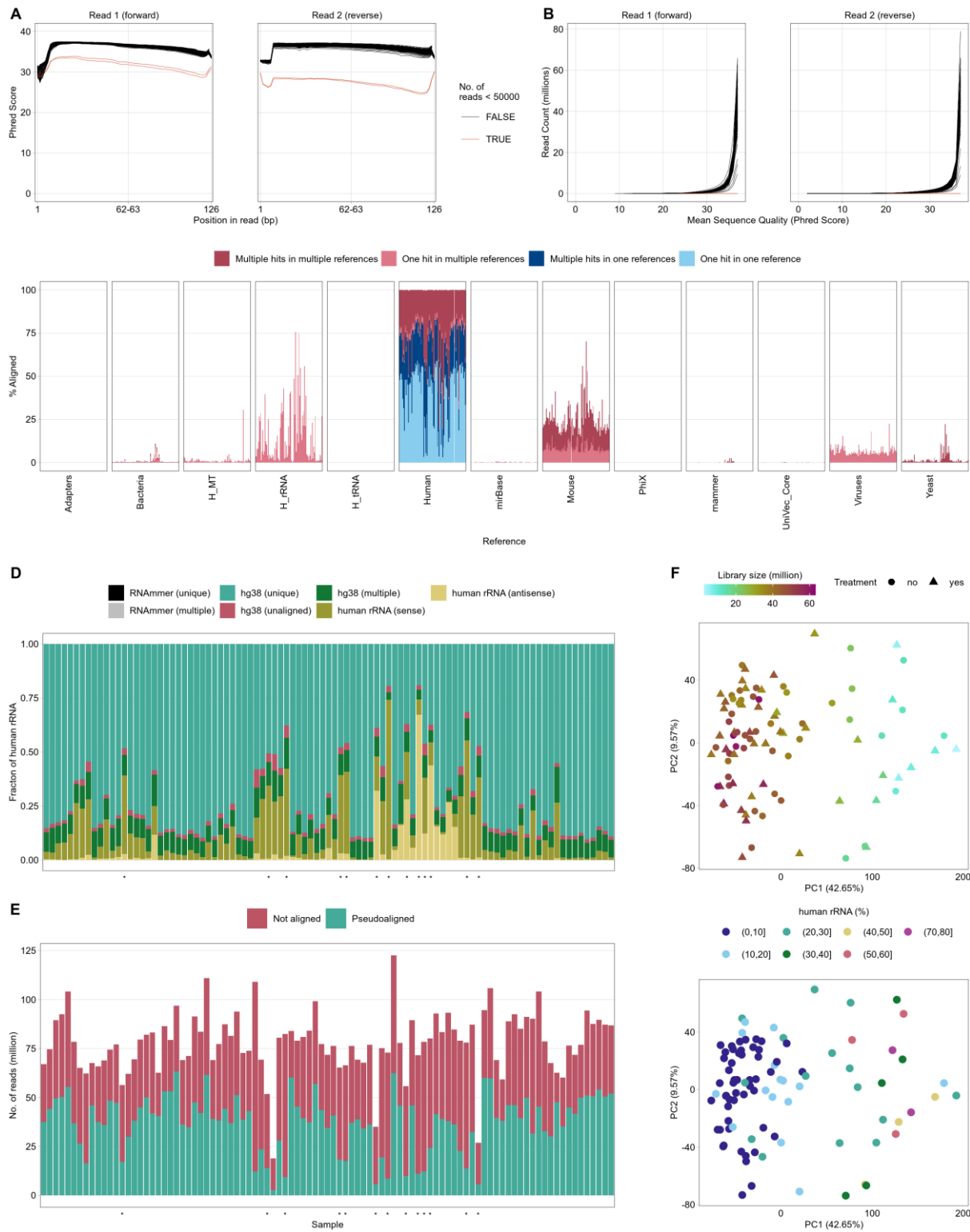


Figure S1: Quality Control of samples with respect to sequencing library composition, read alignment and sample variance. Following adapter trimming, each FASTQ file was assessed for average per base (a) and per sequence (b) quality as measured by Phred score. Samples with sequencing depth < 50000 were removed and are not shown in (c-f). (c) To assess the sequencing library composition, each sample was subsampled to randomly 1 million trimmed paired-end reads. FastQ Screen in conjunction with bowtie2 was conducted to detect possible contamination like for example bacteria and overrepresented fractions of RNA species like human rRNA. The y-axis depicts the percentage of first reads for each sample that aligned against the references from Table S1. Reads are classified into four distinct types indicating reads uniquely mapping in one sequence reference (one hit in one reference), reads with multiple mappings in one sequence reference (multiple hits in one reference), reads uniquely mapping in distinct sequence references (one hit in multiple references) and reads with multiple mappings in distinct sequence databases (multiple hits in multiple references). (d) Subsampled reads were mapped iteratively against the RNAmmer database v1.2, human rRNA and the human genome assembly GRCh38/hg38. Human rRNA reads are divided into sense, which resembles endogenous rRNA and anti-sense RNA which indicate rRNA antisense probes from the rRNA depletion step. Samples mapped with at least 30% against the human rRNA reference depicted with asterisks. (e) Quality assessment of read alignment. Number of fragments aligned or not aligned to the human hg38 reference transcriptome using the Kallisto pseudoaligner. Samples mapped with at least 30% against the human rRNA reference depicted with asterisks. (f) Principal component analysis (PCA) of variance-stabilized counts based on the 5000 most variable genes. The upper plot depicts first and second principal components, the bottom plot the second and third principal component. The upper PCA is colored by library size (sum of all raw count for each sample) and shaped by treatment. The bottom PCA is colored by binned percentages of reads mapped against the human rRNA reference.



Figure S2: Correlation analysis. For each sample group (treat and untreated GBM tissue slices), normalized expression levels were correlated between replicates (if available). The color of each hexagonal bin in the scatter plot represents the number of genes overlapping at that position. The Coefficient of Determination (R^2) and estimated regression model are shown. Axis labels are colored by binned percentages of reads mapped against the human rRNA reference. The last integer in the axis labels indicate the replicate. Treated samples are labeled by “T”.



Figure S3: Hierarchical clustering of treated and untreated GBM tissue samples based on significantly differentially expressed genes. Euclidean distance clustering and complete linkage was applied to visualize similarity between samples. Each column represents a sample, and each row represents a gene. Variance stabilized expression values for each gene were z-score standardized.

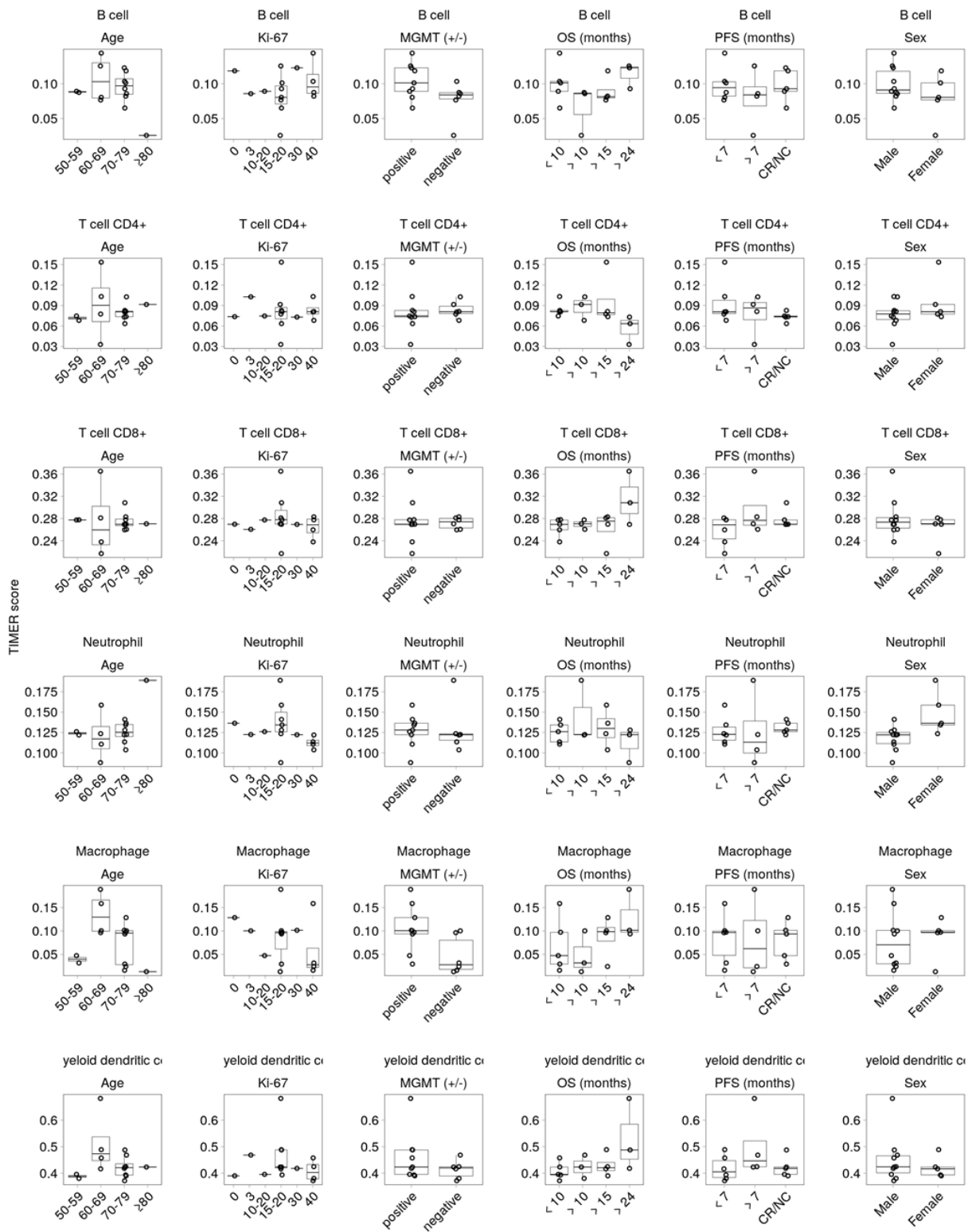


Figure S4: Immune microenvironment analyses. Relationship between relative abundance of immune cell types estimated using the TIMER deconvolution method and clinical parameters.

Supplementary Table S1: Summary of the patient cohort

Patient ID	Sex	Age	MGMT	PFS [months]	PFS [group]	OS [months]	OS [group]
01	M	67	positive	4.5	≤ 7	6	≤ 10
02	W	69	positive	5.5	≤ 7	16.5	> 15
03	W	86	positive	0.25	≤ 7	0.25	≤ 10
04	M	74	positive	-	> 12	32	> 24
05	W	64	positive	6	≤ 7	15.5	> 15
06	M	70	positive	7.5	> 7	9	≤ 10
07	M	54	positive	4.4	≤ 7	7.5	≤ 10
08	M	42	negative	NA	NA	NA	NA
09	M	84	positive	-	NA	5.5	≤ 10
10	M	56	negative	5.5	≤ 7	13	> 10
11	M	52	negative	10	> 7	15.5	> 15
12	M	77	negative	11.5	> 7	17.5	> 15
13	M	76	positive	NA	NA	8	≤ 10
14	W	74	positive	15	> 12	19.6	> 15
15	M	65	positive	32.5	> 12	52.4	> 24
16	M	77	negative	NA	NA	9.5	≤ 10
17	M	78	negative	6	≤ 7	7	≤ 10
18	W	81	negative	8	> 7	17	> 15
19	M	74	positive	-	> 12	35.5	> 24
20	M	75	negative	7.5	> 7	14.5	> 10
21	W	50	negative	NA	NA	NA	NA
22	W	68	negative	6	≤ 7	20.5	> 15
23	W	77	NA	NA	NA	0.3	≤ 10
24	M	59	NA	NA	NA	NA	NA
25	W	79	positive	5	≤ 7	10	≤ 10

Supplementary Table S2: Numbers of analyzed images per condition and experiment

Experiment	Condition	Number of analyzed images
Ki67	untreated	594
	TMZ+4Gy	638
TUNEL	untreated	241
	TMZ+4Gy	305

Supplementary Table S3: References used for FastQ Screen

Reference	Source
Adapter sequences	https://github.com/csf-nugs/fastqc/blob/master/Contaminants/contaminant_list.txt
Bacteria	ftp://ftp.ncbi.nih.gov/genomes/refseq/bacteria/ , Oct 2014
H_MT	human mitochondrial reference sequence in GRCh37/hg19
H_rRNA (human ribosomal RNA sequences)	NR_003286.1 (18S), NT_003287.1 (28S), NR_003285.2(5.8S), V00589.1 (5S), NC_012920.1: gi 251831106:1671-3229 (MT 16S) and NC_012920.1: gi 251831106:648-1601 (MT 12S)
H_tRNA (human transfer RNA sequences)	http://gtrnadb.ucsc.edu/genomes/eukaryota/Hsapi19/hg19-tRNAs.fa
Human genome	GRCh37/hg19, reference chromosomes only
mirBase	miRNA sequences from mirBase v21
Mouse genome	UCSC/mm10
PhiX	gi 9626q372 ref NC_001422.1 Enterobacteria phage phiX174 sensu lato, complete genome
RNAmer (predicted rRNA sequences)	http://www.cbs.dtu.dk/services/RNAmer/ , v1.2
UniVec Core	ftp://ftp.ncbi.nlm.nih.gov/pub/UniVec/UniVec_Core build 8.0, May 2015
Viruses	ftp://ftp.ncbi.nlm.nih.gov/genomes/refseq/viral/ , March 2014
Yeast	genome assembly SacCer3

Supplementary Table S4: Significantly differentially expressed genes (FDR < 0.05) between treated and untreated samples

ENSEMBL ID	Gene symbol	Log2-fold-change (SE)			P-value	Adjusted p-value	Mean expression for treated group	Mean expression for untreated group	Description
		Log2-fold-change	chan ge	(SE)					
ENSG00000124762.13	CDKN1A	1.063	0.083	2.715E-38	1.42E-12	15594.47	9	5655.656	cyclin dependent kinase inhibitor 1A [Source:HGNC Symbol;Acc:HGNC:1784]
ENSG00000130513.6	GDF15	0.712	0.089	1.247E-16	1.42E-12	1493.409	546.344	growth differentiation factor 15 [Source:HGNC Symbol;Acc:HGNC:30142]	
ENSG00000161513.12	FDXR	0.745	0.083	1.408E-19	1.42E-12	1194.43	563.601	ferredoxin reductase [Source:HGNC Symbol;Acc:HGNC:3642]	
ENSG00000162783.10	IER5	0.466	0.051	1.185E-19	1.42E-12	1903.474	1335.796	immediate early response 5 [Source:HGNC Symbol;Acc:HGNC:5393]	
ENSG00000181026.15	AEN	0.668	0.066	7.746E-24	1.42E-12	2683.532	1479.033	apoptosis enhancing nuclese [Source:HGNC Symbol;Acc:HGNC:25722]	
ENSG00000173535.14	TNFRSF1OC	0.655	0.084	3.594E-15	3.549E-12	386.624	160.795	TNF receptor superfamily member 10c [Source:HGNC Symbol;Acc:HGNC:11906]	
ENSG00000131080.15	EDA2R	0.643	0.088	6.264E-14	6.692E-11	1163.545	568.019	ectodysplasin A2 receptor [Source:HGNC Symbol;Acc:HGNC:17756]	
ENSG00000286811.1	AL35531381	0.637	0.089	7.876E-14	7.453E-11	294.026	118.284	novel transcript	
ENSG00000120889.13	TNFRSF10B	0.564	0.077	1.921E-13	1.68E-10	4953.019	2989.824	TNF receptor superfamily member 10b [Source:HGNC Symbol;Acc:HGNC:11905]	
ENSG00000234546.4	LNCTAM34A	0.614	0.085	3.279E-13	2.655E-10	161.467	91.481	long non coding transcriptional activator of miR34a [Source:HGNC Symbol;Acc:HGNC:52548]	
ENSG00000134574.11	DDB2	0.601	0.085	5.332E-13	4.02E-10	2969.709	2049.905	damage specific DNA binding protein 2 [Source:HGNC Symbol;Acc:HGNC:2718]	
ENSG00000256325.1	AC0254231	0.581	0.086	2.66E-12	1.991E-09	128.53	199.237	novel transcript	
ENSG00000235890.2	TSPEAR-AS1	0.523	0.083	1.154E-11	8.576E-09	60.536	14.426	TSPEAR antisense RNA 1 [Source:HGNC Symbol;Acc:HGNC:1271]	
ENSG00000105327.17	BBC3	0.584	0.087	1.323E-11	9.196E-09	480.42	228.414	BCL2 binding component 3 [Source:HGNC Symbol;Acc:HGNC:17868]	
ENSG00000163071.11	SPATA18	0.589	0.089	2.051E-11	1.36E-08	677.334	257.039	spematogenesis associated 18 [Source:HGNC Symbol;Acc:HGNC:29579]	
ENSG00000135679.25	MDM2	0.542	0.087	1.268E-10	8.628E-08	32552.63	25101.81	MDM2 proto-oncogene [Source:HGNC Symbol;Acc:HGNC:6973]	
ENSG00000162643.13	WDR63	0.554	0.089	1.619E-10	0.0000000	5	7	WD repeat domain 63 [Source:HGNC Symbol;Acc:HGNC:30711]	

ENSG0000002446			5.165E-07	913.479	365.831	patched domain containing 4 [Source:HGNC Symbol;Acc:HGNC:21345]
94.7 ENSG000001679	PTCHD4	0.536	0.088	6.114E-07	0.0000000	von Willebrand factor C and EGF domains [Source:HGNC Symbol;Acc:HGNC:26487]
92.13 ENSG000001322	VWCE	0.539	0.089	10.379	674.663	303.824
74.16 ENSG000002154	TRIM22	0.46	0.075	7.628E-07	4.542E-07	tripartite motif containing 22 [Source:HGNC Symbol;Acc:HGNC:16379]
58.8 ENSG000001547	AATBC	0.525	0.089	8.551E-07	4.877E-07	apoptosis associated transcript in bladder cancer [Source:HGNC Symbol;Acc:HGNC:51526]
67.14 ENSG000000870	XPC	0.406	0.067	1.069E-07	5.886E-07	XPC complex subunit, DNA damage recognition and repair factor [Source:HGNC Symbol;Acc:HGNC:12816]
88.20 ENSG000002538	BAX	0.461	0.077	1.913E-07	0.000001	
78.5 ENSG000002737	AC087752	0.400	0.077	2.779E-07	0.000001	BCL2 associated X, apoptosis regulator [Source:HGNC Symbol;Acc:HGNC:959]
03.1 ENSG000001971	HIST1H2BM	-0.432	0.085	7.219E-09	0.000003	
98.15 ENSG000001002	APOBEC3H	0.508	0.089	9.02E-09	845	38.697
53.4 ENSG000002287	HIST1H3J	-0.446	0.086	1.025E-07	0.000005	histone cluster 1 H2B family member m [Source:HGNC Symbol;Acc:HGNC:4750]
09.1 ENSG000001769	LINC02575	0.493	0.088	2.381E-08	0.0000012	apolipoprotein B mRNA editing enzyme catalytic subunit 3H [Source:HGNC Symbol;Acc:HGNC:24100]
12.4 ENSG000001708	TYMSOS	0.476	0.086	2.626E-08	0.0000012	histone cluster 1 H3 family member j [Source:HGNC Symbol;Acc:HGNC:4774]
36.11 ENSG000002861	PPM1D	0.334	0.06	2.868E-08	0.0000013	long intergenic non-protein coding RNA 2575 [Source:HGNC Symbol;Acc:HGNC:53747]
16.1 ENSG000002761	AL157394.2	0.45	0.082	3.33E-08	0.0000015	TYMS opposite strand [Source:HGNC Symbol;Acc:HGNC:29553]
80.1 ENSG000001726	HIST1H4I	-0.466	0.088	4.906E-08	0.0000022	protein phosphatase, Mg ²⁺ /Mn ²⁺ dependent 1D [Source:HGNC Symbol;Acc:HGNC:9277]
67.11 ENSG000002741	ZMAT3	0.405	0.075	5.209E-08	0.0000023	
62.1 ENSG000001843	SNX18P1Y	0.415	0.078	0.0000000	0.0000055	TYMS opposite strand [Source:HGNC Symbol;Acc:HGNC:29983]
57.4 ENSG000001624	HIST1H1B	-0.404	0.088	2.443E-08	0.0000110	sorting nexin 18 pseudogene 1, Y-linked [Source:HGNC Symbol;Acc:HGNC:38442]
90.7 ENSG000002255	DRAVIN	0.411	0.082	3.267E-07	0.0000145	
11.7 ENSG000001259	LINC00475	0.409	0.089	4.268E-07	0.0000187	zinc finger matrin-type 3 [Source:HGNC Symbol;Acc:HGNC:25054]
65.9 ENSG000002763	GDF5	0.439	0.089	4.474E-07	0.0000192	sorting nexin 18 pseudogene 1, Y-linked [Source:HGNC Symbol;Acc:HGNC:38442]
68.1 ENSG000002763	HIST1H2AJ	-0.361	0.084	9.157E-07	0.0000397	dorsal inhibitory axon guidance protein [Source:HGNC Symbol;Acc:HGNC:4719]
						long intergenic non-protein coding RNA 475 [Source:HGNC Symbol;Acc:HGNC:23569]
						growth differentiation factor 5 [Source:HGNC Symbol;Acc:HGNC:4220]
						histone cluster 1 H2A family member j [Source:HGNC Symbol;Acc:HGNC:4727]
						histone cluster 1 H2A family member i [Source:HGNC Symbol;Acc:HGNC:4793]
						histone cluster 1 H4 family member i [Source:HGNC Symbol;Acc:HGNC:4793]
						histone cluster 1 H4 family member j [Source:HGNC Symbol;Acc:HGNC:4793]
						histone cluster 1 H4 family member k [Source:HGNC Symbol;Acc:HGNC:4793]
						histone cluster 1 H4 family member l [Source:HGNC Symbol;Acc:HGNC:4793]
						histone cluster 1 H4 family member m [Source:HGNC Symbol;Acc:HGNC:4793]
						histone cluster 1 H4 family member n [Source:HGNC Symbol;Acc:HGNC:4793]
						histone cluster 1 H4 family member o [Source:HGNC Symbol;Acc:HGNC:4793]
						histone cluster 1 H4 family member p [Source:HGNC Symbol;Acc:HGNC:4793]
						histone cluster 1 H4 family member q [Source:HGNC Symbol;Acc:HGNC:4793]
						histone cluster 1 H4 family member r [Source:HGNC Symbol;Acc:HGNC:4793]
						histone cluster 1 H4 family member s [Source:HGNC Symbol;Acc:HGNC:4793]
						histone cluster 1 H4 family member t [Source:HGNC Symbol;Acc:HGNC:4793]
						histone cluster 1 H4 family member u [Source:HGNC Symbol;Acc:HGNC:4793]
						histone cluster 1 H4 family member v [Source:HGNC Symbol;Acc:HGNC:4793]
						histone cluster 1 H4 family member w [Source:HGNC Symbol;Acc:HGNC:4793]
						histone cluster 1 H4 family member x [Source:HGNC Symbol;Acc:HGNC:4793]
						histone cluster 1 H4 family member y [Source:HGNC Symbol;Acc:HGNC:4793]
						histone cluster 1 H4 family member z [Source:HGNC Symbol;Acc:HGNC:4793]

ENSG0000001307			0.0000001	468	2	2775.029	1691.818	sestrin 2 [Source:HGNC Symbol;Acc:HGNC:20746]
66.5	SESN2	0.408	0.085	468	2	2775.029	1691.818	sestrin 2 [Source:HGNC Symbol;Acc:HGNC:20746]
ENSG000001851	HIST1H2BL	-0.403	0.089	149	3	98.673	179.784	histone cluster 1 H2B family member I [Source:HGNC Symbol;Acc:HGNC:4748]
30.5	ENSG000000483	RRM2B	0.398	0.086	707	0.0011103	3651.135	2155.578 ribonucleotide reductase regulatory TP53 inducible subunit M2B [Source:HGNC Symbol;Acc:HGNC:17296]
92.11	ENSG000002285	MIR34AH	0.398	0.086	664	0.0011103	2008.352	1354.944 MIR34A host gene [Source:HGNC Symbol;Acc:HGNC:51913]
26.7	ENSG000002802	G	0.398	0.086	664	0.0000002	1354.944	MIR34A host gene [Source:HGNC Symbol;Acc:HGNC:51913]
22.1	ENSG000002209	AL365209.1	0.381	0.089	72	0.0011103	280.298	253.49 TEC
ENSG000001635	EOMES	-0.334	0.086	563	0.001431	5.798	15.292	eomesodermin [Source:HGNC Symbol;Acc:HGNC:3372]
08.12	ENSG000001859		0.0000003	563	0.000004	5.798	15.292	sodium/potassium transporting ATPase interacting 3 [Source:HGNC Symbol;Acc:HGNC:26829]
42.11	ENSG000001325	NKAIN3	-0.398	0.089	294	0.001703	182.76	364.934 eomesodermin [Source:HGNC Symbol;Acc:HGNC:3372]
17.15	ENSG000000541	SLC52A1	0.401	0.089	776	0.001864	111.077	64.394 solute carrier family 52 member 1 [Source:HGNC Symbol;Acc:HGNC:30225]
48.17	ENSG000002248	NDUFAF8	0.239	0.052	488	0.0000005	1802.335	1405.775 phosphohistidine phosphatase 1 [Source:HGNC Symbol;Acc:HGNC:30033]
77.4	ENSG000001456	GZMA	-0.336	0.077	368	0.002068	550.853	NADH:ubiquinone oxidoreductase complex assembly factor 8 [Source:HGNC Symbol;Acc:HGNC:33551]
49.8	ENSG000001171	IGSF21	0.375	0.089	569	0.0002399	702.173	495.385 immunoglobin superfamily member 21 [Source:HGNC Symbol;Acc:HGNC:28246]
54.12	ENSG000001961	ZNF79	0.305	0.068	825	0.002449	760.502	591.942 zinc finger protein 79 [Source:HGNC Symbol;Acc:HGNC:13153]
52.10	ENSG000001151	TP53I3	0.352	0.078	966	0.002455	1011.897	694.639 tumor protein p53 inducible protein 3 [Source:HGNC Symbol;Acc:HGNC:19373]
29.14	ENSG000001456	PLK2	0.375	0.083	186	0.00249	1356.172	808.824 polo like kinase 2 [Source:HGNC Symbol;Acc:HGNC:19699]
32.15	ENSG000002789	AL031587	0.0000007	506	0.002559	666.264	489.803	granzyme A [Source:HGNC Symbol;Acc:HGNC:4708]
48.1	ENSG000001374	.5	0.32	0.072	506	0.0000008	22.353	42.923 granzyme A [Source:HGNC Symbol;Acc:HGNC:4708]
41.8	ENSG000002749	FGFBP2	-0.399	0.089	67	0.00271	22.353	42.923 immunoglobin superfamily member 21 [Source:HGNC Symbol;Acc:HGNC:28246]
56.2	ENSG000002461	NKAIN3-IT1	-0.347	0.076	348	0.00276	1025.508	1866.284 NKAIN3 intronic transcript [Source:HGNC Symbol;Acc:HGNC:48595]
30.1	ENSG000000653	AC107959.2	0.331	0.079	27	0.00337	7.173	2.874 novel transcript
57.20	ENSG000001167	DGKA	0.255	0.058	74	0.003414	1321.805	1045.625 diacylglycerol kinase alpha [Source:HGNC Symbol;Acc:HGNC:2849]
17.13	ENSG000000805	GADD45A	0.372	0.085	69	0.003414	1553.336	980.337 growth arrest and DNA damage inducible alpha [Source:HGNC Symbol;Acc:HGNC:4095]
46.13	SESN1	0.366	0.084	95	0.003428	1106.904	704.807	sestrin 1 [Source:HGNC Symbol;Acc:HGNC:21595]

ENSG0000000174 27.16	IGF1	-0.376	0.089	0.000012	138.968	269.583	insulin like growth factor 1 [Source:HGNC Symbol;Acc:HGNC:5464]
ENSG000001968 34.12	POTEI	0.373	0.088	0.000013	65	0.003925	
ENSG000001743 07.6	PHLDA3	0.371	0.086	0.000014	77	0.004221	182.873 POTE ankyrin domain family member l [Source:HGNC Symbol;Acc:HGNC:37093]
ENSG000002779 54.1	AC092376 .2	-0.357	0.089	0.000018	96	0.004531	pleckstrin homology like domain family A member 3 [Source:HGNC:8934]
ENSG000002729 04.1	AL390726 .2	0.363	0.088	0.000019	68	0.005633	novel transcript, antisense to WWOX
ENSG000001283 42.5	LIF	0.375	0.089	0.000019	41	0.005777	170.868 93.77 novel transcript
ENSG000001808 34.7	MAP6D1	0.331	0.078	0.000024	7	0.005779	3382.316 1952.407 LIF interleukin 6 family cytokine [Source:HGNC Symbol;Acc:HGNC:6596]
ENSG000002865 22.1	HIST1H3 B	-0.302	0.086	0.000025	09	0.007029	399.095 273.897 MAP6 domain containing 1 [Source:HGNC Symbol;Acc:HGNC:25753]
ENSG000001708 35.14	CEL	0.365	0.089	0.000026	52	0.007362	602.53 1040.272 histone cluster 1 H3 family member b [Source:HGNC Symbol;Acc:HGNC:4776]
ENSG000001967 47.4	HIST1H2 A1	-0.354	0.089	0.000026	05	0.007414	134.799 89.431 carboxyl ester lipase [Source:HGNC Symbol;Acc:HGNC:1848]
ENSG000002615 37.1	AC027279 .2	-0.337	0.084	0.000028	42	0.007419	299.124 465.857 histone cluster 1 H2A family member i [Source:HGNC Symbol;Acc:HGNC:4725]
ENSG000001830 87.15	GAS6	0.343	0.083	0.000032	22	0.007837	21.213 28.791 novel transcript, sense intronic to WWOX
ENSG000002846 90.2	CD300H	0.272	0.077	0.000032	94	0.00897	1154.302 798.76 growth arrest specific 6 [Source:HGNC Symbol;Acc:HGNC:4168]
ENSG000001053 72.7	RPS19	0.264	0.064	0.000033	02	0.008825	15645.80 3.314 CD300H molecule (gene/pseudogene) [Source:HGNC Symbol;Acc:HGNC:52292]
ENSG000002637 27.1	AP001178 .1	0.341	0.085	0.000035	69	0.009062	12947.34 1 ribosomal protein S19 [Source:HGNC Symbol;Acc:HGNC:10402]
ENSG000002788 28.1	HIST1H3 H	-0.357	0.089	0.000035	89	0.009436	5.185 novel transcript
ENSG000002764 10.3	HIST1H2 BB	-0.272	0.078	0.000036	91	0.009436	238.822 437.647 histone cluster 1 H3 family member h [Source:HGNC Symbol;Acc:HGNC:4775]
ENSG000002540 03.1	AC003991	0.000047	0.000047	0.000049	65	0.009515	88.563 225.123 histone cluster 1 H2B family member b [Source:HGNC Symbol;Acc:HGNC:4775]
ENSG000002870 80.1	HIST1H3 C	-0.32	0.088	0.000049	44	0.01232	3.644 7.727 novel transcript
ENSG000000999 85.4	OSM	0.353	0.088	0.000051	87	0.01282	214.247 362.437 histone cluster 1 H3 family member c [Source:HGNC Symbol;Acc:HGNC:4768]
ENSG000001861 53.17	WWOX	-0.191	0.047	0.000051	34	0.01289	520.255 313.633 oncostatin M [Source:HGNC Symbol;Acc:HGNC:8506]
ENSG000001770 76.6	ACER2	0.344	0.087	0.000052	31	0.01289	557.532 646.497 WW domain containing oxidoreductase [Source:HGNC Symbol;Acc:HGNC:12799]

ENSG0000001970 19.5	SERTAD1	0.258	0.064	6	0.01291	849.327	679.467	SERTA domain containing 1 [Source:HGNC Symbol;Acc:HGNC:17932]
ENSG000001829 12.6	TSPEAR-	0.328	0.086	32	0.01345	48.008	24.53	TSPEAR antisense RNA 2 [Source:HGNC Symbol;Acc:HGNC:16428]
ENSG000001256 57.5	TNFSF9	0.343	0.088	79	0.01469	103.702	65.949	TNF superfamily member 9 [Source:HGNC Symbol;Acc:HGNC:11939] vitelline membrane outer layer 1 homolog [Source:HGNC Symbol;Acc:HGNC:30387]
ENSG000001828 53.12	VMO1	0.34	0.087	33	0.01469	321.273	237.444	
ENSG000001967 87.3	HIST1H2 AG	-0.329	0.089	88	0.01469	404.051	588.488	histone cluster 1 H2A family member g [Source:HGNC Symbol;Acc:HGNC:4737]
ENSG000002375 12.6	UNC5B-	0.297	0.078	96	0.01469	8.144	2.828	UNC5B antisense RNA 1 [Source:HGNC Symbol;Acc:HGNC:45096]
ENSG000002739 83.1	HIST1H3 G	-0.285	0.085	09	0.01482	168.943	288.85	histone cluster 1 H3 family member g [Source:HGNC Symbol;Acc:HGNC:4772]
ENSG000002498 59.11	PVT1	0.297	0.075	48	0.01547	2834.215	2093.119	Pvt1 oncogene [Source:HGNC Symbol;Acc:HGNC:9709] mitogen-activated protein kinase kinase 6 [Source:HGNC Symbol;Acc:HGNC:6846]
ENSG000001089 84.15	MAP2K6	-0.332	0.086	83	0.01562	353.422	466.355	
ENSG000002336 95.2	GAS6- AS1	0.323	0.087	43	0.01607	771.341	349.749	GAS6 antisense RNA 1 [Source:HGNC Symbol;Acc:HGNC:39826]
ENSG000002503 37.7	PURPL	0.405	0.089	0.000081	0.01791	631.789	360.195	p53 upregulated regulator of p53 levels [Source:HGNC Symbol;Acc:HGNC:48995]
ENSG000002612 22.3	AC064805 .1	0.274	0.082	47	0.01791	21.249	10.238	novel transcript
ENSG000002785 88.1	HIST1H2 B1	-0.322	0.089	67	0.01791	143.248	200.039	histone cluster 1 H2B family member i [Source:HGNC Symbol;Acc:HGNC:4756] BAF chromatin remodeling complex subunit BCL11A [Source:HGNC Symbol;Acc:HGNC:132221]
ENSG000001605 93.18	BCL11A	-0.333	0.087	83	0.01868	339.593	484.347	
ENSG000001832 66.21	JAML	-0.35	0.089	95	0.01924	117.991	203.011	junction adhesion molecule like [Source:HGNC Symbol;Acc:HGNC:19084] POTE ankyrin domain family member C [Source:HGNC Symbol;Acc:HGNC:33894]
ENSG000001790 57.13	POTEC	0.333	0.087	02	0.01924	568.963	352.77	immunoglobulin superfamily member 22 [Source:HGNC Symbol;Acc:HGNC:26750]
ENSG000002245 92.5	IGSF22	0.335	0.089	21	0.01975	43.168	24.817	
ENSG000001529 54.12	NRSN1	-0.338	0.089	9	0.02125	84.26	119.36	neurensin 1 [Source:HGNC Symbol;Acc:HGNC:17881]
ENSG000002245 75.6	AL139158	0.313	0.083	4	0.0216	32.877	19.66	novel transcript long intergenic non-protein coding RNA 2246 [Source:HGNC Symbol;Acc:HGNC:53135]
ENSG000002819 03.2	LINC0224 6	-0.254	0.066	7	0.02362	83.61	101.648	
ENSG000001245 44.10	HIST1H1 D	-0.316	0.084	1	0.02369	768.152	994.208	histone cluster 1 H1 family member d [Source:HGNC Symbol;Acc:HGNC:4717] cyoglobin [Source:HGNC Symbol;Acc:HGNC:16505]

ENSG000001880 37.11	CLCN1 HIST1H2A L	0.294 -0.323	0.081 0.089	0.000118 0.000012	2 0.02409	0.02409 0.02409	10.09 155.881	4.746 269.204	chloride voltage-gated channel 1 [Source:HGNC Symbol;Acc:HGNC:2019] histone cluster 1 H2A family member I [Source:HGNC Symbol;Acc:HGNC:4730]
ENSG000002769 03.1									
ENSG000001810 36.14	FCRL6 OSTM1-AS1	-0.33 -0.315	0.088 0.086	3 8	0.02556 0.02793	0.02556 0.02793	6.645 16.841	10.241 25.51	Fc receptor like 6 [Source:HGNC Symbol;Acc:HGNC:31910] OSTM1 antisense RNA 1 [Source:HGNC Symbol;Acc:HGNC:43666]
ENSG000002251 74.2									
ENSG000001217 64.11	HCRTTR1	0.33	0.088	0.000156	0.03061	0.03061	34.615	17.321	hypocretin receptor 1 [Source:HGNC Symbol;Acc:HGNC:484-8]
ENSG000002253 45.3	SNX18P3	0.305	0.082	4	0.03061	0.03061	747.415	537.852	sorting nexin 18 pseudogene 3 [Source:HGNC Symbol;Acc:HGNC:39611]
ENSG000001133 28.19	CCNG1	0.298	0.079	0.000157	8	0.03062	1898.389	1329.019	cyclin G1 [Source:HGNC Symbol;Acc:HGNC:1592]
ENSG000001003 51.16	GRAP2	-0.283	0.079	3	0.03073	0.03073	12.129	32.064	GRB2 related adaptor protein 2 [Source:HGNC Symbol;Acc:HGNC:4563]
ENSG000002584 51.1	AL1636366 .1	0.318	0.089	0.000161	0.03073	0.03073	51.749	49.979	novel transcript, antisense to RNASE4 and ANG
ENSG000000920 67.5	CEBPE	0.325	0.088	9	0.03283	0.03283	16.621	8.328	CCAAT enhancer binding protein epsilon [Source:HGNC Symbol;Acc:HGNC:1836]
ENSG000001471 38.2	GPR174 APOBEC3	-0.332	0.089	2	0.03557	0.03557	27.447	65.675	G protein-coupled receptor 174 [Source:HGNC Symbol;Acc:HGNC:30245] apolipoprotein B mRNA editing enzyme catalytic subunit 3C [Source:HGNC Symbol;Acc:HGNC:17353]
ENSG000002445 09.4	C	0.286	0.078	4	0.03745	0.03745	904.724	689.181	Fos proto-oncogene, AP-1 transcription factor subunit [Source:HGNC Symbol;Acc:HGNC:3796]
ENSG000001703 45.10	FOS	0.274	0.074	8	0.03749	0.03749	3262.704	2433.091	
ENSG000001738 46.13	PLK3	0.287	0.077	9	0.03749	0.03749	1396.728	1071.226	polo like kinase 3 [Source:HGNC Symbol;Acc:HGNC:2154]
ENSG000000424 45.14	RETSAT LINC0125	0.179	0.048	1	0.03762	0.03762	2456.439	2065.907	retinol saturase [Source:HGNC Symbol;Acc:HGNC:25991] long intergenic non-protein coding RNA 1252 [Source:HGNC Symbol;Acc:HGNC:27888]
ENSG000002471 57.7	HIST2H3 D	-0.32 -0.25	0.089 0.066	2 9	0.000253 0.000232	0.000253 0.000265	140.208 147.494	172.721	histone cluster 2 H3 family member d [Source:HGNC Symbol;Acc:HGNC:25311]
ENSG000001835 98.3									
ENSG000002141 02.7	WEE2	-0.307	0.086	1	0.04764	0.04764	7.308	14.839	WEE1 homolog 2 [Source:HGNC Symbol;Acc:HGNC:19684] long intergenic non-protein coding RNA 1122 [Source:HGNC Symbol;Acc:HGNC:49267]
ENSG000002337 23.9	LINC0112 AL031777	-0.317	0.087	2	0.04764	0.04764	77.646	109.545	
ENSG000002829 88.2		-0.31	0.089	3	0.04804	0.04804	354.507	587.194	novel protein

Supplementary Table S5: Over-Representation Analysis (ORA)

Significantly enriched pathways from the WikiPathways database (FDR < 0.05)

Meaning of BgRatio, M/N and GeneRatio k/M in the table
 - M = size of the gene-set (e.g. number of genes in the Genotoxicity pathway). More precisely, the total number of genes (ENTREZ Gene IDs) from the universe found in this gene-set.

- N = size of all unique genes in the collection of gene-sets (e.g. the WikiPathways collection). More precisely, the total number of genes (ENTREZ Gene IDs) from the universe found in this collection
- K = size of the overlap of significantly differentially expressed genes with a specific gene-set (e.g. Genotoxicity pathway). Only unique ENTREZ Gene IDs were considered.
- n = size of the overlap of significantly differentially expressed genes with all genes in the collection of gene-sets (e.g. the WikiPathways collection). Only unique ENTREZ Gene IDs were considered.
- The rich factor is K / M

ID	Description	Adjus							Gene symbols
		Gen eRat io	Bg Rat io	P- valu e	Q- valu e	p- valu e	Rich facto r	C ou nt	
WP174		19/	2.10	0.000	0.000	0.000	0.263		
2	TP53 Network	5/51	678	4E-07	0.043	0.055	1578	5	BAX/BBC3/GADD45A/CDKN1A/MDM2
WP428		15/5	63/678	1.35	9E-07	1.702	2.133	0.238	RRM2B/TP53I3/GADD45A/CDKN1A/TRIM22/DDB2/MDM2/PPM
6	Genotoxicity pathway	1	8	19	E-17	E-17	38	15	1D/PLK3/PHLDA3/AEN/SERTAD1/HIST1H2BM/HIST1H2BB/HI
WP398	miRNA regulation of p53 pathway in prostate cancer	6/51	678	8E-08	0.010	0.013	2222	6	BAX/BBC3/TNFRSF10B/DDB2/MDM2/ZMAT3
WP455	FBXL10 enhancement of MAP/ERK signaling in diffuse large B-cell lymphoma	3/51	8	0.08	92	69	22		HIST2H3D/HIST1H3J/HIST1H3G/HIST1H3H/HIST1H3B/HIST1
WP432	The effect of progerin on the involved genes in Hutchinson-Gilford Progeria Syndrome	6/51	37/678	2.58	0.000	0.000	0.162		HIST2H3D/HIST1H3J/HIST1H3G/HIST1H3H/HIST1H3B/HIST1
WP707	DNA Damage Response	9/51	8	0.09	1.28	5.363	6.721	3529	RRM2B/SESN1/BAX/BBC3/GADD45A/TNFRSF10B/CDKN1A/D
					E-08	E-08	41	9	DB2/MDM2

WP	miRNA Regulation of DNA Damage Response	10/5	79/1	2.21	0.126
0		8	678	1.385	5822
WP		67/1	10	E-08	RRM2B/SESN1/BAX/BBC3/CCNG1/GADD45A/TNFRSF10B/CD
236	Histone Modifications	678	5.44	0.000	10 KN1A/DDB2/MDM2
9		678	5E-0085	0.000	0.104
WP		7/51	8	0.07	4776 HIST2H3D/HIST1H3J/HIST1H3G/HIST1H4/HIST1H3H/HIST1H
468	Melanoma	678	0.00	26	7 3B/HIST1H3C
5		678	0.010	9	0.088
WP	Chromosomal and microsatellite instability in colorectal cancer	6/51	8	21	0.000 2352
421		73/	0.00	1421	94 BAX/GADD45A/CDKN1A/DDB2/MDM2/FOS
6		678	0.015	1781	0.082
WP	Endometrial cancer	6/51	8	43	0.000 1917
415		63/	0.00	1933	6 BAX/BBC3/GADD45A/CDKN1A/DDB2/FOS
5		678	0.099	2423	81 0.079
WP	Apoptosis	5/51	8	15	0.001 3650
254		84/	0.00	129	5 BAX/GADD45A/CDKN1A/DDB2/FOS
WP	Apoptosis Modulation and Signaling	5/51	8	154	415 79
177		678	0.036	0.001	0.059
2		90/	8	727	0.004 5238
WP	Breast cancer pathway	5/51	8	7	1 IGF1/BAX/BBC3/TNFRSF10B/MDM2
426		678	0.0532	0.004	0.055
2		0.00	3	445	5555
WP		678	0.007	571	5 BAX/BBC3/TNFRSF10B/FOS/TNFRSF10C
WP		0.00	0.00	0.038	0.038
236	Adipogenesis	6/51	88	130	9610 0.038
WP		67	0.00	506	39 IGF1/BAX/GADD45A/CDKN1A/DDB2/FOS
466	Hepatitis B infection	5/51	88	2767	13 4615
6		152	25	408	38 5 IGF1/OSM/GADD45A/CDKN1A/LIF
		/67	0.00	0.030	0.032
		5404	99	85	8947 37 5 BAX/MAP2K6/CDKN1A/DDB2/FOS

Zusammenfassung

Glioblastoma multiforme (GBM) ist der häufigste bösartige Hirntumor bei Erwachsenen. Unbehandelt liegt das mediane Überleben bei circa drei Monaten [13]. Mithilfe maximal möglicher Resektion des Tumors und anschließender aggressiver kombinierter Radiochemotherapie, bestehend aus Bestrahlung und dem Zytostatikum Temozolomid, wird das mediane Überleben auf circa 15 Monate nach Diagnosestellung angehoben [11,12]. Trotz intensiver Forschung ist über die Entstehung des GBMs wenig bekannt, der einzige bisher bestätigte prädisponierende Faktor ist eine Bestrahlung des Kopfes, insbesondere im Kindes- und Jugendalter [7].

Ein charakteristisches Merkmal des GBMs ist seine große Heterogenität sowohl innerhalb des Tumors eines Patienten als auch zwischen den Tumoren verschiedener Patienten. Dadurch werden die erfolgreiche Behandlung und eine mögliche Heilung erschwert, da sich bis heute nicht zuverlässig vorhersagen lässt, wie gut ein Patient von der Standardtherapie profitieren wird. Das infiltrative Wachstum von GBMs entlang von Nervenbahnen in der gesunden weißen Substanz oder mithilfe der Blutgefäße macht es nahezu unmöglich, die gesamte Tumormasse chirurgisch zu entfernen, was eine hohe Rezidivrate zur Folge hat [10,88]. Ein größeres Verständnis für die Entstehungsmechanismen des GBMs und seiner Therapieresistenzen ist essenziell für die Entwicklung besserer Therapiemöglichkeiten und verlangt dringend nach geeigneten Modellen für deren Erforschung.

In der Krebsforschung bedient man sich häufig an Zellkultur- oder Tiermodellen. Zellkulturen bieten den Vorteil, dass sie preisgünstig in der Unterhaltung sind und sich in relativ kurzer Zeit große Datenmengen durch einen hohen experimentellen Durchsatz erzielen lassen. Nachteilig ist, dass jeglicher Gewebeverband fehlt und das Modell daher nicht die reale Situation in einem ganzheitlichen Organismus widerspiegelt. Im Tiermodell ist der Organismus mitsamt verschiedenen Zelltypen, extrazellulärer Matrix und Blutkreislauf gegeben, jedoch gibt es mitunter gravierende Interspeziesunterschiede, die eine erfolgreiche klinische Translation der Ergebnisse aus Tierversuchen in das humane System erschweren. *Patient-derived xenografts*, also Transplantate aus Patientengewebe, machen sich den Organismus des Versuchstieres zunutze, erhalten aber dabei auch die Charakteristik des ursprünglichen Tumors weitgehend [76]. Um eine Abstoßung des transplantierten Tumorgewebes zu verhindern, werden zumeist immundefizierte Tiere verwendet, bei denen die immunologische Komponente fehlt, was das Modell artifiziell macht [77,78]. Zudem ist das erzeugte Tierleid ein nicht zu unterschätzender Faktor, denn Überlebenszeitanalysen mit dem Tod des Versuchstieres als Endpunkt, spielen eine wesentliche Rolle in der onkologischen Forschung. Um das Tierleid in wissenschaftlichen Experimenten zu verringern, wurde 1959 erstmals das 3R-Prinzip (*Reduction, Replacement, Refinement*)

definiert [79], wonach Tierversuche möglichst komplett ersetzt, Tierzahlen reduziert und die Bedingungen für Versuchstiere verbessert werden sollen. Diesem Prinzip folgend wurden im Institut für Anatomie der Universität Leipzig die organotypischen Schnittkulturen aus Patientengewebe als Alternative zum Tierversuch etabliert. Hierbei wird operativ entnommenes Tumorgewebe von Patienten mithilfe eines *Tissue Choppers* in 350 µm dünne Scheiben geschnitten und auf Membranen an einer Luft-Medium-Grenze kultiviert. Gewebe aus humanem GBM kann auf diese Weise bis zu zwei Wochen vital erhalten und für Versuche verwendet werden [83,84]. In der hier vorliegenden Promotionsarbeit wurden Schnittkulturen aus GBM-Gewebe von 25 Patienten angelegt und der Standardbehandlung aus Temozolomid und Bestrahlung unterzogen. Anschließend wurde das Gewebe histologisch aufgearbeitet, um einerseits die Qualität des Gewebeerhalts mittels klassischer Färbungen mit Hämatoxylin und Eosin beurteilen und um andererseits Marker für Proliferation (Ki67) und Apoptose (TUNEL-Assay) anfärbten und quantifizieren zu können. In der Vergangenheit beschränkte sich die Auswertung solcher Färbungen vorrangig auf die manuelle Quantifizierung, was zeitintensiv und abhängig von der durchführenden Person zu abweichenden Ergebnissen führt. Im Rahmen dieser Arbeit gelang die automatisierte quantitative Auswertung histologischer Färbungen von kultivierten Gewebeschnitten und deren Veröffentlichung [84]. Durch die Automatisierung kann die Analyse deutlich schneller erfolgen, ist objektiver und damit auch geeigneter für eine klinische Anwendung.

Zusätzlich zur histologischen Aufarbeitung des Gewebes wurde aus den Schnittkulturen RNA extrahiert, um Behandlungseffekte auf Expressionsebene untersuchen zu können. Für einen Patienten gelang der Vergleich zwischen Tumorgewebe und angrenzendem Tumorzugangsgewebe, da von beiden Gewebetypen Schnittkulturen angelegt und die Behandlung durchgeführt werden konnte. Mit einer Sequenziertiefe von bis zu 368 Millionen Reads pro Probe, wurden 1888 Gene identifiziert, die im Vergleich zum angrenzendem Gewebe im Tumorgewebe signifikant herunterreguliert waren [84]. Fast 2400 Gene waren entsprechend hochreguliert. Zwischen behandeltem und unbehandeltem Tumorgewebe gab es über 3400 Transkripte, die signifikant unterschiedlich exprimiert wurden. Die Signalweganalyse mit der IPA Software (Qiagen) ergab eine reduzierte Proliferation in behandeltem GBM-Gewebe, was sich mit den Befunden aus der Quantifizierung der Ki67-Färbung deckte. Eine Subgruppenanalyse ergab, dass Gewebekulturen von langzeitüberlebenden Patienten (Gesamtüberleben > 24 Monate) besser auf die Behandlung anzusprechen scheinen, was sich in einer signifikant erhöhten Apoptoserate im Vergleich zu Patienten mit kurzem Überleben zeigte. Schnittkulturen aus Patienten mit einem progressionsfreien Überleben (PFS) von mehr als 7 oder 12 Monaten zeigten eine signifikant höhere Proliferation als Patienten mit einem PFS von unter 7 Monaten [89]. Begründbar ist

das mit einer höheren Suszeptibilität von proliferierendem Gewebe gegenüber Schäden durch Bestrahlung und Zytostatika [90].

Die Expressionsanalyse aller 25 Patientenproben ergab eine Hochregulierung von 58 proteinkodierenden Genen. 32 Gene waren im Vergleich zu den unbehandelten Kontrollen im behandelten Gewebe herunterreguliert. Durch die funktionelle Analyse dieser differentiell exprimierten Gene konnte gezeigt werden, dass der p53-Signalweg, die Zellzykluskontrolle, sowie mit DNA-Schäden und deren Reparatur assoziierte Gene und Signalwege nach der Behandlung vermehrt aktiviert sind.

Insgesamt zeigen die Ergebnisse der vorliegenden Arbeit, dass Schnittkulturen aus GBM-Gewebe nicht nur histologisch aufgearbeitet werden können, sondern dass es zudem möglich ist, weitreichende molekulare Untersuchungen und Genexpressionsanalysen erfolgreich durchzuführen. Weiterhin sieht man eine gute Korrelation der aus den Kulturen gewonnenen Ergebnisse mit dem klinischen Verlauf der jeweiligen Patienten, was den Rückschluss zulässt, dass die Schnittkulturen ein gutes Abbild der tatsächlichen Situation im Patienten darstellen. Damit wird die Nutzbarkeit des Modells als Alternative zum Tierversuch weiter erhöht und klinisch interessant. Die Robustheit der Methode zeigt sich dadurch, dass RNA-Analysen aus den 25 Patienten umgesetzt werden konnten, obwohl es zum Teil gravierende Unterschiede in der Qualität des kultivierten Gewebes gab. Die inter- und intratumorale Heterogenität des GBMs stellt eine große Herausforderung dar, die mit der Verwendung von biologischen und technischen Replikaten adressiert wurden. Die Korrelationsanalyse der einzelnen Replikate zeigte, dass zumindest die intratumorale Heterogenität weitgehend ausgeglichen werden konnte. Die Heterogenität zwischen den einzelnen Patienten blieb jedoch erhalten und erschwerte allgemeine Aussagen und generelle Rückschlüsse. Auch im GBM besteht daher der dringende Bedarf an individualisierten und auf den einzelnen Patienten ausgerichteten Therapieansätzen. Hierfür bedarf es zukünftig weiterer Forschung an potenziellen Biomarkern mit größeren Patientenkohorten. Gewebekulturen können hierfür sowohl für die Untersuchung von Patientengewebe als auch für die Testung neuartiger Therapieansätze eine Rolle spielen.

Referenzen

1. Ostrom QT, Gittleman H, Xu J, Kromer C, Wolinsky Y, Kruchko C & Barnholtz-Sloan JS (2016) CBTRUS Statistical Report: Primary Brain and Other Central Nervous System Tumors Diagnosed in the United States in 2009-2013. *Neuro Oncol* 18, doi:10.1093/neuonc/now207.
2. Ostrom QT, Patil N, Cioffi G, Waite K, Kruchko C & Barnholtz-Sloan JS (2020) CBTRUS Statistical Report: Primary Brain and Other Central Nervous System Tumors Diagnosed in the United States in 2013-2017. *Neuro Oncol* 22, doi:10.1093/neuonc/noaa200.
3. Davis ME (2016) Glioblastoma: Overview of Disease and Treatment. *Clin J Oncol Nurs* 20, doi:10.1188/16.CJON.S1.2-8.
4. Kleihues P, Soylemezoglu F, Schäuble B, Scheithauer BW & Burger PC (1995) Histopathology, classification, and grading of gliomas. *Glia* 15, doi:10.1002/glia.440150303.
5. Louis DN, Perry A, Reifenberger G, Deimling A von, Figarella-Branger D, Cavenee WK, Ohgaki H, Wiestler OD, Kleihues P & Ellison DW (2016) The 2016 World Health Organization Classification of Tumors of the Central Nervous System: a summary. *Acta Neuropathol* 131, doi:10.1007/s00401-016-1545-1.
6. Wen PY & Kesari S (2008) Malignant gliomas in adults. *N Engl J Med* 359, doi:10.1056/NEJMra0708126.
7. Wrensch M, Fisher JL, Schwartzbaum JA, Bondy M, Berger M & Aldape KD (2005) The molecular epidemiology of gliomas in adults. *Neurosurg Focus* 19, doi:10.3171/foc.2005.19.5.6.
8. Louis DN, Ohgaki H, Wiestler OD, Cavenee WK, Burger PC, Jouvet A, Scheithauer BW & Kleihues P (2007) The 2007 WHO classification of tumours of the central nervous system. *Acta Neuropathol* 114, doi:10.1007/s00401-007-0243-4.
9. Wesseling P & Capper D (2018) WHO 2016 Classification of gliomas. *Neuropathol Appl Neurobiol* 44, doi:10.1111/nan.12432.
10. Weller M, Cloughesy T, Perry JR & Wick W (2013) Standards of care for treatment of recurrent glioblastoma--are we there yet? *Neuro Oncol* 15, doi:10.1093/neuonc/nos273.
11. Stupp R, Mason WP, van den Bent MJ, Weller M, Fisher B, Taphoorn MJB, Belanger K, Brandes AA, Marosi C, Bogdahn U, Curschmann J, Janzer RC, Ludwin SK, Gorlia T, Allgeier A, Lacombe D, Cairncross JG, Eisenhauer E & Mirimanoff RO (2005) Radiotherapy plus concomitant and adjuvant temozolomide for glioblastoma. *N Engl J Med* 352, doi:10.1056/nejmoa043330.
12. Stupp R, Hegi ME, Mason WP, van den Bent MJ, Taphoorn MJB, Janzer RC, Ludwin SK, Allgeier A, Fisher B, Belanger K, Hau P, Brandes AA, Gijtenbeek J, Marosi C, Vecht CJ, Mokhtari K, Wesseling P, Villa S, Eisenhauer E, Gorlia T, Weller M, Lacombe D, Cairncross JG & Mirimanoff R-O (2009) Effects of radiotherapy with concomitant and adjuvant temozolomide versus radiotherapy alone on survival in glioblastoma in a randomised phase III study: 5-year analysis of the EORTC-NCIC trial. *The Lancet Oncology* 10, doi:10.1016/S1470-2045(09)70025-7.
13. Malmström A, Grønberg BH, Marosi C, Stupp R, Frappaz D, Schultz H, Abacioglu U, Tavelin B, Lhermitte B, Hegi ME, Rosell J & Henriksson R (2012) Temozolomide versus standard 6-week radiotherapy versus hypofractionated radiotherapy in patients older than 60 years with glioblastoma: the Nordic randomised, phase 3 trial. *The Lancet Oncology* 13, doi:10.1016/S1470-2045(12)70265-6.
14. Ohgaki H & Kleihues P (2007) Genetic pathways to primary and secondary glioblastoma. *Am J Pathol* 170, doi:10.2353/ajpath.2007.070011.
15. Tso C-L, Freije WA, Day A, Chen Z, Merriman B, Perlina A, Lee Y, Dia EQ, Yoshimoto K, Mischel PS, Liau LM, Cloughesy TF & Nelson SF (2006) Distinct transcription profiles of primary and secondary glioblastoma subgroups. *Cancer Res* 66, doi:10.1158/0008-5472.CAN-05-0077.
16. Godard S, Getz G, Delorenzi M, Farmer P, Kobayashi H, Desbaillets I, Nozaki M, Diserens A-C, Hamou M-F, Dietrich P-Y, Regli L, Janzer RC, Bucher P, Stupp R, Tribolet N de, Domany E & Hegi ME (2003) Classification of human astrocytic gliomas on the basis of gene expression: a correlated group of genes with angiogenic activity emerges as a strong predictor of subtypes. *Cancer Res* 63,
17. Ohgaki H & Kleihues P (2013) The definition of primary and secondary glioblastoma. *Clin Cancer Res* 19, doi:10.1158/1078-0432.CCR-12-3002.
18. Yan H, Parsons DW, Jin G, McLendon R, Rasheed BA, Yuan W, Kos I, Batinic-Haberle I, Jones S, Riggins GJ, Friedman H, Friedman A, Reardon D, Herndon J, Kinzler KW, Velculescu VE,

- Vogelstein B & Bigner DD (2009) IDH1 and IDH2 mutations in gliomas. *N Engl J Med* 360, doi:10.1056/NEJMoa0808710.
19. Siegal T (2015) Clinical impact of molecular biomarkers in gliomas. *J Clin Neurosci* 22, doi:10.1016/j.jocn.2014.10.004.
 20. Weller M, Wick W & Deimling A von (2011) Isocitrate dehydrogenase mutations: a challenge to traditional views on the genesis and malignant progression of gliomas. *Glia* 59, doi:10.1002/glia.21130.
 21. Cheng H-B, Yue W, Xie C, Zhang R-Y, Hu S-S & Wang Z (2013) IDH1 mutation is associated with improved overall survival in patients with glioblastoma: a meta-analysis. *Tumour Biol* 34, doi:10.1007/s13277-013-0934-5.
 22. Brat DJ, Aldape K, Colman H, Figrarella-Branger D, Fuller GN, Giannini C, Holland EC, Jenkins RB, Kleinschmidt-DeMasters B, Komori T, Kros JM, Louis DN, McLean C, Perry A, Reifenberger G, Sarkar C, Stupp R, van den Bent MJ, Deimling A von & Weller M (2020) cIMPACT-NOW update 5: recommended grading criteria and terminologies for IDH-mutant astrocytomas. *Acta Neuropathol* 139, doi:10.1007/s00401-020-02127-9.
 23. Weller M, van den Bent M, Hopkins K, Tonn JC, Stupp R, Falini A, Cohen-Jonathan-Moyal E, Frappaz D, Henriksson R, Balana C, Chinot O, Ram Z, Reifenberger G, Soffietti R & Wick W (2014) EANO guideline for the diagnosis and treatment of anaplastic gliomas and glioblastoma. *The Lancet Oncology* 15, doi:10.1016/S1470-2045(14)70011-7.
 24. Stummer W, Pichlmeier U, Meinel T, Wiestler OD, Zanella F & Reulen H-J (2006) Fluorescence-guided surgery with 5-aminolevulinic acid for resection of malignant glioma: a randomised controlled multicentre phase III trial. *The Lancet Oncology* 7, doi:10.1016/S1470-2045(06)70665-9.
 25. Schucht P, Knittel S, Slotboom J, Seidel K, Murek M, Jilch A, Raabe A & Beck J (2014) 5-ALA complete resections go beyond MR contrast enhancement: shift corrected volumetric analysis of the extent of resection in surgery for glioblastoma. *Acta Neurochir (Wien)* 156, doi:10.1007/s00701-013-1906-7.
 26. Weller M, van den Bent M, Preusser M, Le Rhun E, Tonn JC, Minniti G, Bendszus M, Balana C, Chinot O, Dirven L, French P, Hegi ME, Jakola AS, Platten M, Roth P, Rudà R, Short S, Smits M, Taphoorn MJB, Deimling A von, Westphal M, Soffietti R, Reifenberger G & Wick W (2021) EANO guidelines on the diagnosis and treatment of diffuse gliomas of adulthood. *Nat Rev Clin Oncol* 18, doi:10.1038/s41571-020-00447-z.
 27. Stupp R, Taillibert S, Kanner A, Read W, Steinberg D, Lhermitte B, Toms S, Idbaih A, Ahluwalia MS, Fink K, Di Meco F, Lieberman F, Zhu J-J, Stragliotto G, Tran D, Brem S, Hottinger A, Kirson ED, Levy-Shahaf G, Weinberg U, Kim C-Y, Paek S-H, Nicholas G, Bruna J, Hirte H, Weller M, Palti Y, Hegi ME & Ram Z (2017) Effect of Tumor-Treating Fields Plus Maintenance Temozolomide vs Maintenance Temozolomide Alone on Survival in Patients With Glioblastoma: A Randomized Clinical Trial. *JAMA* 318, doi:10.1001/jama.2017.18718.
 28. Zhang J, Stevens MFG & Bradshaw TD (2012) Temozolomide: mechanisms of action, repair and resistance. *Curr Mol Pharmacol* 5, doi:10.2174/1874467211205010102.
 29. Weller M, Pfister SM, Wick W, Hegi ME, Reifenberger G & Stupp R (2013) Molecular neuro-oncology in clinical practice: a new horizon. *The Lancet Oncology* 14, doi:10.1016/S1470-2045(13)70168-2.
 30. Smrdel U, Popovic M, Zwitter M, Bostjancic E, Zupan A, Kovac V, Glavac D, Bokal D & Jerebic J (2016) Long-term survival in glioblastoma: methyl guanine methyl transferase (MGMT) promoter methylation as independent favourable prognostic factor. *Radiol Oncol* 50, doi:10.1515/raon-2015-0041.
 31. Wick W, Platten M, Meissner C, Felsberg J, Tabatabai G, Simon M, Nikkhah G, Papsdorf K, Steinbach JP, Sabel M, Combs SE, Vesper J, Braun C, Meixensberger J, Ketter R, Mayer-Steinacker R, Reifenberger G & Weller M (2012) Temozolomide chemotherapy alone versus radiotherapy alone for malignant astrocytoma in the elderly: the NOA-08 randomised, phase 3 trial. *The Lancet Oncology* 13, doi:10.1016/S1470-2045(12)70164-X.
 32. Perry JR, Laperriere N, O'Callaghan CJ, Brandes AA, Menten J, Phillips C, Fay M, Nishikawa R, Cairncross JG, Roa W, Osoba D, Rossiter JP, Sahgal A, Hirte H, Laigle-Donadey F, Franceschi E, Chinot O, Golfinopoulos V, Fariselli L, Wick A, Feuvret L, Back M, Tills M, Winch C, Baumert BG, Wick W, Ding K & Mason WP (2017) Short-Course Radiation plus Temozolomide in Elderly Patients with Glioblastoma. *N Engl J Med* 376, doi:10.1056/NEJMoa1611977.

33. Wick, W. & et al. Gliome, S2k-Leitlinie, 2021. Leitlinien für Diagnostik und Therapie in der Neurologie. Available at www.dgn.org/leitlinien/ (2021).
34. Razavi S-M, Lee KE, Jin BE, Aujla PS, Gholamin S & Li G (2016) Immune Evasion Strategies of Glioblastoma. *Front Surg* 3, doi:10.3389/fsurg.2016.00011.
35. Duncan DS & Miller SD (2011) CNS expression of B7-H1 regulates pro-inflammatory cytokine production and alters severity of Theiler's virus-induced demyelinating disease. *PLoS One* 6, doi:10.1371/journal.pone.0018548.
36. Freeman GJ, Long AJ, Iwai Y, Bourque K, Chernova T, Nishimura H, Fitz LJ, Malenkovich N, Okazaki T, Byrne MC, Horton HF, Fouser L, Carter L, Ling V, Bowman MR, Carreno BM, Collins M, Wood CR & Honjo T (2000) Engagement of the PD-1 immunoinhibitory receptor by a novel B7 family member leads to negative regulation of lymphocyte activation. *J Exp Med* 192, doi:10.1084/jem.192.7.1027.
37. Wang H, Xiao Y, Ren X & Wan D (2021) Prognostic value of programmed death ligand 1 (PD-L1) in glioblastoma: a systematic review, meta-analysis and validation based on dataset. *Bioengineered* 12, doi:10.1080/21655979.2021.1996515.
38. Wintterle S, Schreiner B, Mitsdoerffer M, Schneider D, Chen L, Meyermann R, Weller M & Wiendl H (2003) Expression of the B7-related molecule B7-H1 by glioma cells: a potential mechanism of immune paralysis. *Cancer Res* 63,
39. Zeng J, See AP, Phallen J, Jackson CM, Belcaid Z, Ruzevick J, Durham N, Meyer C, Harris TJ, Albesiano E, Pradilla G, Ford E, Wong J, Hammers H-J, Mathios D, Tyler B, Brem H, Tran PT, Pardoll D, Drake CG & Lim M (2013) Anti-PD-1 blockade and stereotactic radiation produce long-term survival in mice with intracranial gliomas. *Int J Radiat Oncol Biol Phys* 86, doi:10.1016/j.ijrobp.2012.12.025.
40. Johnson DB, Peng C & Sosman JA (2015) Nivolumab in melanoma: latest evidence and clinical potential. *Ther Adv Med Oncol* 7, doi:10.1177/1758834014567469.
41. Daher S, Lawrence YR, Dudnik E, Hanovich E, Urban D, Peled N, Navon R, Leibowitz R, Hammerman A, Battat E, Gottfried T, Onn A & Bar J (2021) Nivolumab in Non-Small Cell Lung Cancer: Real World Long-Term Survival Results and Blood-Based Efficacy Biomarkers. *Front Oncol* 11, doi:10.3389/fonc.2021.625668.
42. Larkin J, Chiarion-Sileni V, Gonzalez R, Grob J-J, Rutkowski P, Lao CD, Cowey CL, Schadendorf D, Wagstaff J, Dummer R, Ferrucci PF, Smylie M, Hogg D, Hill A, Márquez-Rodas I, Haanen J, Guidoboni M, Maio M, Schöffski P, Carlino MS, Lebbé C, McArthur G, Ascierto PA, Daniels GA, Long GV, Bastholt L, Rizzo JI, Balogh A, Moshyk A, Hodi FS & Wolchok JD (2019) Five-Year Survival with Combined Nivolumab and Ipilimumab in Advanced Melanoma. *N Engl J Med* 381, doi:10.1056/NEJMoa1910836.
43. Motzer RJ, Rini BI, McDermott DF, Arén Frontera O, Hammers HJ, Carducci MA, Salman P, Escudier B, Beuselinck B, Amin A, Porta C, George S, Neiman V, Bracarda S, Tykodi SS, Barthélémy P, Leibowitz-Amit R, Plimack ER, Oosting SF, Redman B, Melichar B, Powles T, Nathan P, Oudard S, Pook D, Choueiri TK, Donskov F, Grimm M-O, Gurney H, Heng DYC, Kollmannsberger CK, Harrison MR, Tomita Y, Duran I, Grünwald V, McHenry MB, Mekan S & Tannir NM (2019) Nivolumab plus ipilimumab versus sunitinib in first-line treatment for advanced renal cell carcinoma: extended follow-up of efficacy and safety results from a randomised, controlled, phase 3 trial. *The Lancet Oncology* 20, doi:10.1016/S1470-2045(19)30413-9.
44. Filley AC, Henriquez M & Dey M (2017) Recurrent glioma clinical trial, CheckMate-143: the game is not over yet. *Oncotarget* 8, doi:10.18632/oncotarget.21586.
45. Omuro A, Vlahovic G, Lim M, Sahebjam S, Baehring J, Cloughesy T, Voloschin A, Ramkisson SH, Ligon KL, Latek R, Zwirter R, Strauss L, Paliwal P, Harbison CT, Reardon DA & Sampson JH (2018) Nivolumab with or without ipilimumab in patients with recurrent glioblastoma: results from exploratory phase I cohorts of CheckMate 143. *Neuro Oncol* 20, doi:10.1093/neuonc/nox208.
46. Schalper KA, Rodriguez-Ruiz ME, Diez-Valle R, López-Janeiro A, Porciuncula A, Idoate MA, Inogés S, Andrea C de, López-Díaz de Cerio A, Tejada S, Berraondo P, Villarroel-Espindola F, Choi J, Gúrpide A, Giraldez M, Goicoechea I, Gallego Perez-Larraya J, Sanmamed MF, Perez-Gracia JL & Melero I (2019) Neoadjuvant nivolumab modifies the tumor immune microenvironment in resectable glioblastoma. *Nat Med* 25, doi:10.1038/s41591-018-0339-5.
47. Parker NR, Khong P, Parkinson JF, Howell VM & Wheeler HR (2015) Molecular heterogeneity in glioblastoma: potential clinical implications. *Front Oncol* 5, doi:10.3389/fonc.2015.00055.

48. Nowell PC (1976) The clonal evolution of tumor cell populations. *Science* 194, doi:10.1126/science.959840.
49. Gerlinger M & Swanton C (2010) How Darwinian models inform therapeutic failure initiated by clonal heterogeneity in cancer medicine. *Br J Cancer* 103, doi:10.1038/sj.bjc.6605912.
50. Sprouffske K, Merlo LMF, Gerrish PJ, Maley CC & Sniegowski PD (2012) Cancer in light of experimental evolution. *Curr Biol* 22, doi:10.1016/j.cub.2012.06.065.
51. Reya T, Morrison SJ, Clarke MF & Weissman IL (2001) Stem cells, cancer, and cancer stem cells. *Nature* 414, doi:10.1038/35102167.
52. Cheshier SH, Kalani MYS, Lim M, Ailles L, Huhn SL & Weissman IL (2009) A neurosurgeon's guide to stem cells, cancer stem cells, and brain tumor stem cells. *Neurosurgery* 65, doi:10.1227/01.NEU.0000349921.14519.2A.
53. Meyer M, Reimand J, Lan X, Head R, Zhu X, Kushida M, Bayani J, Pressey JC, Lionel AC, Clarke ID, Cusimano M, Squire JA, Scherer SW, Bernstein M, Woodin MA, Bader GD & Dirks PB (2015) Single cell-derived clonal analysis of human glioblastoma links functional and genomic heterogeneity. *Proc Natl Acad Sci U S A* 112, doi:10.1073/pnas.1320611111.
54. Phillips HS, Kharbanda S, Chen R, Forrest WF, Soriano RH, Wu TD, Misra A, Nigro JM, Colman H, Soroceanu L, Williams PM, Modrusan Z, Feuerstein BG & Aldape K (2006) Molecular subclasses of high-grade glioma predict prognosis, delineate a pattern of disease progression, and resemble stages in neurogenesis. *Cancer Cell* 9, doi:10.1016/j.ccr.2006.02.019.
55. Verhaak RGW, Hoadley KA, Purdom E, Wang V, Qi Y, Wilkerson MD, Miller CR, Ding L, Golub T, Mesirov JP, Alexe G, Lawrence M, O'Kelly M, Tamayo P, Weir BA, Gabriel S, Winckler W, Gupta S, Jakkula L, Feiler HS, Hodgson JG, James CD, Sarkaria JN, Brennan C, Kahn A, Spellman PT, Wilson RK, Speed TP, Gray JW, Meyerson M, Getz G, Perou CM & Hayes DN (2010) Integrated genomic analysis identifies clinically relevant subtypes of glioblastoma characterized by abnormalities in PDGFRA, IDH1, EGFR, and NF1. *Cancer Cell* 17, doi:10.1016/j.ccr.2009.12.020.
56. Wang Q, Hu B, Hu X, Kim H, Squatrito M, Scarpace L, deCarvalho AC, Lyu S, Li P, Li Y, Barthel F, Cho HJ, Lin Y-H, Satani N, Martinez-Ledesma E, Zheng S, Chang E, Sauvé C-EG, Olar A, Lan ZD, Finocchiaro G, Phillips JJ, Berger MS, Gabrusiewicz KR, Wang G, Eskilsson E, Hu J, Mikkelsen T, DePinho RA, Muller F, Heimberger AB, Sulman EP, Nam D-H & Verhaak RGW (2017) Tumor Evolution of Glioma-Intrinsic Gene Expression Subtypes Associates with Immunological Changes in the Microenvironment. *Cancer Cell* 32, doi:10.1016/j.ccr.2017.06.003.
57. Weller M, Knobbe-Thomsen CB, Le Rhun E & Reifenberger G (2022) Die WHO-Klassifikation der Tumoren des zentralen Nervensystems 2021. *Onkologe* 28, doi:10.1007/s00761-021-01083-7.
58. Bhat KPL, Balasubramanyan V, Vaillant B, Ezhilarasan R, Hummelink K, Hollingsworth F, Wani K, Heathcock L, James JD, Goodman LD, Conroy S, Long L, Lelic N, Wang S, Gumin J, Raj D, Kodama Y, Raghunathan A, Olar A, Joshi K, Pelloski CE, Heimberger A, Kim SH, Cahill DP, Rao G, Dunnen WFA den, Boddeke HWGM, Phillips HS, Nakano I, Lang FF, Colman H, Sulman EP & Aldape K (2013) Mesenchymal differentiation mediated by NF-κB promotes radiation resistance in glioblastoma. *Cancer Cell* 24, doi:10.1016/j.ccr.2013.08.001.
59. Wolf J (2020) „Wir sind es den Patienten schuldig, medizinische Innovationen umzusetzen“. *Frankfurter Allgemeine Zeitung*,
60. Alamgeer M, Ganju V & Watkins DN (2013) Novel therapeutic targets in non-small cell lung cancer. *Curr Opin Pharmacol* 13, doi:10.1016/j.coph.2013.03.010.
61. Savas P, Hughes B & Solomon B (2013) Targeted therapy in lung cancer: IPASS and beyond, keeping abreast of the explosion of targeted therapies for lung cancer. *J Thorac Dis* 5 Suppl 5, doi:10.3978/j.issn.2072-1439.2013.08.52.
62. Non-small Cell Lung Cancer Targeted Drug Therapy | Lung Cancer Drugs. Available at <https://www.cancer.org/cancer/lung-cancer/treating-non-small-cell/targeted-therapies.html> (2022).
63. Shepherd FA, Rodrigues Pereira J, Ciuleanu T, Tan EH, Hirsh V, Thongprasert S, Campos D, Maoleekoonpiroj S, Smylie M, Martins R, van Kooten M, Dediu M, Findlay B, Tu D, Johnston D, Bezzjak A, Clark G, Santabarbara P & Seymour L (2005) Erlotinib in previously treated non-small-cell lung cancer. *N Engl J Med* 353, doi:10.1056/NEJMoa050753.
64. Bezzjak A, Tu D, Seymour L, Clark G, Trajkovic A, Zukin M, Ayoub J, Lago S, Albuquerque Ribeiro R de, Gerogianni A, Cyron A, Noble J, Laberge F, Chan RT-T, Fenton D, Pawel J von, Reck M & Shepherd FA (2006) Symptom improvement in lung cancer patients treated with erlotinib: quality

- of life analysis of the National Cancer Institute of Canada Clinical Trials Group Study BR.21. *J Clin Oncol* 24, doi:10.1200/JCO.2006.05.8073.
65. Solomon BJ, Mok T, Kim D-W, Wu Y-L, Nakagawa K, Mekhail T, Felip E, Cappuzzo F, Paolini J, Usari T, Iyer S, Reisman A, Wilner KD, Tursi J & Blackhall F (2014) First-line crizotinib versus chemotherapy in ALK-positive lung cancer. *N Engl J Med* 371, doi:10.1056/NEJMoa1408440.
 66. Gilbert MR, Dignam JJ, Armstrong TS, Wefel JS, Blumenthal DT, Vogelbaum MA, Colman H, Chakravarti A, Pugh S, Won M, Jeraj R, Brown PD, Jaeckle KA, Schiff D, Stieber VW, Brachman DG, Werner-Wasik M, Tremont-Lukats IW, Sulman EP, Aldape KD, Curran WJ & Mehta MP (2014) A randomized trial of bevacizumab for newly diagnosed glioblastoma. *N Engl J Med* 370, doi:10.1056/NEJMoa1308573.
 67. Weller M, Butowski N, Tran DD, Recht LD, Lim M, Hirte H, Ashby L, Mechtler L, Goldlust SA, Iwamoto F, Drappatz J, O'Rourke DM, Wong M, Hamilton MG, Finocchiaro G, Perry J, Wick W, Green J, He Y, Turner CD, Yellin MJ, Keler T, Davis TA, Stupp R, Sampson JH, Campian J, Recht L, Goldlust S, Becker K, Barnett G, Nicholas G, Desjardins A, Benkers T, Wagle N, Groves M, Kesari S, Horvath Z, Merrell R, Curry R, O'Rourke J, Schuster D, Mrugala M, Jensen R, Trusheim J, Lesser G, Belanger K, Sloan A, Purow B, Fink K, Raizer J, Schulder M, Nair S, Peak S, Brandes A, Mohile N, Landolfi J, Olson J, Jennens R, DeSouza P, Robinson B, Crittenden M, Shih K, Flowers A, Ong S, Connelly J, Hadjipanayis C, Giglio P, Mott F, Mathieu D, Lessard N, Sepulveda SJ, Lövey J, Wheeler H, Inglis P-L, Hardie C, Bota D, Lesniak M, Portnow J, Frankel B, Junck L, Thompson R, Berk L, McGhie J, Macdonald D, Saran F, Soffietti R, Blumenthal D, André de SBCM, Nowak A, Singhal N, Hottinger A, Schmid A, Srkalovic G, Baskin D, Fadul C, Nabors L, LaRocca R, Villano J, Paleologos N, Kavan P, Pitz M, Thiessen B, Idbaih A, Frenel JS, Domont J, Grauer O, Hau P, Marosi C, Sroubek J, Hovey E, Sridhar PS, Cher L, Dunbar E, Coyle T, Raymond J, Barton K, Guarino M, Raval S, Stea B, Dietrich J, Hopkins K, Erridge S, Steinbach J-P, Pineda LE, Balana QC, Sonia del BB, Wenczl M, Molnár K, Hideghéty K, Lossos A, Myra van L, Levy A, Harrup R, Patterson W, Lwin Z, Sathornsumetee S, Lee E-J, Ho J-T, Emmons S, Duic JP, Shao S, Ashamalla H, Weaver M, Lutzky J, Avgeropoulos N, Hanna W, Nadipuram M, Cecchi G, O'Donnell R, Pannullo S, Carney J, Hamilton M, MacNeil M, Beaney R, Fabbro M, Schnell O, Fietkau R, Stockhammer G, Malinova B, Odrazka K, Sames M, Miguel Gil G, Razis E, Lavrenkov K, Castro G, Ramirez F, Baldotto C, Viola F, Malheiros S, Lickliter J, Gauden S, Dechaphunkul A, Thaipisuttikul I, Thotathil Z, Ma H-I, Cheng W-Y, Chang C-H, Salas F, Dietrich P-Y, Mamot C, Nayak L & Nag S (2017) Rindopepimut with temozolomide for patients with newly diagnosed, EGFRvIII-expressing glioblastoma (ACT IV): a randomised, double-blind, international phase 3 trial. *The Lancet Oncology* 18, doi:10.1016/S1470-2045(17)30517-X.
 68. Wick W, Dettmer S, Berberich A, Kessler T, Karapanagiotou-Schenkel I, Wick A, Winkler F, Pfaff E, Brors B, Debus J, Unterberg A, Bendszus M, Herold-Mende C, Eisenmenger A, Deimling A von, Jones DTW, Pfister SM, Sahm F & Platten M (2019) N2M2 (NOA-20) phase I/II trial of molecularly matched targeted therapies plus radiotherapy in patients with newly diagnosed non-MGMT hypermethylated glioblastoma. *Neuro Oncol* 21, doi:10.1093/neuonc/noy161.
 69. Wang Z, Gerstein M & Snyder M (2009) RNA-Seq: a revolutionary tool for transcriptomics. *Nat Rev Genet* 10, doi:10.1038/nrg2484.
 70. Ju J, Kim DH, Bi L, Meng Q, Bai X, Li Z, Li X, Marma MS, Shi S, Wu J, Edwards JR, Romu A & Turro NJ (2006) Four-color DNA sequencing by synthesis using cleavable fluorescent nucleotide reversible terminators. *Proc Natl Acad Sci U S A* 103, doi:10.1073/pnas.0609513103.
 71. Perez-Garcia A, Carrion-Navarro J, Bosch-Forteá M, Lazaro-Ibanez E, Prat-Acin R & Ayuso-Sacido A (2012) Genomic instability of surgical sample and cancer-initiating cell lines from human glioblastoma. *Front Biosci (Landmark Ed)* 17, doi:10.2741/3998.
 72. Schneider CK, Kalinke U & Löwer J (2006) TGN1412--a regulator's perspective. *Nat Biotechnol* 24, doi:10.1038/nbt0506-493.
 73. Dowsing T & Kendall MJ (2007) The Northwick Park tragedy--protecting healthy volunteers in future first-in-man trials. *J Clin Pharm Ther* 32, doi:10.1111/j.1365-2710.2007.00808.x.
 74. Tisoncik JR, Korth MJ, Simmons CP, Farrar J, Martin TR & Katze MG (2012) Into the eye of the cytokine storm. *Microbiol Mol Biol Rev* 76, doi:10.1128/MMBR.05015-11.
 75. Pallardy M & Hünig T (2010) Primate testing of TGN1412: right target, wrong cell. *Br J Pharmacol* 161, doi:10.1111/j.1476-5381.2010.00925.x.
 76. Hidalgo M, Amant F, Biankin AV, Budinská E, Byrne AT, Caldas C, Clarke RB, Jong S de, Jonkers J, Mælandsmo GM, Roman-Roman S, Seoane J, Trusolino L & Villanueva A (2014)

- Patient-derived xenograft models: an emerging platform for translational cancer research. *Cancer Discov* 4, doi:10.1158/2159-8290.CD-14-0001.
77. Flanagan SP (1966) 'Nude', a new hairless gene with pleiotropic effects in the mouse. *Genet Res* 8, doi:10.1017/s0016672300010168.
 78. Bosma GC, Custer RP & Bosma MJ (1983) A severe combined immunodeficiency mutation in the mouse. *Nature* 301, doi:10.1038/301527a0.
 79. Russell WMS & Burch RL. The principles of humane experimental technique. 1959th ed. (Universities Federation for Animal Welfare, 1992).
 80. Stoppini L, Buchs P-A & Muller D (1991) A simple method for organotypic cultures of nervous tissue. *Journal of Neuroscience Methods* 37, doi:10.1016/0165-0270(91)90128-m.
 81. Kluge A, Hailer NP, Horvath TL, Bechmann I & Nitsch R (1998) Tracing of the entorhinal-hippocampal pathway in vitro. *Hippocampus* 8, doi:10.1002/(SICI)1098-1063(1998)8:1<57::AID-HIPO6>3.0.CO;2-4.
 82. Eyüpoglu IY, Bechmann I & Nitsch R (2003) Modification of microglia function protects from lesion-induced neuronal alterations and promotes sprouting in the hippocampus. *FASEB J* 17, doi:10.1096/fj.02-0825fje.
 83. Merz F, Gaunitz F, Dehghani F, Renner C, Meixensberger J, Gutenberg A, Giese A, Schopow K, Hellwig C, Schäfer M, Bauer M, Stöcker H, Taucher-Scholz G, Durante M & Bechmann I (2013) Organotypic slice cultures of human glioblastoma reveal different susceptibilities to treatments. *Neuro Oncol* 15, doi:10.1093/neuonc/not003.
 84. Haehnel S, Reiche K, Loeffler D, Horn A, Blumert C, Puppel S-H, Kaiser N, Rapp F, Rade M, Horn F, Meixensberger J, Bechmann I, Gaunitz F & Winter K (2019) Deep sequencing and automated histochemistry of human tissue slice cultures improve their usability as preclinical model for cancer research. *Sci Rep* 9, doi:10.1038/s41598-019-56509-5.
 85. Gerlach MM, Merz F, Wichmann G, Kubick C, Wittekind C, Lordick F, Dietz A & Bechmann I (2014) Slice cultures from head and neck squamous cell carcinoma: a novel test system for drug susceptibility and mechanisms of resistance. *Br J Cancer* 110, doi:10.1038/bjc.2013.700.
 86. Sönnichsen R, Hennig L, Blaschke V, Winter K, Körfer J, Hähnle S, Monecke A, Wittekind C, Jansen-Winkel B, Thieme R, Gockel I, Grosser K, Weimann A, Kubick C, Wiechmann V, Aigner A, Bechmann I, Lordick F & Kallendrusch S (2018) Individual Susceptibility Analysis Using Patient-derived Slice Cultures of Colorectal Carcinoma. *Clin Colorectal Cancer* 17, doi:10.1016/j.clcc.2017.11.002.
 87. Koerfer J, Kallendrusch S, Merz F, Wittekind C, Kubick C, Kassahun WT, Schumacher G, Moebius C, Gaßler N, Schopow N, Geister D, Wiechmann V, Weimann A, Eckmann C, Aigner A, Bechmann I & Lordick F (2016) Organotypic slice cultures of human gastric and esophagogastric junction cancer. *Cancer Med* 5, doi:10.1002/cam4.720.
 88. Cuddapah VA, Robel S, Watkins S & Sontheimer H (2014) A neurocentric perspective on glioma invasion. *Nat Rev Neurosci* 15, doi:10.1038/nrn3765.
 89. Haehnel S, Rade M, Kaiser N, Reiche K, Horn A, Loeffler D, Blumert C, Rapp F, Horn F, Meixensberger J, Renner C, Mueller W, Gaunitz F, Bechmann I & Winter K (2022) RNA sequencing of glioblastoma tissue slice cultures reveals the effects of treatment at the transcriptional level. *FEBS Open Bio* 12, doi:10.1002/2211-5463.13353.
 90. Mendonca MS, Rodriguez A & Alpen EL (1989) Quiescence in 9L Cells and Correlation with Radiosensitivity and PLD Repair. *Radiation Research* 117, doi:10.2307/3577349.

Darstellung des eigenen Beitrags

Hiermit erkläre ich, dass die unten genannte Darstellung des eigenen Beitrags an der vorliegenden Arbeit der Wahrheit entspricht.

Publikation: Deep sequencing and automated histochemistry of human tissue slice cultures improve their usability as preclinical model for cancer research.

Susann Haehnel, Kristin Reiche, Dennis Loeffler, Andreas Horn, Conny Blumert, Sven-Holger Poppel, Nicole Kaiser, Felicitas Rapp, Michael Rade, Friedemann Horn, Juergen Meixensberger, Ingo Bechmann, Frank Gaunitz & Karsten Winter.

Scientific Reports. 2019.

Eigener Beitrag:

- Mitkonzipierung und Durchführung der Experimente
- Aufbereitung des humanen Gewebes und Kultivierung der Schnittkulturen
- Behandlung des Gewebes mit Cytostatika und Bestrahlung
- RNA- und Proteinisolation, histologische Färbungen, RNA-Sequenzierung
- Aufnahme und Auswertung der histologischen Färbungen
- Analyse und Interpretation der Daten
- Erstellung der Abbildungen
- Anfertigung des Manuskripts

Folgende Personen bestätigen die Richtigkeit meiner Darstellung des eigenen Beitrags:

Seniorautor:


Dr. Karsten Winter

Ko-Seniorautor:


Prof. Dr. Frank Gaunitz

Ko-Autor:


Prof. Dr. Ingo Bechmann

Ko-Autor:


Dr. Nicole Kaiser

Ko-Autor:


Andreas Horn

Ko-Autor:


Dr. Kristin Reiche

Ko-Autor:


Michael Rade

Ko-Autor:


Dr. Dennis Löffler

Leipzig, 06.05.22

Ort, Datum



Unterschrift

Publikation: Benefit and limitations of glioblastoma tissue slice cultures – an RNA sequencing study

Susann Haehnel, Michael Rade, Nicole Kaiser, Kristin Reiche, Andreas Horn, Dennis Loeffler, Conny Blumert, Felicitas Rapp, Friedemann Horn, Juergen Meixensberger, Christof Renner, Wolf Mueller, Frank Gaunitz, Ingo Bechmann, and Karsten Winter

FEBS Open Bio. 2021.

Eigener Beitrag:

- Mitkonzipierung und Durchführung der Experimente
- Aufbereitung des humanen Gewebes und Kultivierung der Schnittkulturen
- Behandlung des Gewebes mit Cytostatika und Bestrahlung
- RNA- und Proteinisolierung, histologische Färbungen, RNA-Sequenzierung
- Aufnahme und Auswertung der histologischen Färbungen
- Monitoring des klinischen Verlaufs der 25 Patienten
- Analyse und Interpretation der Daten
- Erstellung der Abbildungen
- Anfertigung des Manuskripts

Folgende Personen bestätigen die Richtigkeit meiner Darstellung des eigenen Beitrags:

Seniorautor:



Dr. Karsten Winter

Ko-Autor:



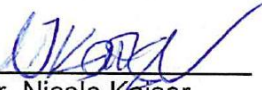
Prof. Dr. Frank Gaunitz

Ko-Autor:



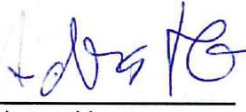
Prof. Dr. Ingo Bechmann

Ko-Autor:



Dr. Nicole Kaiser

Ko-Autor:



Andreas Horn

Ko-Autor:



Dr. Kristin Reiche

Ko-Autor:



Michael Rade

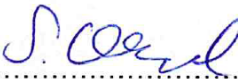
Ko-Autor:



Dr. Dennis Löffler

Leipzig, 06.05.22

Ort, Datum



S. Oerel

Unterschrift

Erklärung über die eigenständige Abfassung der Arbeit

Hiermit erkläre ich, dass ich die vorliegende Arbeit selbstständig und ohne unzulässige Hilfe oder Benutzung anderer als der angegebenen Hilfsmittel angefertigt habe. Ich versichere, dass Dritte von mir weder unmittelbar noch mittelbar eine Vergütung oder geldwerte Leistungen für Arbeiten erhalten haben, die im Zusammenhang mit dem Inhalt der vorgelegten Dissertation stehen und dass die vorgelegte Arbeit weder im Inland noch im Ausland in gleicher oder ähnlicher Form einer anderen Prüfungsbehörde zum Zweck einer Promotion oder eines anderen Prüfungsverfahrens vorgelegt wurde. Alles aus anderen Quellen und von anderen Personen übernommene Material, das in der Arbeit verwendet wurde oder auf das direkt Bezug genommen wird, wurde als solches kenntlich gemacht. Insbesondere wurden alle Personen genannt, die direkt an der Entstehung der vorliegenden Arbeit beteiligt waren. Die aktuellen gesetzlichen Vorgaben in Bezug auf die Zulassung der klinischen Studien, die Bestimmungen des Tierschutzgesetzes, die Bestimmungen des Gentechnikgesetzes und die allgemeinen Datenschutzbestimmungen wurden eingehalten. Ich versichere, dass ich die Regelungen der Satzung der Universität Leipzig zur Sicherung guter wissenschaftlicher Praxis kenne und eingehalten habe.

.....
Datum

.....
Unterschrift

Publikationen

Haehnel S, Rade M, Kaiser N, Reiche K, Horn A, Loeffler D, Blumert C, Rapp F, Horn F, Meixensberger J, Renner C, Mueller W, Gaunitz F, Bechmann I, Winter K (2021): *Benefit and limitations of glioblastoma tissue slice cultures – an RNA sequencing study*. FEBS Open Bio.

Haehnel S, Reiche K, Loeffler D, Horn A, Blumert C, Puppel S-H, Kaiser N, Rapp F, Rade M, Horn F, Meixensberger J, Bechmann I, Gaunitz F & Winter K (2019): *Deep sequencing and automated histochemistry of human tissue slice cultures improve their usability as preclinical model for cancer research*. Sci Rep 9, doi:10.1038/s41598-019-56509-5.

Menzel F, Kaiser N, **Haehnel S**, Rapp F, Patties I, Schöneberg N, Haimon Z, Immig K & Bechmann I (2018): *Impact of X-irradiation on microglia*. Glia 66, doi:10.1002/glia.23239

Sönnichsen R, Hennig L, Blaschke V, Winter K, Körfer J, **Hähnel S**, Monecke A, Wittekind C, Jansen-Winkel B, Thieme R, Gockel I, Grosser K, Weimann A, Kubick C, Wiechmann V, Aigner A, Bechmann I, Lordick F & Kallendrusch S (2018): *Individual Susceptibility Analysis Using Patient-derived Slice Cultures of Colorectal Carcinoma*. Clin Colorectal Cancer 17, doi:10.1016/j.clcc.2017.11.002.

Vorträge

05/2017 – Jahrestagung der Deutschen Gesellschaft für Neurochirurgie, Magdeburg.
Titel: “*Glioblastoma tissue slices – What can we learn from them?*”

11/2016 – Statusseminar des Bundesministeriums für Bildung und Forschung (BMBF) der im Rahmen der 3R-Initiative geförderten Projekte, Berlin. Titel: “*Humane organotypische Schnittkulturen aus Glioblastomgewebe als Testsystem zur Aufklärung molekularer Mechanismen der Therapieresistenz und Tumorausbreitung*“